A 135° Gas-Filled Magnet at the Cologne 10 MV AMS FN-Tandem Accelerator Setup and the use of ^{41}Ca as a Reference Nuclide for Nuclear Waste Management

Inaugural-Dissertation

zur
Erlangung des Doktorgrades
der Mathematisch-Naturwissenschaftlichen Fakultät
der Universität zu Köln

vorgelegt von

Richard Spanier
aus Frechen

Köln 2019

The saddest aspect of life right now is that science gathers knowledge faster than society gathers wisdom.

– Isaac Asimov –

Kurzzusammenfassung

Diese Arbeit legt den Schwerpunkt auf die Verbesserung der Messmöglichkeiten am Kölner 10 MV FN-Tandem-Beschleuniger und dem Kölner 6 MV Tandetron™-Beschleuniger, im Hinblick auf Beschleuniger-Massenspektrometrie (AMS). Die Arbeit teilt sich in vier Bereiche auf. Dies beinhaltet zum einen die Entwicklungen und Verbesserungen der experimentellen Aufbauten, die Datenaufnahme und Datenverarbeitung und zum anderen die durchgeführten Messungen mit ^{58}Fe/^{58}Ni am 10 MV Tandem-Beschleuniger sowie die Untersuchungen am 6 MV Tandetron™-Beschleuniger hinsichtlich ^{41}Ca als mögliches neues Referenznuklid für den Umgang mit radioaktivem Abfall, welcher bei dem Abbau von Reaktoranlagen anfällt.

Beide Beschleunigersysteme sind ausgestattet mit einem vergleichbaren MPA3-Datenaufnahmesystem. Aufgrund der vielen einzelnen Dateien mit Messergebnissen, speziell bei AMS-Batch-Messungen am 6 MV Tandetron™-Beschleuniger, wurden verschiedene Python-Programme entwickelt um die Daten zu extrahieren und zu sortieren. Besondere Aufmerksamkeit wurde hierbei auf die Offline-Datenanalyse von Listmode-Dateien, im Hinblick auf die Möglichkeiten durch verschiedene Signalkombinationen, das Ändern oder neu Setzen von ROIs und weiteren Softwarebedingungen, gelegt.

Für zukünftige ^{60}Fe-Messungen ist das dedizierte AMS-Strahlrohr des 10 MV Tandem-Beschleuniger in Verbindung mit dem neuen 135° gasgefüllten Magneten gut geeignet, da das Isobar ^{60}Ni durch die Verwendung des neuen Magneten um mehrere Größenordnungen unterdrückt werden kann. Im Rahmen dieser Arbeit wurden die nötigen Untersuchungen zu Strahleinstellungen und dem gasgefüllten Magneten mit stabilem ^{58}Fe durchgeführt. Messungen am niederenergetischen Massenspektrometer haben gezeigt, dass FeO^-, im Vergleich zu elementarem Fe^- und FeO_2^-, den höchsten Strahlstrom liefert. Mit der Inbetriebnahme des neuen 135° Magneten, wurde außerdem ein Gassystem aufgebaut, welches in der Lage ist, sowohl das N_2-Gas als auch das Isobutan-Gas für die angeschlossene Gasionisationskammer zu handhaben. Die Homogenität des magnetischen Feldes, in einem Bereich von ± 50 mm um die optische Achse, innerhalb der Vakuumkammer, wurde mit Hilfe einer NMR-Sonde zu $B_{hom} < 1.64 \times 10^{-4}$ gemessen und ist damit besser als die von Hersteller angegebene Homogenität von $B_{hom} = 4 \times 10^{-4}$. Die Messungen der populierten Ladungszustände von ^{58}Fe und ^{58}Ni nach dem Durchgang durch die Eintrittsfolie des Magneten wurden durchgeführt. Hieraus ergibt sich eine Transmission von 53% ohne N_2-Gas. Die Untersuchung eines 100 MeV ^{58}Fe Strahles, nach dem Durchgang durch 7 mbar N_2-Gas, ergab eine Breite von $\sigma = 12.0$ mm in der dispersiven Ebene. Die ^{58}Ni-Komponente war in diesem Fall 81 mm räumlich separiert. Eine existierende 10-Anoden-Gasionisationskammer, mit einer aktiven Länge von 509 mm, wurde überholt und wieder in Betrieb genommen. Erste Tests mit ^{12}C ergaben eine totale Energieauflösung von $E_{res} = 1.72\%$. Der Energieverlust in Materie wurde mittels ^{40}Ca, ^{39}K und ^{48}Ti sowie ^{58}Fe und ^{58}Ni untersucht. Der erzielte Separationsfaktor für ^{58}Fe und ^{58}Ni bei 88 MeV ist $S_f = 3.9$. Parallel hierzu wurde ein neuer 5-Anoden-Gasionisationsdetektor, mit einer aktiven Länge von 150 mm, entwickelt und gebaut. Getestet wurde der neue Detektor am 6 MV Tandetron™-Beschleuniger im Rahmen einer ^{10}Be-AMS-Messung. Die gemessenen Isotopenverhältnisse und der daraus bestimmte mittlere Korrekturfaktor von $c_f = 2.43$ stimmt innerhalb des 2σ Fehlers mit den Messungen des standardmäßig verwendeten 4-Anoden-Gasionisationsdetektors von High Voltage Engineering Europa B.V. überein.

Weitere Messungen haben gezeigt, dass bei vergleichbaren Strahlenergien von 54 MeV für ^{58}Fe, die Trennung zwischen ^{58}Fe und ^{58}Ni durch die Ionisationskammer, hinter dem gasgefüllten Magneten um 36% besser ist, als ohne diesen. Der höchste Separationsfaktor von $S_f = 4.76$ für ^{58}Fe, gemessen mit dem neuen 5-Anoden-Gasionisationsdetektor nach dem gasgefüllten Magneten, wurde bei 7 mbar N_2-Gasdruck und 28 mbar Isobutan-Gasdruck erzielt.

Neben diesen Untersuchungen wurden außerdem stabile und reproduzierbare Einstellungen zur Messung von ^{41}Ca am 6 MV Tandetron™-Beschleuniger erarbeitet. Die Messung des niedrigsten Standardmaterials mit einem nominalen Verhältnis von $R_{lit}(^{41}Ca/Ca) = 5.885 \times 10^{-13}$ ergab ein Isotopenverhältnis von $R(^{41}Ca/Ca) = 4.70(79) \times 10^{-13}$ was einem Korrekturfaktor von $c_f = 1.25$ entspricht. Des Weiteren wurde ^{41}Ca in Schwerbetonproben untersucht, welche zuvor am Forschungsreaktor TRIGA Mark II in Mainz mit Neutronen bestrahlt wurden. Durch verschieden lange Bestrahlungszeiten, konnten Proben mit Isotopenverhältnissen zwischen 10^{-9} und 10^{-11} erzeugt und später gemessen werden. Die erwarteten Aktivitäten und Isotopenverhältnisse wurden unter Berücksichtigung des gesamten ausgesendeten Neutronenenergiespektrums und der zugehörigen energieabhängigen Neutroneneinfangwirkungsquerschnitte berechnet. Der hieraus ermittelte mittlere Neutroneneinfangwirkungsquerschnitt ist $\overline{\sigma} = 0.28$ barn. Der Vergleich zwischen den berechneten und den gemessenen Werten zeigt die hohe Präzision der Messungen und bestätigt die Möglichkeit bestrahlte Schwerbetonproben mittels AMS zu untersuchen um Aussagen über die Aktivität und den Gesamtneutronenfluss zu treffen. Erste Proben von einem biologischen Schild eines Reaktors ergaben ein Isotopenverhältnis zwischen 3.92×10^{-9} und 1.21×10^{-8}.

Abstract

This thesis is focused on the improvement of the measurement capabilities at the Cologne 10 MV FN-Tandem accelerator as well as the Cologne 6 MV Tandetron™ accelerator, with respect to accelerator mass spectrometry (AMS). It is separated into four different main topics. The developments and improvements concerning the experimental setups, the data acquisition and data processing on the one hand and on the other hand the measurements of ^{58}Fe/^{58}Ni at the 10 MV Tandem accelerator as well as the investigations concerning ^{41}Ca as a new reference nuclide for the topic of nuclear waste management, performed at the 6 MV Tandetron™ accelerator.

Both accelerator systems are equipped with a comparable MPA3 data acquisition system. According to the large number of files generated during the AMS measurements, especially during the batch mode measurements at the 6 MV Tandetron™ accelerator, different Python tools were developed to extract and sort the data from these files. Special attention was payed to the generated list mode files, which enables an offline data analysis with respect to signal combinations, the used ROIs and further software conditions.

For upcoming measurements of ^{60}Fe, the dedicated AMS beamline at the 10 MV Tandem accelerator in combination with a new 135° gas-filled magnet is well suited, since the isobar ^{60}Ni should be suppressed by several orders of magnitude by the use of the new magnet. Within the scope of this thesis, the required tests with stable ^{58}Fe, the tuning procedure and the measurements with the gas-filled magnet were conducted. Investigations at the low energy mass spectrometer revealed that FeO$^-$, in comparison to elemental Fe$^-$ or FeO$_2^-$, provide the largest beam output. The new 135° gas-filled magnet was set into operation at the 10 MV Tandem accelerator, including a gas handling system for the N$_2$ gas used at the magnet as well as the isobutane gas for the ionization chamber downstream the magnet. The magnetic field homogeneity was determined by a NMR probe to B$_{hom}$ < 1.64×10^{-4} in a range of ±50 mm around the optical axis, which is better than the manufacturers specifications of B$_{hom}$ = 4×10^{-4}. Measurements were performed with ^{58}Fe and ^{58}Ni according to the charge state population after the entrance foil of the magnet, resulting in a transmission of 53% through the magnet without N$_2$ gas. The beam width of a 100 MeV ^{58}Fe ion beam passing the gas-filled magnet, with a pressure of 7 mbar N$_2$ gas is σ = 12.0 mm in the dispersive plane. The separation from the ^{58}Ni component, under these conditions, was measured to 81 mm.

The existing 10 anode ionization chamber was overhauled and set back into operation. The detector has a total active length of 509 mm. First tests with ^{12}C revealed a total energy resolution of E$_{res}$ = 1.72%. The energy loss in matter was investigated by additional measurements with ^{40}Ca, ^{39}K and ^{48}Ti as well as ^{58}Fe and ^{58}Ni beams. The achieved separation factor for ^{58}Fe and ^{58}Ni at 88 MeV is S$_f$ = 3.9. In parallel, a new 5 anode ionization chamber was developed with an active length of 150 mm. The new ionization chamber was tested during a ^{10}Be AMS measurement at the 6 MV Tandetron™ accelerator. The resulting isotopic ratios and the achieved mean correction factor of c$_f$ = 2.43 matches the values determined by the reference 4 anode ionization chamber from High Voltage Engineering Europa B.V., used as standard for ^{10}Be measurements at the Cologne 6 MV Tandetron™ accelerator, within the 2σ error limits.

Measurements with these detectors revealed, that at comparable beam energies of 54 MeV for a ^{58}Fe beam, the separation between ^{58}Fe and ^{58}Ni inside an ionization chamber is 36% larger

after the gas-filled magnet than without. The best separation factor of $S_f = 4.76$ for ^{58}Fe was measured with the 5 anode ionization chamber after the gas-filled magnet, with 7 mbar N_2 gas pressure and 28 mbar isobutane gas pressure.

Furthermore, stable and reproducible system settings were determined to measure the radionuclide ^{41}Ca at the 6 MV Tandetron™ accelerator. The lowest available standard with a nominal ratio of $R_{lit}(^{41}Ca/Ca) = 5.885 \times 10^{-13}$ could be measured to $R(^{41}Ca/Ca) = 4.70(79) \times 10^{-13}$ which corresponds to a correction factor of $c_f = 1.25$. The blank level is 6×10^{-14}. Furthermore, ^{41}Ca in concrete material was investigated by irradiating heavy concrete samples with neutrons at the research reactor TRIGA Mark II at Mainz. By choosing different irradiation times, samples with isotopic ratios between 10^{-9} and 10^{-11} could be produced and measured. The expected radioactive activities and isotopic ratios were calculated by taking the full neutron energy spectrum emitted from the research reactor and the corresponding energy depending neutron capture cross sections into account, which results in a mean neutron capture cross section of $\overline{\sigma} = 0.28$ barn. The comparison of calculated and measured isotopic ratios showed the high precision of the performed AMS measurements and confirms the possibility of investigating concrete samples with AMS methods and obtain informations concerning their radioactive activity and the applied neutron flux. Samples from a biological shield of a research reactor were measured and provided isotopic ratios between 3.92×10^{-9} and 1.21×10^{-8}.

Contents

Chapter 1

Introduction

Accelerator Mass Spectrometry (AMS) is a highly sensitive method for counting atoms and to determine even lowest concentrations. For this purpose, the material of interest is extracted as an ion beam, mainly by the use of a cesium sputter source. For the acceleration of negative ions, as extracted by this type of source, tandem accelerators are used for two main reasons. On the one hand the applied voltage is used twice to achieve higher energies and on the other hand molecules are destroyed, which reduces the background. In a first state the ions are accelerated towards a thin carbon foil or a low pressure gas, at the center of the accelerator, where molecules are dissociated and electrons are stripped of the ions. Therefore, the second stage of acceleration uses the same electrical potential to repel the ions. The separation of the beam components is achieved by electric and magnetic fields or a combination of both, according to the E/q and p/q value, respectively. In a last step isobars are separated by the differential energy loss in matter, according to their nuclear charge. In this way, it is possible to measure isotopic ratios down to 10^{-16}. Applications for AMS measurements can be found in many fields of research. For example archeology, environmental sciences, geology, (bio-)medicine, nuclear astrophysics, oceanography, paleontology or paleoclimatology, see Fifield [1] and Chen et al. [2].

The University of Cologne provides a 10 MV FN-Tandem accelerator and a 6 MV Tandetron™ accelerator. The latter was installed in 2011 and is mainly used for AMS measurements. In this context, the new center for Accelerator Mass Spectrometry in Cologne, CologneAMS, was found. Also the 10 MV Tandem accelerator is equipped with a dedicated beamline for AMS measurements, see Schiffer [3].

In the coarse of this thesis, the AMS measurement capabilities at both accelerators were extended. In chapter 2 several basic concepts concerning the interaction of ions and matter in terms of the intended measurements are given and discussed. Furthermore, important terms are defined. The used experimental setups, the developments and test measurements are described in chapter 3. This includes the sample preparation, the commissioning of a new 135° gas-filled magnet, the recommissioning of a 10 anode ionization chamber and the test of a new designed 5 anode ionization chamber. The used MPA3 data acquisition system is described in chapter 4, with respect to the online and offline data analysis. To this end, several python tools are developed and the capabilities for offline analysis of the ROOT framework are investigated. For the intended measurement of the radionuclide ^{60}Fe, several measurements were performed with ^{58}Fe and the corresponding isobar ^{58}Ni, see chapter 5. This includes measurements with the new 135° gas-filled magnet, the determination of the separation factor achieved from the gas-filled magnet as well as the ionization chambers. In chapter 6 the measurements and investigations on the radionuclide ^{41}Ca at the 6 MV Tandetron™ accelerator are discussed. The tuning process of the system to achieve stable and reproducible settings is described. Furthermore, the production and measurement of concrete samples irradiated with neutrons is given and analyzed. In this way it was tested, if ^{41}Ca could be a new reference nuclide for nuclear waste management.

Chapter 2

Basic Concepts

Within the scope of this chapter, basic concepts will be discussed which are important for many parts of the thesis and AMS measurements in general. The chapter is divided into two parts. First of all the interaction of ions with matter is explained, with respect to the energy loss and energy loss straggling as well as the angular straggling and changes of the charge state, with special regard to the used calculation tools LISE++ and SRIM. Furthermore, basic definitions are given as they are used within this thesis. In a second part the concepts of isobar separation and suppression with respect to different techniques are discussed.

2.1 Interaction of Ions with Matter

Due to the relative low energies used for AMS measurements, especially for the medium mass isotopes investigated in this thesis, no nuclear reaction will take place. On this account, the interactions are limited to energy loss, energy loss straggling and angular straggling and the corresponding charge changing processes, which are described briefly in the following sections.

2.1.1 Energy Loss

For isobar separation and suppression during AMS measurements the differential energy loss $\mathrm{d}E/\mathrm{d}x$ of ions passing matter is commonly used. The energy loss is mainly caused by the projectile scattering on the Coulomb field of the target material electrons. As particles with the energy E moving a distance x through matter they lose an amount ΔE energy.

$$\Delta E = \int\limits_{0}^{x_1} \frac{\mathrm{d}E}{\mathrm{d}x}\, E\,\mathrm{d}x$$

This relation is used to estimate or simulate the required gas pressure for any kind of gas ionization chamber, the remaining energy after stripper and degrader foils or entrance/exit windows and the gas pressure for gas-filled magnets. In all of these cases, the correct knowledge of the required or remaining energies allow to tune the desired ion beam and identify isotopic components by their difference in energy. First investigations concerning the differential energy loss were published by Bethe [4] and Bloch [5], which lead to the Bethe-Bloch formula, which is given here in the non-relativistic form.

$$-\frac{\mathrm{d}E}{\mathrm{d}x} = \frac{4\pi Z_P^2}{m_e v^2}\left(\frac{e^2}{4\pi\epsilon_0}\right)^2 n\ln\left(\frac{2m_e v^2}{I}\right)$$

Where Z_P is the nuclear charge of the projectile, v the velocity of the projectile, m_e the electron mass, n the electron density and I the mean excitation potential of the target material. Further

measurements concerning corrections for not fully stripped ions and projectiles of a certain charge state q were performed by Lindhard and Sørensen [6]. These investigations lead to the first general description of energy loss and stopping for heavy ions and forms the basis of the software SRIM [7] and LISE++ [8]. Both programs allow to calculate the energy loss and range of various ions in different materials and are used in the scope of this thesis. SRIM allows to simulate even compound materials by a linear combination of individual energy losses by applying Bragg's rule [9]. The formalism used in LISE++ during this thesis is ATIMA 1.2, which is developed and supported by the GSI (Helmholtzzentrum für Schwerionenforschung). The energy loss calculations in LISE++ are based on the measurements of Ziegler et al. [7] for particle energies below 10 MeV and for energies above 30 MeV the theory and the measurements of Lindhard and Sørensen are used. For particles with an intermediate energy the result is interpolated between both theories, therefore, the results of SRIM and LISE++, especially for higher energies, are not fully comparable and, for our needs, more accurate by LISE++, see energy loss calculations in sec. 3.6.2. A comparison between the predicted energy losses calculated with LISE++ and measured energy losses for medium mass isotopes inside a 1 μm silicon nitride (SiN) foil was done by Feuerstein [10].

2.1.2 Energy Loss Straggling

In any case of an energy loss interaction, energy loss straggling occurs and is defined as the mean square deviation of the energy loss ΔE, see Lindhard et al. [6].

$$\Omega^2 = \left\langle \left(\Delta E - \langle \Delta E \rangle \right)^2 \right\rangle$$

The energy loss straggling is responsible for beam broadening. This aspect becomes vitally important for gas-filled magnets, due to the long flight path through an area of increased pressure, compared to the vacuum, and the related energy loss. To predict energy loss straggling three different methods are commonly used. One way is to use the program SRIM, which is, according the energy loss straggling, based on the formalism described by Bohr [11].

$$\Omega_{\text{Bohr}}^2 = 4\pi Z_1^2 Z_2^2 \, e^2 N$$

Where Z_1 and Z_2 represents the atomic numbers of the projectile and the target, and N the density of the target material. Bohr's description is based on the assumption of fully stripped, fast ions, which transfer only a very small part of there energy per collision.

The formalism implemented to ATIMA 1.2, is based on Hvelplund et al. [12, 13] for particle energies below 10 MeV, and Lindhard and Sørensen for energies above 30 MeV. Hvelplund described straggling for the low and medium energy region. He also added a more realistic description of the charge distribution ρ(r) based on the first-order Lenz-Jensen model, see Lenz [14] and Jensen [15], compared to the studies by Bohr.

$$\Omega_{\text{Hvelplund}}^2 = \frac{\Omega_{\text{Bohr}}^2}{Z_2} \int 4\pi r^2 \rho(r) \, \frac{\Omega^2(r, v)}{\Omega_{\text{Bohr}}^2} \, \mathrm{d}r \tag{2.1}$$

Where $\Omega^2(r, v)$ describes the contribution to the straggling by atomic electrons. The atomic electron distribution at a distance r is given by ρ(r) and v is the velocity of the particle, for further details see Bonderup et al. [12]. The latest description for energy loss straggling, discussed here, was presented by Yang et al. [16]. Yang introduced a way to adapt the concept of effective charges to straggling calculations by performing a large number of individual measurements and

introduced several fit parameters ($C_1 - C_4$), depending on the used particle and target materials (atomic gas, molecular gas or solid). The concept of effective charges was invented by Biersack et al. [17], which reduces the amount of "interacting charge". The result is given in eq. 2.2 and the corresponding fit parameters can be found in Yang et al. [16, p.153].

$$\Omega^2_{\text{Yang}} = \Omega^2_{\text{Bohr}} \frac{Z_1^{4/3}}{Z_2^{1/3}} C_1 \frac{\Gamma}{(\varepsilon - C_2)^2 + \Gamma^2} \tag{2.2}$$

$$\text{where: } \Gamma = C_3 \left(1 - e^{-C_4 \varepsilon} \right)$$

$$\varepsilon = \begin{cases} E/Z_1^{3/2} & \text{,for gas targets} \\ E/Z_1^3 Z_2^{1/2} & \text{,for solid targets} \end{cases}$$

A detailed experimental investigation concerning the Yang straggling was done by Feuerstein [10] for 1 μm SiN foils at beam energies of $25\,\text{MeV} < \text{E} < 60\,\text{MeV}$.

2.1.3 Angular Straggling

The angular straggling is responsible for ion beam broadening as it passes through matter. Early records to this topic observed angular deviations in cloud-chamber measurements, see Bohr [11] and Williams [18] described the distribution of scattered particles as nearly Gaussian.

Sigmund and Winterborn [19] decided upon a classical approach, re-evaluated from the quantum mechanic descriptions of Molière [20], which extends the existing description for thicker targets and higher particle energies. They considered the concept of the "reduced" target thickness τ and the "reduced" scattering angle $\tilde{\alpha}$ introduced by Meyer [21]. They not longer calculated each scattering step along the flight path up to the n-th step, and reduced the expression for the scattering angle to the following simple form.

$$\tilde{\alpha} = \frac{a\,E}{2\,Z_P Z_T\,e^2}\,\alpha \tag{2.3}$$

$$\tau = \pi a^2 N t$$

$$\text{where: } a = 0.465 \times 10^{-8}\,\text{cm} \cdot \sqrt{Z_P^{2/3} + Z_T^{2/3}}$$

Where α describes the angle between the projectile and the beam axis after the scattering, E the energy of the projectile, Z_P and Z_T the nuclear charge of the projectile and the target, N the density and t the thickness of the target. The mentioned approaches were investigated at the LISE spectrometer at GANIL National Facility in Caen by Anne et al. [22]. Measurements were taken for multiple angular scattering of heavy ions in solid and gas targets in the energy range of 20 - 90 MeV/u. The result is again expressed in terms of the reduced thickness τ and reduced scattering angle $\tilde{\alpha}$.

$$\tilde{\alpha} = 1.00\,\tau^{0.55} \tag{2.4}$$

$$\tau = \frac{41.5 \times 10^3\,t}{M_T \left(Z_P^{2/3} + Z_T^{2/3} \right)}$$

Where $\tilde{\alpha}$ is given in mrad, t is the target thickness in mg/cm² and M_T the target mass number.

Based on this empirical studies a formalism for LISE++ was developed and implemented.[1]

2.1.4 Charge States of Ions after passing Matter

Ions passing matter in general change their charge state by collisions. In case of solid matter or gas, with a sufficient high pressure, electrons are removed from the incoming ions. This process is called stripping and was first suggested by Flamm and Schumann [23] and further investigated by Henderson [24] and Bohr [25]. Bohr brought together many, most empirical, findings and described the electron loss and also the capture process as a relation between the electron orbital velocity u and the projectile velocity v, see Bohr [26]. The probability for half the electrons to be stripped at u = v is 50% and called the Bohr criterion. To improve the prediction and calculate a so called equilibrium charge state q_m, of ions passing through matter (solid foils or gas) the theoretical concepts from Bohr and Lamb [27] were combined with empirical studies of Betz [28, 29]. Betz introduced an asymmetric term to describe the charge state of elements heavier than hydrogen and helium. The asymmetric tail for $q > q_m$ results on the charge changing cross section for multiple electron loss, which is much larger in heavy target material than in light ones. He described the charge state distribution F(q) as an asymmetric function, given in eq. 2.5. Where ρ represents the width of a Gaussian distribution and ε is the asymmetric parameter.

$$F(q) = \exp\left(\frac{-0.5\,((q - q_m)/\rho)^2}{1 + \epsilon\,(q - q_m)/\rho} \right) \tag{2.5}$$

$$\text{with: } \rho = 0.48 \cdot Z^{0.45} \left(\frac{q_0}{Z} \left(1 - \frac{q_0}{Z} \right) \right)^{0.26}$$

$$\epsilon = \rho \cdot (0.0007 \cdot Z - 0.7 \cdot \beta)$$

Therefore, it is possible to calculate the available charge states and their abundances with respect to the nuclear charge Z, the mass A and the energy E of the desired particle. Based on this results he defined a relation for the average charge q_m, depending on the nuclear charge Z and the target material.

$$q_m = Z \left[1 - C \cdot (0.71\,Z^a)^{\frac{\beta}{\alpha}} \right]$$

The parameters C and a specifies the target material, β is the relative velocity v/c and α the fine structure constant. Sayer further improved this semi-empirical studies of Betz, to calculate populated charge states in gas, see eq. 2.6 and carbon foils, see eq. 2.7, for further explanations see Sayer [30]. These semi-empirical formulas tend to hold for a wide range of isotopes and charge states, it is restricted to $0.07 \leq q_0/Z$ for gases and $0.15 \leq q_0/Z \leq 0.95$ for carbon foils.

$$q_m = 1 - 1.08 \cdot \exp\left(-80.1 \cdot Z^{-0.506} \cdot \beta^{0.996} \right) \quad \text{,for gases} \tag{2.6}$$

$$q_m = 1 - 1.03 \cdot \exp\left(-47.3 \cdot Z^{-0.38} \cdot \beta^{0.86} \right) \quad \text{,for carbon foils} \tag{2.7}$$

$$\text{with: } \quad \beta \ = \sqrt{\frac{2 \cdot E}{m}}$$

---

[1] NSCL Lise, Retrieved February 25,2019 from http://lise.nscl.msu.edu

These equations are used to determine the mean charge state expected for the beam transport after the accelerator, gas-filled magnets or after degrader foils. In the scope of this thesis several measurements were performed to investigate also the applicability of the given formulas. The concept of calculating mean charge states q_m is also very important for the use of gas-filled magnets, see sec. 5.3. More detailed investigations concerning the electron loss and electron capture is of importance for any detailed numerical description and computer based simulations. The required cross sections for electron capture were determined by Schlachter et al. [31]. He defines a reduced energy $\tilde{E}$ to describe the electron capture cross section σ_c.

$$\tilde{E} = \frac{E}{M} \frac{1}{\left(Z_2^{1.25} \, q^{0.7} \right)}$$

$$\sigma_c = \frac{1.1 \times 10^{-8} \cdot q^{0.5}}{\tilde{E}^{4.8} \cdot Z_2^{1.8}} \cdot \left[1 - e^{\left(-0.037 \, \tilde{E}^{2.2} \right)} \right] \cdot \left[1 - e^{\left(-2.44 \times 10^{-5} \, \tilde{E}^{2.6} \right)} \right]$$

The required cross sections for electron loss σ_l were determined by Sarén et al. [32]. He assumes an exponential model.

$$\sigma_l = A \, e^{b \, (q - q_m)}$$

Where the parameters A and b are fitted to experimental data, the procedure is described by Sarén [33]. Furthermore, multiple electron transfer processes were considered by Zoppi [34], who measured the dedicated cross section for multiple electrons for a few projectile target (N_2 gas, Ar) combinations. A detailed investigation and simulation is given by Feuerstein [10].

2.2 Isobar Separation and Suppression

During an AMS measurement the goal is to measure the amount of a desired radionuclide within a sample of a given size. For elements like carbon the answer to this question mostly depends on the extraction efficiency of the used ion source, see sec. 3.4, the overall transmission through the system and the detection efficiency. For other isotopes, for example the investigated ^{10}Be, ^{41}Ca or ^{58}Fe, the separation and suppression of unintended isobaric background becomes also important. Therefore, the second part of this section is about the separation and suppression, which is challenging for AMS measurements in general. First of all, important parameters like the isotopic ratio R and the separation factor S_f as well as the suppression factor S are defined and explained. In a second step frequent methods are described to achieve separation and suppression of unwanted isobaric background.

2.2.1 Isotopic Ratio

The isotopic ratio of a given sample is defined as the amount of radionuclide atoms divided by the amount of the related stable nuclide atoms or related radionuclide. To determine this parameter of an unknown sample is the goal for all AMS measurements. By using a particle detector, the number of radionuclide atoms N(R) can be measured. Since the number of stable atoms N(S) is by orders of magnitude higher than N(R), a current can be measured in a so called Faraday cup and is used to calculate N(S). The fraction of the radionuclide atoms divided by the number of

stable atoms of the corresponding isotope is defined as the isotopic ratio R.

$$R = \frac{N(R)}{N(S)}$$

Since the number of detected radionuclide atoms is very limited and only in the order of several hundred to a few thousand events, the relative counting error can be calculated with the Poisson statistics.

$$\Delta N(R) = \frac{1}{\sqrt{N(R)}} \approx \Delta R \, [\%]$$

As an example, it is necessary to have 10000 counts in total to achieve an error level of 1%. In terms of a measurement, at a beam current of $1\,\text{p}\mu\text{A}$, it would take about $44\,\text{h}$ to achieve a ratio of 10^{-14} at 1% statistical counting error. The measured isotopic ratio can therefore be described by the following formula.

$$R = \frac{N(R) \cdot q \cdot e}{I(S) \cdot t \cdot c_f}$$

Where N(R) is the number of the detected radionuclide atoms, I(S) the beam current of the stable isotopes, t the measurement time, q the charge state and e the elementary charge. The factor c_f describes the correction based on the transmission between the offset Faraday cup, were the stable beam is measured, and the used detector. The correction factor is determined by measuring samples with a well known ratio, so called standard samples. A more detailed description is given by Poutivtsev [35] and Schiffer [3].

## 2.2.2 Separation Factor S_f and Isobar Suppression S

The following section is about the separation of two 1-dim beam components related mainly to measurements performed with gas ionization chambers, gas-filled magnets or the projection of 2-dim histograms to a straight line. A simple definition of the separation between two measured beam components is given by Knie [36], see eq. 2.8. He described the separation factor as the distance d between both components divided by the full width at half maximum ($\text{FWHM} = 2\sqrt{2 \ln 2}\,\sigma$) of the component with the larger FWHM value.

$$S_f = \frac{d}{\text{FWHM}} = \frac{\mu_1 - \mu_2}{\text{FWHM}} \tag{2.8}$$

Higher values for S_f imply a higher possible separation. A similar definition of the separation factor was suggested by Feuertein [10]. He took the mean width of both distributions into account, instead the FWHM of the border distribution. Following this idea, but to achieve separation factors comparable to the factors determined with the definition of Knie, the mean FWHM was used, see eq. 2.9. This, results in the same values for the separation of equal width distributions, than the definition of Knie, but for measurements were one of the contamination is getting larger, the separation value gets smaller. It tends to be a more precise description of the measurement, and will therefore be used within this work.

$$S_f = \frac{\mu_1 - \mu_2}{0.5 \cdot 2 \cdot \sqrt{2 \ln 2}\,(\sigma_1 + \sigma_2)} \tag{2.9}$$

In most cases the separation factor can be calculated fast and gives a good impression of the
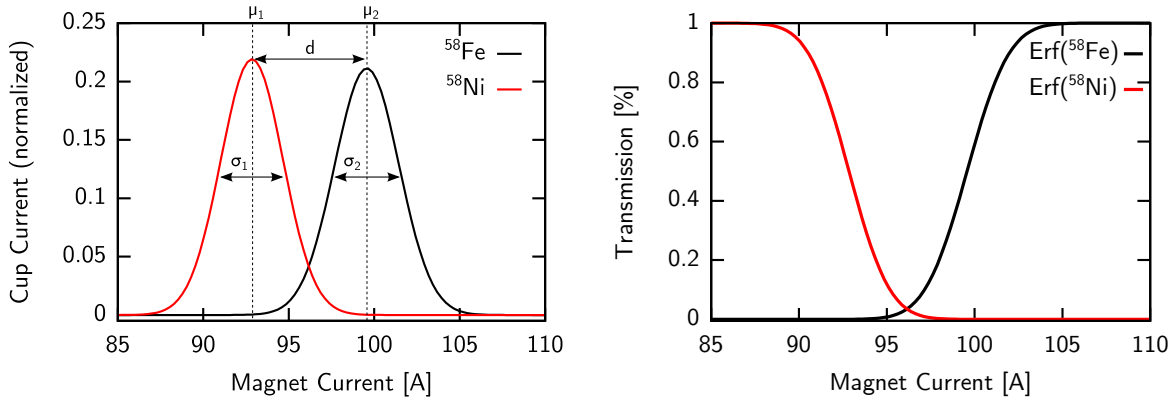
(a) Normalized beam currents measured for ^{58}Fe and ^{58}Ni after the gas-filled magnet. The position μ_1 and μ_2 represent the mean of a Gaussian distribution, the distance $d = |\mu_1 - \mu_2|$.

(b) Corresponding error function for both measured distributions. The error function for ^{58}Ni is plottet inverted for a better understanding.

Figure 1: The figure illustrates how the suppression of an unwanted isobar is associated with the transmission of both, the radionuclide and the corresponding isobar. Figure a) shows the measured beam currents for different magnetic fields, after the gas-filled magnet, and figure b) the integrated Gaussian distribution. The error function for ^{58}Ni was plotted inverse for a better understanding.

usability of the chosen separation or suppression techniques, the detector gas pressure as well as the quality of the system settings, see fig. 1a. But, it is devoid of any information about the measured or achievable ratio.

The suppression factor S is described by Martschini et al. [37] and further investigated by Schiffer [3]. This factor is based on the ratio of the transmission of the radionuclide and the transmission of the corresponding isobar to the detector, see eq. 2.10.

$$S = \frac{T_R}{T_I} \tag{2.10}$$

Hereinafter the suppression will be explained on the example of an ^{58}Fe and ^{58}Ni measurement performed after the gas-filled magnet, described later in this work, see chapter 5. The transmission is defined by Schiffer [3], as the part of a Gaussian distributed beam component that remains after setting certain cutoff conditions. In an 1-dim spectrum this is a limitation on the x-axis to a certain range of channels recorded by the analog digital converter (ADC), which corresponds to a limitation to a certain energy deposition range. For the case that this limitation is set on both sides of the distribution, the transmission is given by the following equation.

$$T_i = \int_l^r \frac{1}{\sqrt{2\pi}\,\sigma} \exp\left(-\frac{1}{2}\left(\frac{|I| - \bar{I}}{\sigma}\right)^2\right) \mathrm{d}|I|$$

$$= \frac{1}{2}\left(1 + \mathrm{erf}\left(\frac{|I| - \bar{I}}{\sigma\sqrt{2}}\right)\right)\Bigg|_l^r$$

Where I is the current applied to a magnet, $\bar{I}$ the current at the maximum beam intensity and σ the corresponding width of the distribution. The primitive of the Gaussian distribution is
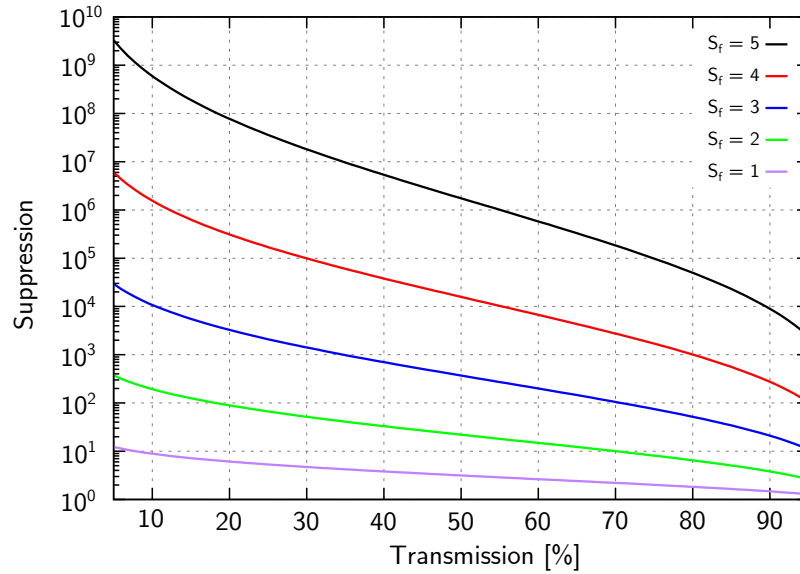
Figure 2: Indicated is the suppression of the isobar, achievable at a certain transmission of the radionuclide for different suppression factor S_f. Inspired by Feuerstein [10].

the so called error function, see fig. 1 for an example. In fig. 1a the measured and normalized beam currents of ^{58}Fe and ^{58}Ni for different magnetic field values are shown and in fig. 1b the corresponding error functions are given. The error function for ^{58}Ni was inverted for a better understanding. Depending on the cutoffs, the transmission of both, the isotope ^{58}Fe as well as the isobar ^{58}Ni, can be affected. Based on a given separation factor S_f only certain suppression values are achievable. Two beams that are more separated from each other, lead to a higher suppression and smaller losses in transmission with the same cutoff. In fig. 2, theoretical possible suppressions depending on the desired transmission for different separation factors are simulated, following Feuerstein [10]. Nevertheless, it must be kept in mind, that effects based on statistical straggling as well as possible tails generated by energy loss or pile up of multiple events are ignored in this description. These effects have to be investigated separately and are of high importance especially for low isotopic ratios.

2.2.3 Ion Sputter Source

The ion source is already important concerning the suppression of isobaric background. On account of the working principal of a tandem accelerator, negative ions are required for injection to take full advantage of the applied acceleration voltage. The probability to create negative ions and sputter them is different for each element and each molecule. Therefore, the correct choice of the extracted isotope in comparison with the correlated isobar is of great importance. Extensive investigations to extracted beam currents and the related cathode materials are given by Middleton [38]. For some isotopes of interest this effect fully suppresses possible isobars, for example ^{14}C and the isobar ^{14}N or ^{26}Al and the isobar ^{26}Mg, where no stable negative ions are formed by the isobar. In general, the ratio of negative to neutral particles N^-/N^0 sputtered by the Cs bombardment is described by the Langmuir-Saha-Equation [39].

$$\frac{N^-}{N^0} \propto \frac{g^-}{g^0} \exp\left(\frac{EA - \Phi}{kT}\right)$$

Where g^- and g^0 describe the statistical weights of negative or neutral particles, respectively, and Φ describes the work function at a temperature T. Of great importance is the electron affinity EA, which describes the energy released from a neutral atom by adding a free electron. For several elements the electron affinity is smaller than zero, and therefore no negative ions are built. This also applies for molecules. The isobar ^{26}Mg is fully suppressed, whereas ^{26}MgO easily forms negative molecules. A more detailed derivation of the classical form is given by Wendt et al. [40].

2.2.4 Full Stripping

Another possibility to suppress an isobaric component, at least if the nuclear charge of the isotope is larger than those of the isobar, is full stripping. In this case, all electrons have to be stripped of from the isotope as well as the isobar. The resulting beam can easily be separated by a subsequent bending magnet. The procedure, however, can only be used at high energy accelerators. A detailed investigation concerning the required energies was performed by Kutschera et al. [41]. He found out that, to achieve 7.2% fully strip ^{58}Ni inside a $0.5\,\text{mg/cm}^2$ carbon foil, a beam energy of at least 597 MeV is required. Which is much higher than achievable at the 6 MV Tandetron™ accelerator or the 10 MV Tandem accelerator. Also, by using a second stripper foil after the accelerator, the abundance for fully stripped ions is to low for AMS measurements.

2.2.5 Gas Ionization Chamber

A common approach for isobar separation and suppression is based on the differences in energy loss of particles passing matter, depending on their nuclear charge and energy, see sec. 2.1.1. The gas ionization chamber is the most widely used detector type for AMS measurements. It contains of a sealed volume, which is filled with a detector gas, usually isobutane gas and a beam entrance window, usually made of Mylar ($C_{10}H_8O_4$) or silicon nitride (Si_3N_4), to separate gas region from the ultra high vacuum (UHV).

During the interaction between the gas atoms and the incoming ions electrons are released. These electrons are collected by an electrical field applied between an anode and a cathode, perpendicular to the flight path of the particles. The measured signal depends on the induced charge at the anode while the electron moves through the gas. This induced electric current by moving charged particles in the vicinity of an electrode was first described by Shockley [42] and Ramo [43]. Since the moving distance of the electrons is important, a second potential step, between the anode and the cathode was suggested by Frisch [44]. In this way the signal is generated by the electrons between the Frisch-Grid and the anode. Therefore, the signal is insensitive to the original distance, between the anode and the cathode, were the electron was released at. Furthermore, the anode is segmented into several parts (at least two) along the flight path of the incoming particles, to distinguish particles with lower and particles with higher energy loss.

The advantages over other particle detector types, like germanium or silicon detectors, PIN diode arrays or solar panels, is the high radiation resistance and the comparatively easy handling. This includes the variability in gas pressure and therefore energy loss per unit length as well as different anode configurations for different radionuclide / isobar combinations, see sec. 3.7.1. The downside of this type of detector is a limitation to several hundred beam particles per second interacting with the detector gas. For higher beam intensities negative effects like pile up and electronic noise, arises. As a consequence, the measured position and width of each detected signal broadens and the energy resolution deteriorates. The achievable energy resolution depends on the energy loss, energy loss straggling, angular straggling, recombination, quality of the detector gas,

entrance window, anode segmentation, geometry and used electronics. In general, it is apparent that higher energies lead to a better separation, based on the larger differences in energy loss between the radionuclide and the isobar. A more detailed description of the detector design is given in sec. 3.6 on the basis of the 10 anode ionization chamber and the new designed 5 anode ionization chamber, described in sec. 3.7.

2.2.6 Degrader Foil Method

Similar to the ionization chamber, also the degrader foil method is based on different energy losses, of particles passing matter, depending on the nuclear charge. In this case, the beam has to pass a so called degrader or absorption foil usually made of SiN. The common thickness of such a foil is about 50 nm to several µm. When a beam passes the foil, on the one hand it loses energy depending on the nuclear charge and the initial energy and on the other hand different charge states are populated, as described in sec. 2.1.4. These differences in energy and charge state in combination with a subsequent dispersive element like a bending magnet or an electrostatic analyzer generates a spatial separation between different isotopes. Further investigation were done by Schiffer [3] at the 10 MV Tandem accelerator.

This method is widely used to reduce large amounts of background and isobaric contamination. In the course of this thesis it was used during the ^{10}Be measurements to reduce the ^{10}B background at the 6 MV Tandetron™ accelerator, see sec. 3.7.4. The disadvantage of this method is the charge state distribution created within the degrader foil. Only one charge state can be chosen by the dispersive element and transported onwards through the system, which results in major transmission losses.

2.2.7 Gas-Filled Magnet

Hereinafter, the working principal of a gas-filled magnet is explained. The ion beam passes a thin entrance foil to a magnet vacuum chamber, which is sealed on the exit and can be filled with gas. Often, the used gases are nitrogen or helium, both non reactive gases. When the ions passing through the gas-filled region, multiple interactions with the gas molecules take place and result in a statistical change of the charge state of each ion, described by eq. 2.6. If the mean free path is short, and therefore the number of statistical collisions high, the magnetic rigidity can be described by the following equation, see Paul et al. [45].

$$\langle B\rho \rangle = \frac{m\,v}{q_{\mathsf{m}}}$$

Where m is the mass, q_{m} the mean charge state of the ion and v the velocity. In this way the disadvantage of the degrader foil method can be compensated and all charge states are transported to a single point on the focal plane, at the exit of the magnet. The main reason to use a gas-filled magnet for AMS measurements is the difference in energy loss along the flight path, between the intended isotope and the corresponding isobar. In the case of the later described ^{58}Fe and ^{58}Ni measurements, this difference is of the order of MeV, which leads to a different mean charge state and a spatial separation, see fig. 3. But this large energy loss is also one of the main disadvantages. If one considers a 100 MeV ^{58}Fe beam the energy loss inside the foil is about 1 MeV for a 200 nm SiN window. The energy loss, for the same beam at the same initial energy, inside the gas-filled magnet at 3 mbar N_2 gas pressure, is about 30 MeV. Another aspect, resulting from these multiple collisions inside the gas, is a higher energy straggling and angular
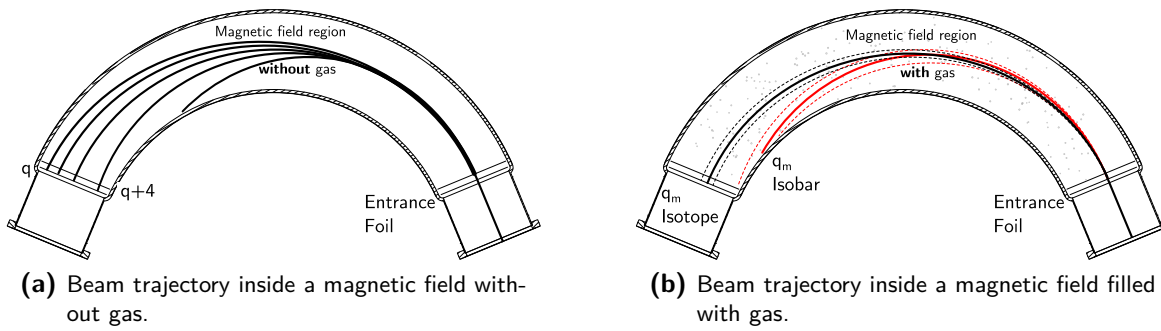
(a) Beam trajectory inside a magnetic field without gas.

(b) Beam trajectory inside a magnetic field filled with gas.

Figure 3: Figure a) shows the beam separation inside a magnetic field, based on its charge state generated in the entrance foil. Only a single charge state can be focused to the optical axis, which leads to high transmission losses. Figure b) shows the beam trajectory according to a mean charge state generated by multiple scattering inside the gas-filled region.

straggling, which leads to beam broadening. Furthermore, the additional entrance foil and the N_2 gas itself require a more complex setup and handling of the system, see sec. 3.5.3.

The concept of a gas-filled magnet was described for the first time by Fulmer and Cohen [46] in 1958 and later by Kubik et al. [47] in 1989. Important investigations concerning the optimal bending angle were done by Knie [36]. He described the spatial distance d between the isotope and the isobar on a circular trajectory as d $\propto 1 - \cos\phi$. His investigations revealed an optimal bending angle between $110°$ and $150°$. Based on this consideration and the good results achieved with a $135°$ gas-filled magnet at the mass spectrometer GAMS, see [36, 48], also the new magnet for the 10 MV Tandem accelerator was designed with a bending angle of $135°$. More details concerning the new magnet and the setup are given in sec. 3.5. First measurements were shown and discussed in sec. 5.4.

Chapter 3

Experimental Setup, Development and Test Measurements

The following chapter gives an insight to the experimental setup used during this work. This includes an overview of both accelerators available at the University of Cologne. In the course of this thesis both accelerators were used for different purposes, to benefit from their individual advantages. In the case of the 10 MV Tandem accelerator, measurements with ^{58}Fe and ^{58}Ni isotopes benefit from the larger available energies. Whereas the 6 MV Tandetron™ accelerator comes with a better beam transmission and a higher degree of automation. The achievable total transmission is largely based on the Ar-gas stripper, in contrast to the C-foil stripper used at the Tandem accelerator, which reduces the beam broadening and losses generated by the coulomb explosion, see Weisser [49, pp. 166]. The second large benefit is the high degree of automation at different parts of the system, starting with the possibility of tuning each element against the beam intensity at the Faraday cup as well as the software region of interest (ROI) set at the data acquisition system of the detector and ending with the fully automated batch mode for long term measurements of large sets of samples, in which the samples are inserted and measured one after another. This procedure was used for the ^{41}Ca samples, see chapter 6.

A second point described in this chapter, is the preparation of AMS samples for the MC-SNICS source. Based on this experience, also the extraction efficiency of the MC-SNICS source was investigated. The results for several elements as well as molecules are given below. Furthermore, the commissioning of the new $135°$ gas-filled magnet is described, as well as conducted tests concerning the magnetic field homogeneity. First measurements with this magnet are described later in the thesis in sec. 5.4.

The last part of this chapter deals with both ionization chambers used in the course of this thesis. On the one hand a 10 anode ionization chamber, obtained from the University of Utrecht, which had to be recommissioned and equipped with a new entrance window system. On the other hand a new designed 5 anode ionization chamber, which was designed to be compact, modular and easy to install at almost every place along the beamline. With both detectors several measurements were performed to determine performance indicators such as the optimal gas pressure for different beam energies, applied detector voltages, the total energy resolution as well as achievable separation factors. An AMS measurement with the radionuclide ^{10}Be was performed at the 6 MV Tandetron™ accelerator, to finally test the new designed ionization chamber. The results were compared to the well known detector setup of the 4 anode ionization chamber from High Voltage Engineering Europa B.V. (HVE), which is usually used for ^{10}Be measurements.

3.1 10 MV FN-Tandem Accelerator

The Cologne 10 MV Tandem accelerator is equipped with two pelletron chains and as insulation gas SF_6 with a pressure of 6.8 bar is used. The same insulation gas at the same pressure is used at the 6 MV Tandetron™ accelerator, therefore both accelerators can be operated with one gas system. For stabilization purposes two separate systems are available. On the one hand there is the generating volt meter (GVM) which detects the terminal voltage and converts it to a proportional current. Therefore, it is independent of the ion beam. On the other hand, the slit control is used for voltage stabilization. For this purpose a pair of x-slits is mounted after the 90° analyzing magnet I and II and read out. In this case the position of the ion beam is monitored along the dispersive axis and changes in the accelerator voltage can be observed and corrected, see Rohrer et al. [49, pp. 152]. For the required stripping process at the terminal, carbon foils are used. An overview of the whole system is given in fig. 4.

At the low energy side, the system is equipped with three different ion sources. A single cathode Middleton type cesium sputter source, a Duoplasmatron ion source, both mainly used for nuclear physics beam times and a MC-SNICS (Multi Cathode Source of Negative Ions by Cesium Sputtering), which is used for the AMS measurements. The MC-SNICS is designed by National Electrostatics Corp. (NEC) and can hold up to 40 samples inside a sample wheel. A first mass separation is achieved by a low energy mass spectrometer, which consists of a 90° electrostatic analyzer (ESA) and a 90° bending magnet, both with a radius of $\rho = 0.435$ m. Many parts of this AMS injector are obtained from the University of Utrecht, see van der Borg et al. [50]. For better beam focusing, a pre-acceleration unit, with up to 80 kV acceleration voltage is installed after the low energy mass spectrometer, which requires the whole injector system to be mounted on a high potential platform. Since the detection of the radionuclide and the corresponding stable isotope are required for AMS measurements, the vacuum chamber of the bending magnet is electrically isolated and connected to a so called bouncer unit. The bouncer unit contains of three power supplies in combination with an Arduino micro controller, to apply different voltages to the vacuum chamber within milliseconds. In this way the magnetic rigidity of the beam can be changed, and different masses can be selected without changing the slow responsive magnetic field.

The high energy mass spectrometer, down stream the accelerator, is based on a double focusing 90° analyzing magnet, with a bending radius of $\rho = 1.1$ m and a maximum magnetic flux density of 1.52 T, in combination with a 30° ESA with a bending radius of $\rho = 3.5$ m and a maximum electric field of 6.66 MV/m. To detect the stable beam components an offset Faraday cup chamber is installed after the 90° magnet, including two adjustable cups. For beam focusing and transport, a magnetic quadrupole triplet is installed right between the 90° magnet and the 30° ESA. Two other magnetic quadrupole doublets are installed in front and after the ESA, as well as a Time-of-Flight (TOF) system. The stop detector of the TOF system is followed by the new 135° gas-filled magnet, see sec. 3.5. In the end of the beam line another position for an ionization chamber is established.

The majority of the mentioned components, corresponding to the MC-SNICS ion source, the low energy mass spectrometer as well as the high energy mass spectrometer are connected to four different Programmable Logic Controllers (PLC) (Siemens SPS S7-200) and controlled over one computer by a dedicated LabVIEW™ software, see Feuerstein [10]. In this way it is possible to store and load settings for different isotopes, trace electrostatic and magnetic hardware components and monitor the whole system without interruption and with a high degree of automation. A more detailed description of the system, all components and exact positions is given by Schiffer [3].
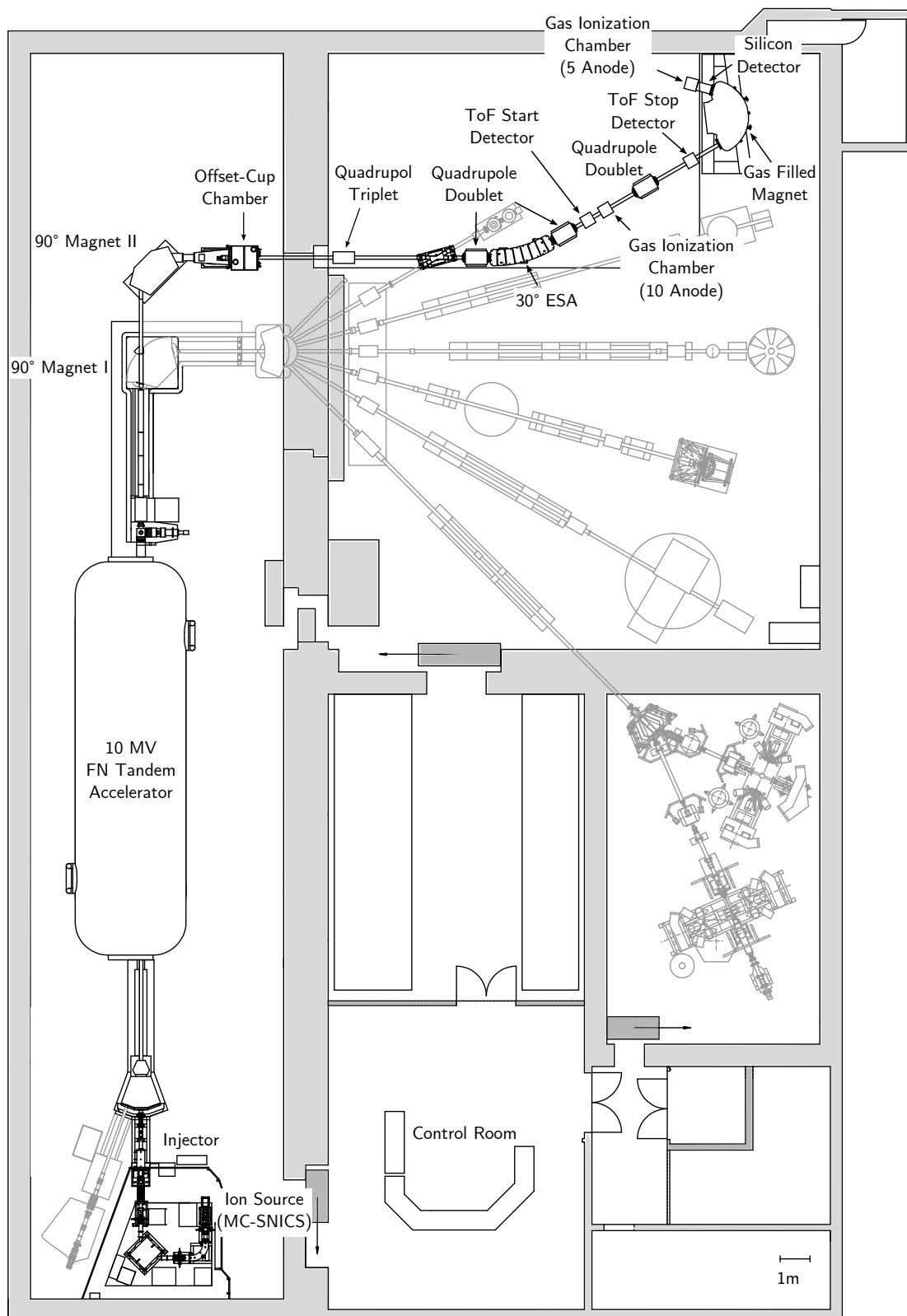
Figure 4: Overview of the 10 MV Tandem accelerator at the University of Cologne. Indicated are the important parts, used, installed or tested during this thesis. The indicated position of the 10 anode ionization chamber was used for test measurements only. Adapted from Schiffer [3].

3.2 6 MV Tandetron™ Accelerator

The 6 MV Tandetron™ accelerator, designed and built by HVE, was installed in 2011 at the second basement level below the earlier described 10 MV Tandem accelerator. The system is a dedicated AMS machine and only in a few cases used for other experimental tests or measurements. In this context the new center for Accelerator Mass Spectrometry in Cologne, CologneAMS, was found. An overview of the system is given in fig. 5 and a more detailed description is given by Dewald et al. [51].

The accelerator operates with a parallel fed Cockroft-Walton power supply, with all-solid-state diodes, conducted to two large dynodes on the high energy side of the accelerator tank. The oscillator frequency is 38 kHz, see Gottdang et al. [52] and Schenkel [53]. In this way the number of moving parts was reduced to a minimum, which is a great advantage compared to the 10 MV Tandem accelerator, with regard to abrasion and dust. It can be operated with both stripper types, carbon foils and argon gas.

The system is equipped with two SO-110 cesium sputter sources from HVE. The first one is used for solid samples and holds up to 200 cathodes. The other source is used to measure gaseous samples and can hold up to 50 cathodes. It is directly connected to a gas injection system from Ionplus AG which can handle up to 16 gaseous samples, see Stolz [54]. Both sources are connected to the same 54° ESA, with a bending radius of $\rho = 0.47$ m as linking part to the following beam system. The second part of the low energy mass spectrometer is a 90° analyzing magnet with a bending radius of $\rho = 0.4$ m. The vacuum chamber of the magnet can be put on high voltage, to achieve the same bouncer effect as described in the previous section, for the 90° low energy magnet. At the accelerator entrance a so called Q-snout lens, designed by Purser et al. [55] is used to create a field transition region between the field free region and the first columns of the accelerator, which helps to achieve higher transmission.

The high energy mass spectrometer consists of a 90° analyzing magnet, with a bending radius of $\rho = 2$ m, in combination with two 35° ESA's each with a bending radius of $\rho = 2.6$ m. The following switching magnet allows up to five beam lines for experimental setups for further separation or suppression steps. For beam focusing and manipulation several quadrupole triplets and steerer are installed. At the most right port under 30° another magnet with a bending angle of 120° and a radius of $\rho = 0.45$ m is installed. This magnet is, for example, used for ^{10}Be measurements in combination with the degrader foil method.

The available detector system consists of two ionization chambers designed from HVE with four anodes and an SiN entrance window. The ionization chambers are mounted at the left 30° beam line after the switching magnet and the other one after the 120° bending magnet. Furthermore, a TOF system was installed at the right 20° beam line, see Müller-Gatermann [56].

To detect the stable beam components for the AMS measurements, two offset Faraday cups are installed in the vacuum chamber after the 90° analyzing magnet. Both ionization chambers are connected to a FAST ComTec data acquisition system, which is further described in chapter 4.

The system is, with exception of the gas control system for the second ion source, controllable over a single computer system and can automatically handle AMS measurements after the beam was tuned to the detector. During a batch measurement, each sample is measured multiple times to compensate possible fluctuations of the system. Furthermore, the incoming data is analyzed online and a preliminary result is given for each run of any sample measured so far. More information and a detailed investigation of this procedure and the obtained data is given in sec. 4.3
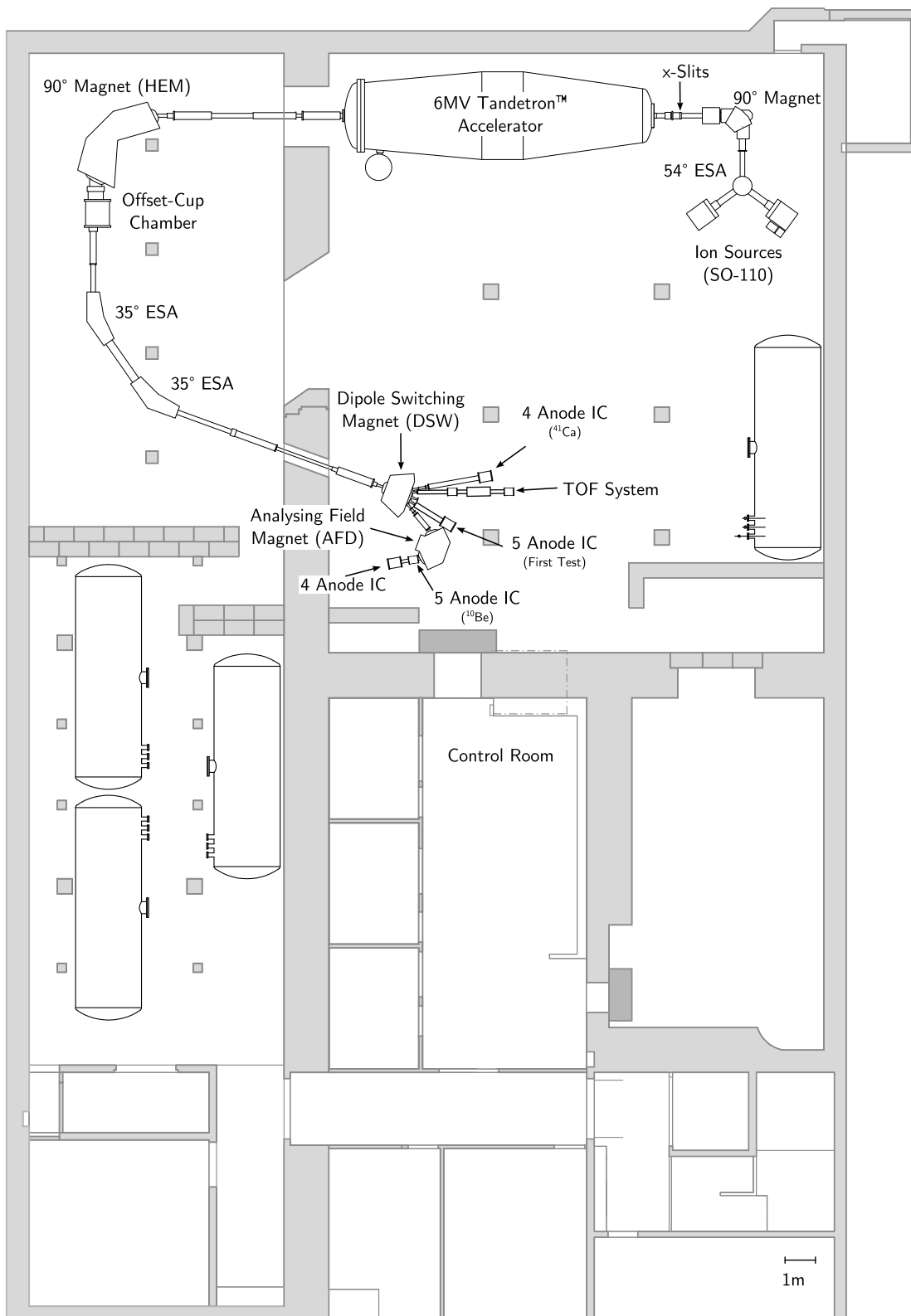
Figure 5: Overview of the 6 MV Tandetron™ accelerator at the University of Cologne. The indicated position of the 5 anode was used for ^{10}Be AMS measurements and removed afterwards. Adapted from Stolz [57].

3.3 Sample Preparation

Since 2012 more than 400 samples have been produced and used at the MC-SNICS ion source at the Phoenix injector for AMS or test measurements. For every AMS measurement the correct and accurate preparation of the desired sample is the first step and an important point. The available copper or aluminum cathode are used depending on the desired beam to be extracted. The cathodes can be ordered from NEC in two sizes 1 mm and 6 mm inner diameter. The smaller cathodes are comparable in size to the cathodes used at the SO-110 ion source at the 6 MV Tandetron™ accelerator. The larger cathodes should only be used for test purposes, due to the large amount of unused material, which will not be sputtered by the cesium beam.

The amount of material that fits into a single small cathode depends to a large extend on the material, the material composition and grain size. A mixture of titanium hydride and silver, with a ratio of about 1:1 ranges between 2 and 7 mg, for example. On the other hand iron, zinc and silver material mixtures could weight up to 60 mg.

Before a mixture can be pressed to a cathode, it is crushed and mixed by pestle and mortar. Especially for material that comes in larger grain sizes this step is important. Through the addition of silver powder, the mixtures becomes more homogeneous, mechanically more stable and even more important this admixture ensures a good thermal conductivity to dissipate the heat generated by the ionizer, see Middleton [38] and Fifield [1].

As for any chemical, the rule is, anything taken from the storage box or glass must not return, even if unused. This means, that any amount of chemical that was taken from a container has to be used or disposed, to avoid any possible cross contamination. Therefore, it is of equally importance to use clean tools and instruments for handling and pressing, which is especially crucial for the used silver powder. As mentioned above, silver is used for the most samples, and any foreign particles inserted will therefore contaminate any following sample.

After the sample material is prepared, it can be filled into a clean cathode, which is, for this purpose, hold by a special pressing tool. The cathode is filled from the rear, while the front side is pressed to a pre-drilling pin, compare to Stolz [57]. The material is pressed into the cathode by a manual operated press. Attention must be paid to use pressures between 500 kPa and 750 kPa. At lower pressures the sample material is still not solid enough and parts of the powder can fall out, whereas higher pressures can lead to a deformation of the cathode itself. In this case, force is required to remove the cathode from the pressing tool and it is very likely that the cathode will not fit into the cathode wheel.

For the 6 mm cathodes no special pressing tool is actually available and therefore several procedures were tested. In the end two ways lead to at least acceptable results. But due to the fact, that this type of samples is used very rarely no further investigations where undertaken. The material can be pre-pressed to a 6 mm rod and than put into the cathode. Unfortunately, several pre-pressed samples broke apart when they were removed from the pressing tool. On the other hand, the material can be hammered directly into the cathode. But this approach also tents to deformations of the cathode itself, and therefore samples which does not fit into the sample wheel anymore. Therefore, it is recommendable to use small samples, because of a better stability, less used material and the better comparability to real measurements.

3.4 MC-SNICS Extraction Efficiency

The extraction efficiency of the used ion source is one key question depending to the overall transmission. Additional beam losses are generated at several points of the beam line, for example, losses due to different charge states, populated inside the stripper foil or degrader foils, but also losses from beam tuning and beam straggling. The overall transmission for the 10 MV Tandem accelerator was investigated by Schiffer [3]. The extraction efficiency ϵ is the fraction of the number $N(X^-)_{\text{extracted}}$ of extracted ions of a desired species X^- divided by the total number $N(X^-)_{\text{sample}}$ of ions, of the same species, inside the cathode.

$$\epsilon = \frac{N(X^-)_{\text{extracted}}}{N(X^-)_{\text{sample}}}$$

Therefore, the efficiency must be determined for each sample material and each extracted ion or molecule species individually. In the first step the cathode is weighted before and after the material was filled in, to get the exact amount of available sample material. Since during the sputter process also cathode material will be sputtered it is not possible to determine the correct weight of the used material afterwards. In a second step the low energy mass spectrometer was tuned to the desired mass and the beam current was measured at the Faraday cup after the 90° magnet on the low energy side, until the measurable current drops beyond several nA.

A typical performance curve of a sputter sample is shown in fig. 6. In this measurement iron powder was used, with an initial weight of 20.6 mg. It took 25.45 h until the measurable current dropped from 1.2 µA to 51 nA. Based on the measured total current over time and the initial weight, the extraction efficiency can be calculated.
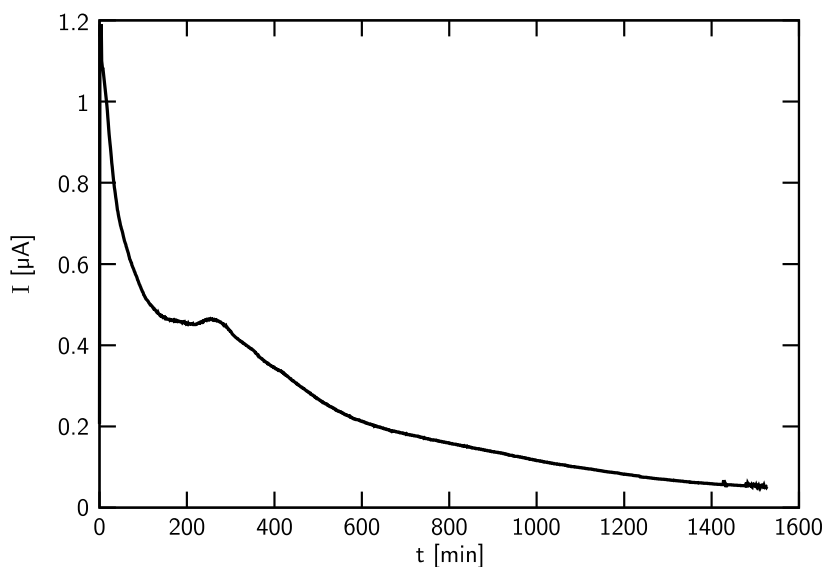

Figure 6: The extracted beam current over a total time span of 25.45 h from a single Fe sample, extracted from the MC-SNICS ion source and measured after the low energy mass spectrometer. The beam was extracted as $^{56}\text{FeO}^-$ from iron powder. The corresponding extraction efficiency is 0.62‰.

Table 1: Results from the extraction efficiency measurements at the MC-SNICS ion source. Given are the extracted beam, the type of material, the amount of sample material, the detected mean current and the resulting extraction efficiency.

Beam	Material	Sample mass [mg]	$\bar{I}$ [µA]	ϵ [‰]
$^{12}C^-$	C	10.0	20.74	38.20
$^{55}MnH^-$	Mn + TiH	11.3	0.03	0.09
$^{55}MnO^-$	MnO	20.8	0.15	0.36
$^{55}MnO^-$	MnO2	12.4	0.15	2.84
$^{56}FeO^-$	Fe (Powder)	20.6	0.24	0.62
$^{56}FeO^-$	Fe (Solid)	5.5	0.09	0.42

$$N_{\text{sample}} = \frac{m(X^-)}{M} \cdot N_A$$

$$N_{\text{extracted}} = \frac{\bar{I} \cdot t}{e}$$

Where m stands for the mass of the desired isotope, including molecular compositions and natural abundances. M represents the molar mass and N_A the Avogadro constant. $\bar{I}$ is the measured mean beam current at the Faraday cup after the magnet and t is the measurement time. The ratio, of the number of particles detected at the magnet Faraday cup and the number of particles from the sample, is defined as the extraction efficiency. The extraction efficiency was determined for C, MnH, MnO and Fe extracted from different types of material. Investigating different types of material is important since the resulting beam currents can vary considerably, see Middelton [38]. This test should also provide information about the best material for the manganese measurements, see Schiffer [3]. In the case of iron, the question could be clarified, if solid material can be a good alternative to iron powder. The results for each beam, the used material, the initial masses and the measured currents are given in tab. 1.

3.5 Commissioning of the new 135° Gas-Filled Magnet at the 10 MV Tandem

In the scope of this thesis, the new 135° gas-filled magnet was commissioned and tested. The magnet is installed at the 10 MV Tandem accelerator downstream the TOF stop detector, see fig. 4, to enlarge the available options for isobar separation and suppression of the new dedicated beam line for AMS measurements. The specifications and the design are inspired by Knie [36] and the 135° gas-filled magnet at the GAMS spectrometer in Munich, see Knie et al. [58]. It was ordered and assembled by Schiffer [3]. The new c-shape magnet has a bending radius of $\rho = 0.9$ m at a pole width of 300 mm and height of 50 mm. At an input current of 202 A and an input voltage of 60.3 V the maximum field strength of 1.25 T is generated. The corresponding vacuum chamber is equipped with five radial ports and two viewing ports along the entrance and exit optical axis, see fig. 7. Through the integrated ports, on the one hand it is possible
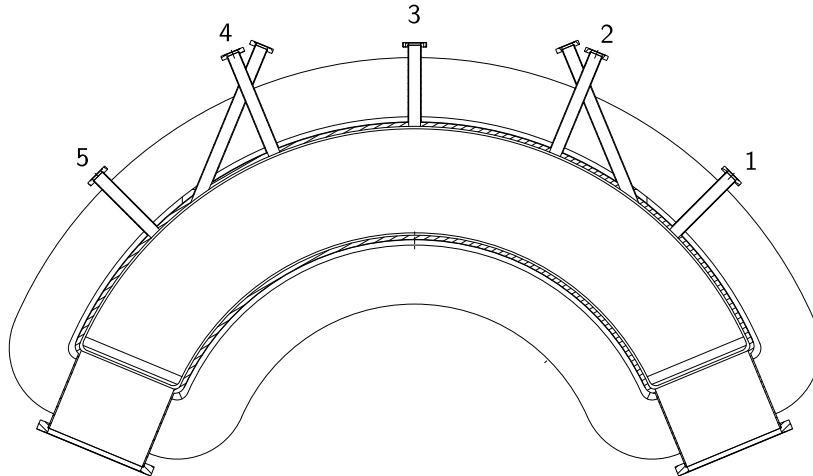
Figure 7: Technical drawing of the new 135° magnet at the AMS beam line of the 10 MV Tandem accelerator. Adapted from [59].

to adjust the magnet to the optical beam axis, and on the other hand it is possible to perform measurements of the magnetic field strength and homogeneity, see sec. 3.5.2. Along the optical axis the flight path has a total length of 2121 mm. The magnet was, for the first tests, equipped with a 2 µm Mylar entrance window. It was replaced afterwards by a 200 nm SiN window, which is described in sec. 5.4.1. The following section considers the technical aspects of the commissioning, the installation, programming and testing of the power supplies, magnetic field measurements concerning stability and homogeneity as well as the required gas handling system. First test measurements with stable ^{56,58}Fe as well as ^{58}Ni beams are discussed in chapter 5.

Table 2: Specifications of the new 135° gas-filled magnet. A complete list is given by Schiffer [3].

Pole form	C
Bending radius	0.9 m
Bending angle	135°
Pole width	300 mm
Pole gap	50 mm
Entrance edge angle	0°
Exit edge angle	0°
Magnetic flux	1.25 T
Current max.	202 A
Voltage max.	60.3 V
Radial ports	5
Viewing ports	2

3.5.1 Installation and Control of the new Power Supplies

According to the installation site, on top of concrete beam ceiling of the second basement, and the total weight of 14 t a solid substructure was required for the new gas-filled magnet. This consists of four double T-girders, see fig. 8a. On top of two additional transverse beams the actual substructure of the magnet is mounted, which was designed and constructed by Danfysik. It consists of three supporting feet, which allow a very accurate alignment of the magnet. A list of the specifications is given in tab. 2.

As mentioned before, the magnet is designed for a maximum current of 202 A at a required voltage of 60.3 V. To provide a sufficient electrical power three new SM 6000 - series DeltaElektronika power supplies were installed. Each of which has a power of 6400 W, at a maximum voltage of 80 V. This results in a total maximum current, in parallel operation mode, of 240 A. To use short connection cable between the power supplies and the magnet, the positioning should be as close as possible to the magnet. For this purpose, a frame was installed between the upper layer of the T-girders and the bottom side of the magnet, see fig. 8b. The inner dimensions of the frame are 358 mm height and 485 mm width and offers space for several 19" modules with a total height of 2×4 RU (rack units). Each of the new DeltaElektronika power supply has a height of 4 RU. The remaining 4 RU were used for the NMR 851PC control unit, used for magnetic field measurements, described in sec. 3.5.2.

All three power supplies are equipped with a 16-bit PSC-ETH Ethernet power supply controller, instead of the standard IEEE488 or RS232 controller, and two additional RJ45 connectors for a master/salve mode connection. This type of communication allows a fast and comprehensive
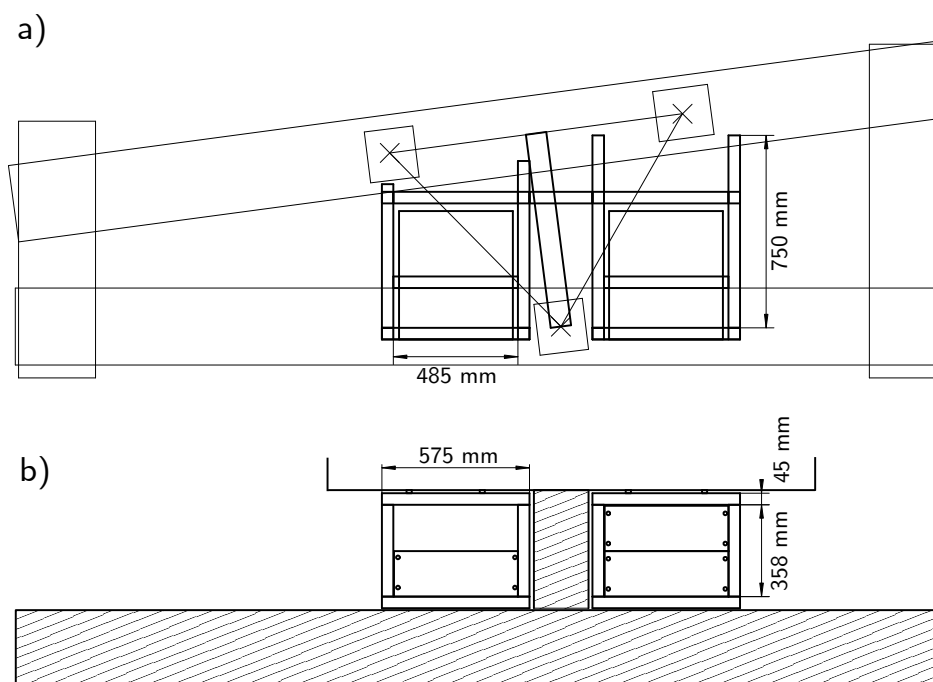

Figure 8: Technical drawing of the new substructure for the 135° gas-filled magnet and the new frame for the DeltaElektronika SM6000 power supplies. Figure a) shows the top view. Indicated are the large double T-girders from left to right and on both sides to distribute the weight of the magnet equally to several concrete beams, the floor is made of. Furthermore, it shows the three supporting feet and the new designed frame for the power supplies in the center. Figure b) shows the front view of the substructure and the three power supplies.
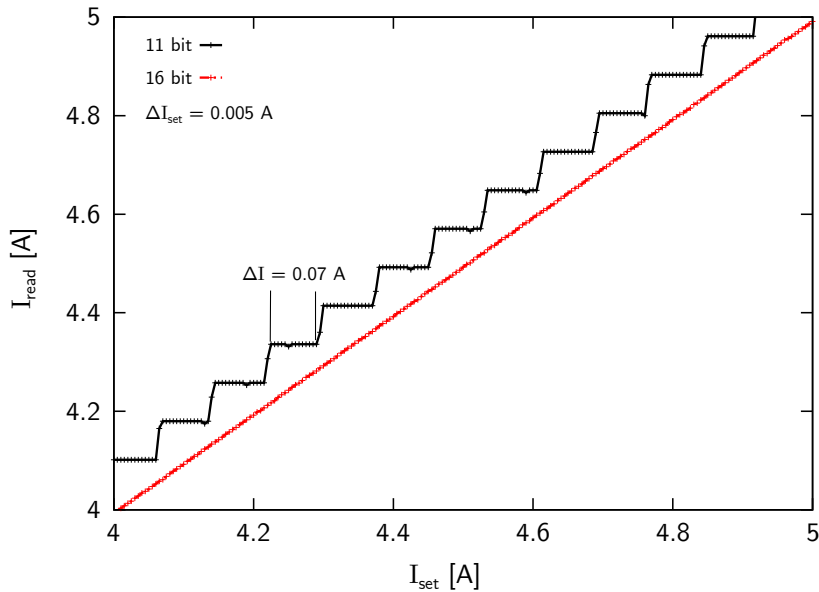
Figure 9: This plot shows a test with the new DeltaElektronika power supplies against the former used SPS solution. In both cases, 11-bit and 16-bit resolution, the magnetic current was tuned from 0 - 10 A over 2000 steps. Displayed on the y-axis is the read back value of the applied current. The step like shape is caused by the S7-200 SPS which is only able to control the output current with a resolution of 11-bit. Furthermore, an offset of 110 mA was detected for the old system, whereas the new system could reduce this by an order of magnitude.

control over a long distance. Furthermore, there are no additional hardware components required to transform or translate the commands send by the control computer or to extend the range of the signals, like for most of the other components. To operate the units in parallel mode, only a interconnection of the RJ45 master/slave ports is required. In this mode the units in slave mode will follow the master unit and it is therefore sufficient to control just the master unit. In the scope of this thesis a new software tool was written in LabVIEW™ to control all new DeltaElektronika power supplies. Furthermore, this new tool was fully integrated to the existing control software written by Feuerstein [10]. In this way it is possible not only to read and set new current values applied to the magnet, but also fully control all other parameters. This includes, the applied voltage, the maximum allowed voltage and current, the front panel behavior of the supplies and even detailed register manipulation to change the way of controlling the supplies (CC or CV).

By addressing the power supplies via Ethernet, a 16-bit digital connection is enabled. Until this point, the resolution of the magnetic current was limited to 11-bit, which corresponds to a step size of $\Delta I = 39$ mA for a maximum current of 80 A. This limitation is caused by the S7-200 PLC, and the signed 12-bit analogue output channels. With the new 16-bit digital system a step size of $\Delta I = 5$ mA is achieved. To show the effect an automated current trace was performed with both systems. The result is shown in fig. 9. For this test a step size of $\Delta I_{set} = 5$ mA was chosen. On the x-axis the set values and on the y-axis the read back values of the supply are displayed. The black line shows the old 11-bit resolution and the red line the new 16-bit resolution. Two important points become clear. On the one hand, the current changes are applied immediately by the new system, whereas with the old system it took 16 steps of ΔI_{set}, on average, until the output current really changes. During this time the output current stayed constant. In this case also a smooth mass spectrum would look stepped and might lead to false conclusions. On

the other hand the old spectrum is shifted by 110 mA. This was reduces by the new system by one order of magnitude. For this reason, another, identical power supply was installed at the 90° analyzing magnet of the low energy mass spectrometer of the AMS injector at the 10 MV Tandem accelerator. For this supply a similar software solution was designed and implemented to the existing control software.

3.5.2 Magnetic Field Homogeneity

Important for later AMS measurements, especially in combination with a gas-filled magnet, is the magnetic field homogeneity. By manufacturer specification the homogeneity is 4×10^{-4} within a radial range of ± 50 mm. To determine the magnetic field homogeneity a mount was designed and built to hold a NMR probe. This construction can be mounted to each of the five available radial ports. Furthermore, the position of the probe can be manually adjusted throughout the vacuum chamber, which allows to measure the magnetic field even during beam operation. In this way it is possible to determine the homogeneity of the magnetic field over a radial range of more than 200 mm. Based on the geometry of the NRM probe a 38 mm section at the innermost part of the vacuum chamber can not be investigated.

For these tests three BPH-851 probes and a corresponding NMR 851 PC control unit were used. The probes are able to measure magnetic fluxes in a range of 0.1 to 2.3 T, see [60]. In addition the probes are equipped with an integrated magnetoresistor, which is able to detect changes in the magnetic flux in a wide range and is used to trigger the actual nuclear magnetic resonance unit to search in the correct range. Very detailed explanations concerning the principal and development of NMR probes are given by Salzer et al. [61] and Levitt [62]. The control unit can be read out via a LabVIEW™ code, written by Herb [63]. The magnetic field was measured at all five ports, for two different currents, 45 A and 105 A. The measurement starts at each port from the innermost point of the vacuum chamber, from which the probe was pulled out in steps
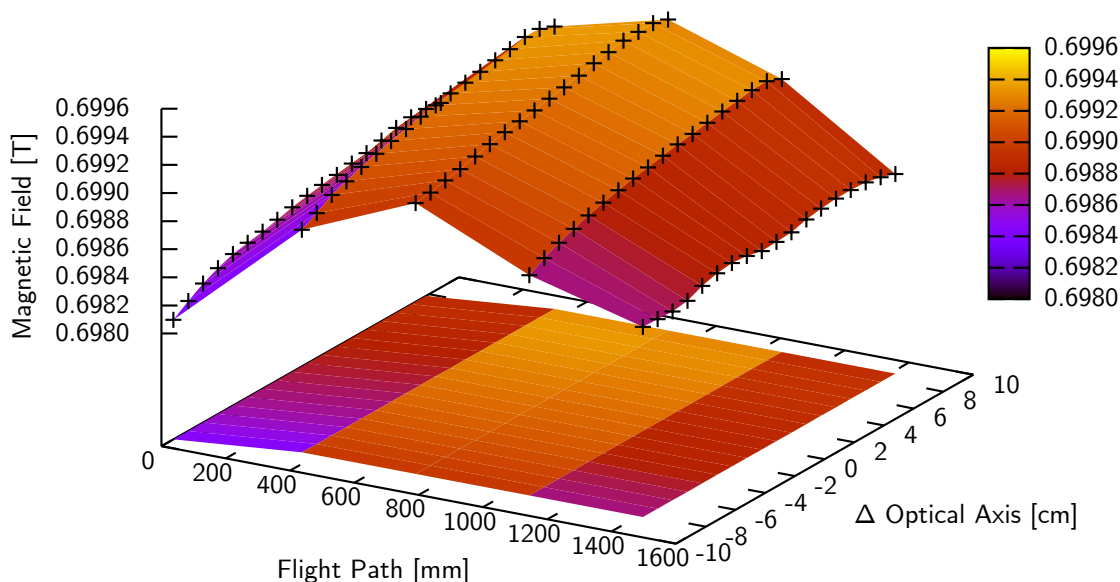

Figure 10: Measurement of the magnetic field homogeneity of the new 135° magnet at 105 A. On the xy plane the deviation from the optical axis the flight path throughout the magnet, starting from the first radial port, are shown. The z-axis shows the measured magnetic field at each investigated point.

of 10 mm. The corresponding measuring error of the probe is 2×10^{-6} T and was determined by multiple measurements at the same position.

A second limitation for this measurements are field inhomogeneities on both sides of the vacuum chamber along the optical axes. A reliable and reproducible measurement was only possible in a region ±80 mm around the optical axis. Beyond this area the probe was not able to lock the resonance frequency. The tests revealed that the magnetoresistor is working fine, even larger changes of the field are detected correctly. However no resonance was detected by the NMR probe itself. Nevertheless, the major part of the magnetic field region could be investigated concerning the magnetic field strength and homogeneity. In total 91 points for each set current value were investigated. The resulting field map, for an applied current of 105 A, is shown in fig. 10. On the xy plane the deviation from the optical axis and the flight path throughout the magnet are shown, starting from the first radial port. The z-axis shows the measured magnetic field at each investigated point. The mean of the detected field was 0.6989(8) T over the whole magnetic field region. Danfysik defines the field homogeneity by the following formula.

$$ B_{\text{hom}} = 1 - \frac{B}{B_{\text{max}}} $$

Where B is the field measured on the optical axis and B_{max} the maximum measured field strength. In what follows, this definition is used to compare the determined homogeneity and the specified homogeneity. The measured magnetic fluxes and the calculated homogeneities for each current and all five radial ports, are given in tab. 3. The values for 93.50 A and 196.05 A are reference values determined by Danfysik and were provided upon request after the measurements with 45 A and 105 A were carried out. According to the very good agreement of the data, it was decided not to repeat the very time consuming measurements with the exact same currents Danfysik

Table 3: Measured magnetic field homogeneity of the new 135° magnet for 45 A and 105 A input current. At each radial viewing port the magnetic flux was determined at 18 different positions around the optic axis. The homogeneity values for 93.50 A and 196.05 A were given by Danfysik for comparison. The numbers of the viewing ports are related to fig. 7

Current [A]	Radial port	$\overline{B}$ [T]	B_{hom} [$\times 10^{-4}$] (±50 mm)	B_{hom} [$\times 10^{-4}$] overall
	1	0.3013	0.10	0.10
	2	0.3015	0.03	0.03
45.00	3	0.3015	0.03	0.03
	4	0.3014	0.33	0.33
	5	0.3012	1.00	1.66
	1	0.6984	1.48	2.39
	2	0.6991	1.44	2.09
105.00	3	0.6993	1.64	2.00
	4	0.6990	1.37	1.89
	5	0.6986	1.07	1.09
93.50	3	0.6205	1.39	
196.05	3	1.2502	2.45	

used. Remarkable is the decreasing homogeneity for larger applied currents. Nevertheless, the determined homogeneity is in all cases and for more than $\pm 50\,\text{mm}$ around the optical axes better than the requested specification.

3.5.3 Gas-System Design and Construction

To use the new $135°$ magnet in gas-filled mode, it is necessary, on the one hand to install an entrance window to keep the volume sealed and on the other hand a dedicated gas handling system is required. For the first test a simple $2\,\mu\text{m}$ thick Mylar window was used. The foil was glued to a $58\,\text{mm}$ large aperture ring and mounted to the ISO-300 entrance flange of the magnet vacuum chamber. In this way a mechanical stable window was used with a very large acceptance. On the downside, the resulting energy loss was very high and is absolutely not recommended for real AMS measurements. For later measurements a $200\,\text{nm}$ thick and $12 \times 12\,\text{mm}^2$ wide SiN window was used, which reduces the energy loss by an order of magnitude.

Apart from the important entrance window, the gas handling system is of equal relevance. The new gas system has to fulfill several different tasks. On the one hand, the vacuum chamber of the magnet and the ionization chamber must be evacuated to prevacuum and high vacuum separately. On the other hand the different required gases, isobutane gas as detector gas and N_2 gas for the magnet itself, must be pumped into each region individually. Special attention must be payed to the large pressure differences between the used gas cylinder, $200\,\text{bar}$, and the maximum pressure the installed foils are capable to hold, which is in the order of several hundred mbar. Therefore, very fine valves were used to control the gas flow. Furthermore, the system must be equipped with different bypasses, for pressure compensation between the regions, for venting as well as pressure adjusting. Finally, it has to be equipped with different pressure probes.
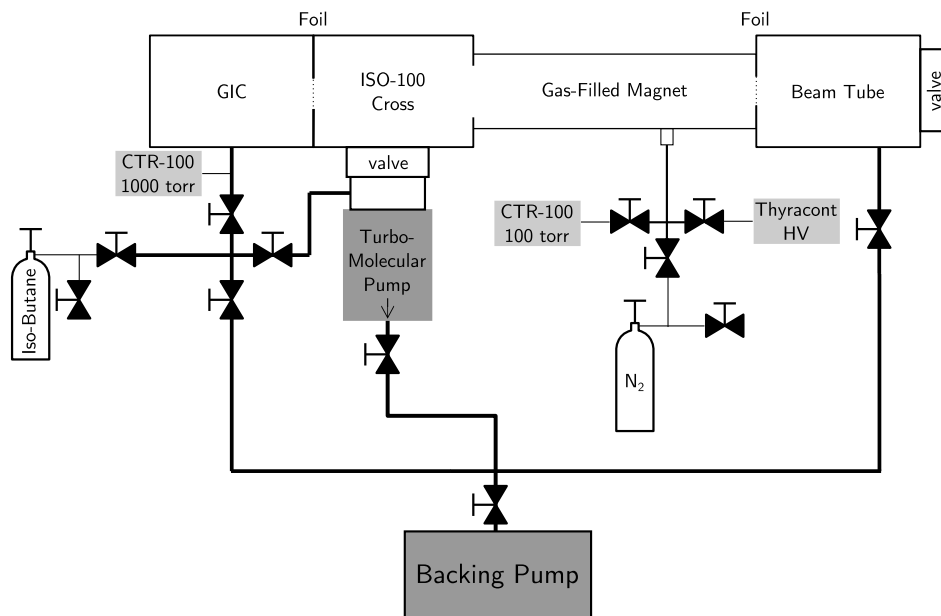

Figure 11: Gas system of the new $135°$ gas-filled magnet. The system is able to control the pressure inside the ionization chamber and the vacuum chamber of the magnet individually. It handles both required gases, isobutane gas and N_2 gas. Furthermore, it is possible on the one hand to evacuate the whole system down to $10^{-7}\,\text{mbar}$ or, on the other hand to vent both sections, without destroying the thin windows, in a controlled way.

As the working principal of the standard probes for high vacuum is based on the ionization of particles and the probes where calibrated for air, different types of probes are required to measure the high vacuum on the one hand and the gas pressure on the other hand. The working principal of the CTR-100 probes, used for the gas system, is based on the deformation of a membrane and is therefore an absolute measurement, at least in the desired pressure region between 0.01 mbar and 100 mbar. The designed and installed system is displayed in fig. 11.

One difficulty of the setup is to change the entrance foil of the magnet. In this case, a part of the beam tube in front of the magnet has to be vented and dismounted, but without venting the TOF stop detector. Therefore, an additional gate valve was installed, see fig. 11. In this way another isolated region was created and had to be connected to the whole gas system. This has to be kept in mind to not destroy the entrance foil of the magnet or the TOF detector system, if installed.

3.6 Setup and Characterization of the 10 Anode Gas Ionization Chamber

After the new injection system and the AMS beam line were finished, first measurements were performed with a 2 anode ionization chamber after the 30° ESA, see fig. 4. Like parts of the new established injection system, also a 10 anode ionization chamber was obtained from the University of Utrecht, see van der Borg et al. [64]. In the course of this thesis the detector was composed and tested. Due to the limited amount of ADC input channels of the MPA3 data acquisition hardware, only eight signals can be detected, see chapter 4. Hereinafter the detector is yet called 10 anode ionization chamber according to the number of anodes installed. During several measurements, the total energy resolution, the energy loss along the anodes and separation factors for different isobutane gas pressures were investigated. For this purpose stable ^{12}C, ^{40}Ca, ^{39}K, ^{48}Ti, ^{58}Fe and ^{58}Ni beams were used.

3.6.1 Detector Design

The 10 anode ionization chamber consists of a cylindric hull, which is closed on the backside by a 19 mm thick flange. On the one hand, this is used for the required feedthroughs and on the other hand to hold the inner part of the detector, see fig. 12. Therefore, for any maintenance, the whole detector can be pulled out by the back plate. To not damage the sensitive parts, two guiding disks, one at the front and one at the end of the inner detector part are mounted to a upper and a lower guiding plate. The upper plate is also used to hold and fix all required cables. In total the back flange is equipped with fourteen BNC and one SHV ports as well as a gas feedthrough. In this way not only the 10 anodes can be read out but also the mounted frames and the electrical ground can be connected.

On the front side the detector has two 25 mm flanges stacked onto each other. The outer most is equipped with a 4" port to connect the detector housing to the beam guidance system. The inner flange is designed to hold the entrance window. To reduce the drift length of the ions outside the active detector volume, the window is mounted to a 52.5 mm long tube with a diameter of 20 mm. The inner part of the detector consists of the cathode, which is formed like a tub, the ten anodes and in between the Frisch-Grid. The cathode is mounted to the lower guiding plate via 20 mm long, nonconductive plastic rods. The Frisch-Grid as well as the anodes are mounted to the upper guiding plate, also by nonconductive plastic rods. In this way the required stability, for such a long detector, is provided.
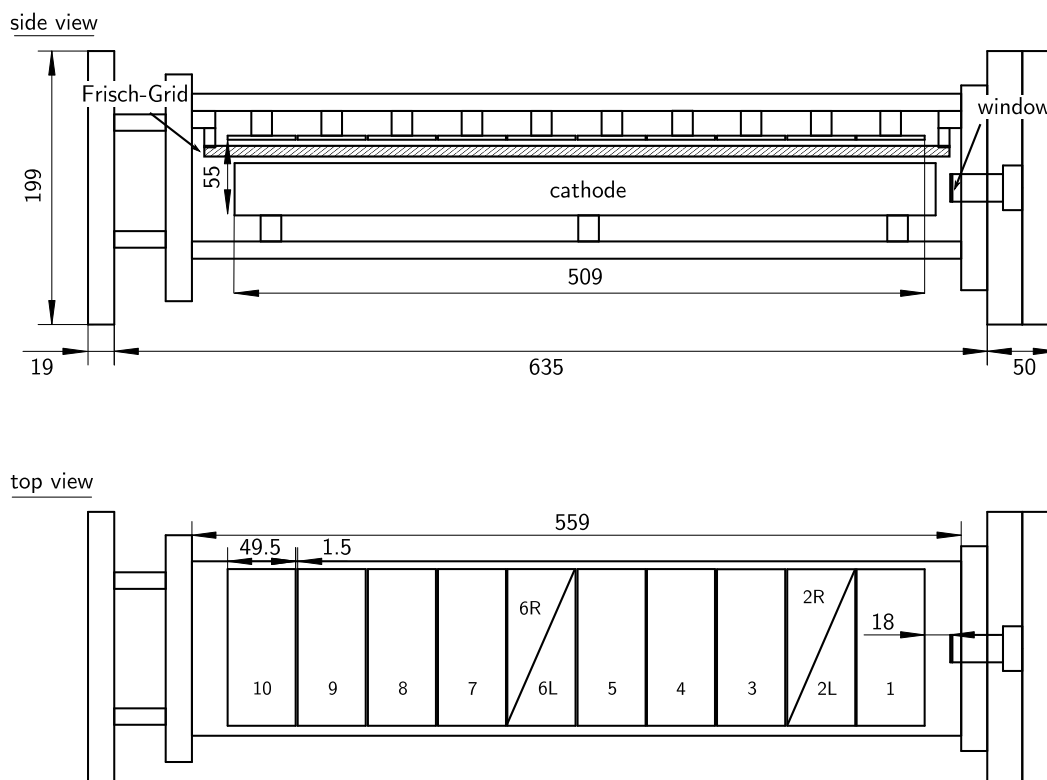
side view

top view

Figure 12: This technical drawing of the 10 anode ionization chamber shows a side view and a top view of the detector. The left side is the backside of the detector and the beam can enter from the right side through a window, mounted to a 20 mm ⌀ tube. The side view drawing shows the back plate and the nonconductive mounting rods where the rest of the detector is mounted to. In this way the detector is completely removable to the backside.

The active detector volume is 55 mm high and 509 mm long. The distance between the Frisch-Grid and the anode is 15 mm and the distance between the Frisch-Grid and the cathode is 40 mm. All anodes are the same size, 114 mm wide and 49.5 mm long, with an 1.5 mm gap in between. The distance between the entrance window and the first anode is 18 mm.

3.6.2 Test Measurements at the 10 MV Tandem Accelerator

After composing all detector parts and installing a new entrance window, several test measurements were performed to determine the total energy resolution E_{res}, test different gas pressures as well as anode and Frisch-Grid voltages. Furthermore, the data acquisition system was configured to record on all eight available signals parallel. The measurements, related to the ion energy loss, were conducted within the scope of the Bachelor thesis of Aron Pfeil. For this first test a 2 µm Mylar foil was used for the detector entrance window. This has a higher mechanical stability compared to a 200 nm SiN window, used for the later measurements, but a much larger energy loss is created.

To investigate several aspects of the detector, a set of six different stable nuclides was selected. First of all the standard AMS nuclide ^{12}C to get an easy to make and well known beam without any notable contamination. Furthermore, ^{40}Ca and ^{39}K beams were used with regard to the measurements of ^{41}Ca and the corresponding isobar ^{41}K. In this context also a ^{48}Ti beam was measured, which is used to calibrate the ^{41}Ca spectra, see sec. 6.2.1. The last nuclides used for

measurements were ^{58}Fe and ^{58}Ni, with respect to the AMS radionuclide ^{60}Fe, which is a very good candidate for AMS measurements at the 10 MV Tandem accelerator in combination with the new 135° gas-filled magnet. A detailed investigation on ^{58}Fe and ^{58}Ni, beam tuning, separation and measurements are given in chapter 5. For these first tests, the 10 anode ionization chamber was mounted after the high energy 30° ESA at the 10 MV Tandem accelerator, see fig. 4. Before the measurement starts, all used main amplifiers were calibrated by a pulser signal. This signal is very clear and is converted by the ADC's into a single channel. During the calibration every amplifier was tuned until the pulser signal was detected at the same channel in each spectrum. In this way it is possible to compare signals between each anode and draw conclusion to the deposited amount of energy.

Detector Tests with ^{12}C

For the first test run, a ^{12}C^{5+} beam was chosen with a beam energy of 48 MeV. The detector voltages were set to 450 V and 225 V for the anodes and the Frisch-Grid, respectively. Based on simulations made with LISE++ and SRIM the required isobutane gas pressure was calculated between 85 mbar to 95 mbar, according to a stopping distance between 374.5 mm to 424 mm corresponding to the beginning and the end of the eights anode. The detector gas pressure was investigated in steps of 5 mbar and an optimal pressure was determined at 90 mbar. After summing the detector signals for all eight anodes, the resulting 1-dim spectrum is fitted by a Gaussian distribution and the total energy resolution E_{res} can be calculated by the following equation.

$$E_{res} = \frac{2\sqrt{2\ln(2)} \cdot \sigma}{\mu} \tag{3.1}$$

Where σ and μ are the width and the center of a signal distribution, respectively, see Knoll [65]. The resolution was determined to $E_{res} = 1.72(1)\%$. The measured peak position inside the 2-dim histogram, see fig. 13a as well as the determined total energy resolution, see fig. 13b was
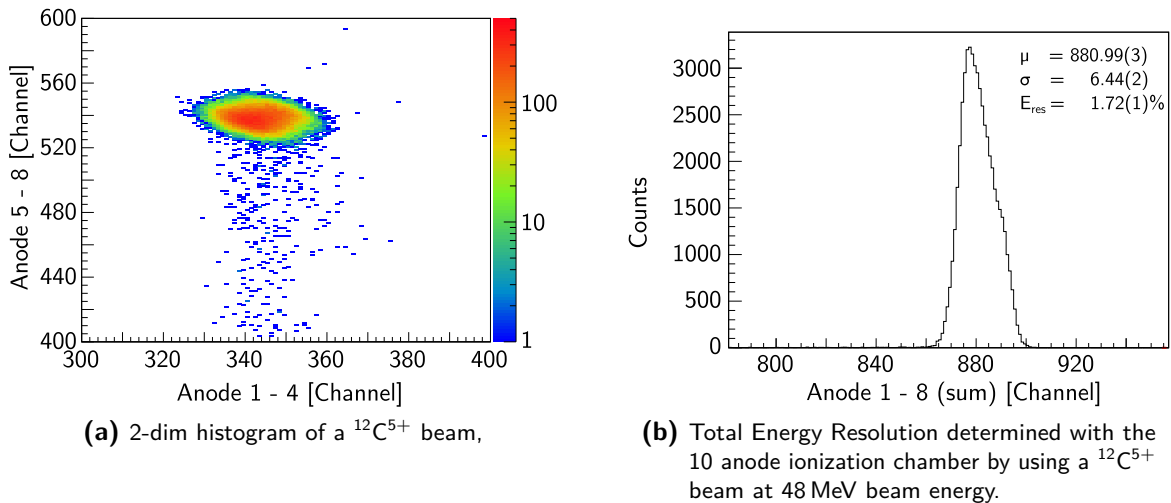
(a) 2-dim histogram of a ^{12}C^{5+} beam,

(b) Total Energy Resolution determined with the 10 anode ionization chamber by using a ^{12}C^{5+} beam at 48 MeV beam energy.

Figure 13: The figure shows the results of the first test measurement with the 10 anode ionization chamber and a ^{12}C^{5+} beam with 48 MeV beam energy. Figure a) shows the 2-dim histogram achieved by plotting the signal of the first 4 anodes against the last 4 anodes. Figure b) shows the determined total energy resolution E_{res} by combining the signals of all 8 anodes.

reproducible also after restarting everything from scratch and refocusing the beam the next day. Furthermore, this investigation revealed how important the correct gas pressure inside the detector is, for the later measurement results. For higher pressures, as predicted by the calculations, the particles are stopped before they reach the eighth anode. As a consequence, the 2-dim histogram does not contain every signal, due to the coincidence condition set for each anode, see sec. 4.1. On the other hand, for lower pressures, not all particles are stopped withing the active detector volume and a part of the beam energy is left undetected. A second problem arising from a wrong pressure is a deterioration of the total energy resolution. At a pressure of 80 mbar, for example, the energy resolution drops to $E_{res} = 3.6\,\%$.

Detector tests with ^{40}Ca, ^{39}K and ^{48}Ti

For a second set of test measurements ^{40}Ca was chosen, which represents a good pilot beam to determine and test required system settings for later AMS measurements with ^{41}Ca. Therefore, also ^{39}K was investigated as a pilot beam for the upcoming isobar ^{41}K. In this way, on the one hand, it was possible to determine the energy loss throughout the detector and compare it to the simulated values of SRIM. On the other hand it was also possible to test different anode combinations for the later data analysis. The detector was calibrated with ^{48}Ti, to ensure the correct identification of the components. In the context of this measurement also different isobutane gas pressures were tested. The best result was achieved at a pressure of 21 mbar. For this pressure the total energy resolution for ^{40}Ca is $E_{res} = 3.2\,\%$. In a second step the energy loss per anode was investigated and compared to the simulations done with SRIM. For this purpose, the total beam energy was set to 63.09 MeV for ^{40}Ca^{7+} after the 10 MV Tandem accelerator. Due to the relatively thick detector entrance window, 8.31 MeV for ^{40}Ca and 7.74 MeV for ^{39}K are lost inside the Mylar foil, calculated with LISE++. The remaining particle energy of 54.78 MeV had to be deposited within the 424.5 mm of active detector length, between the first and the eighth anode, including the distance between the entrance window and the first anode. In this
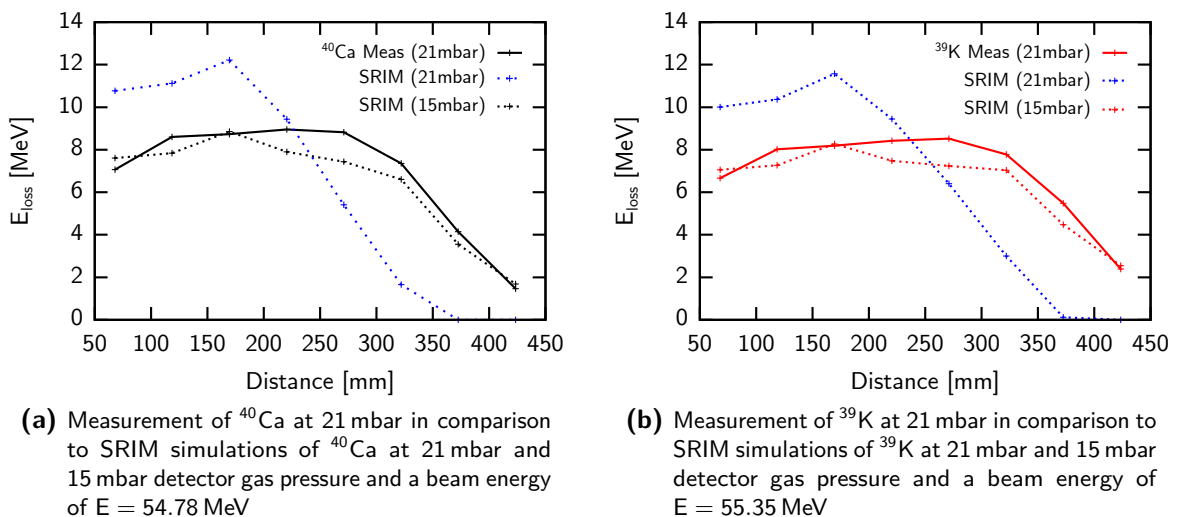

(a) Measurement of ^{40}Ca at 21 mbar in comparison to SRIM simulations of ^{40}Ca at 21 mbar and 15 mbar detector gas pressure and a beam energy of $E = 54.78$ MeV

(b) Measurement of ^{39}K at 21 mbar in comparison to SRIM simulations of ^{39}K at 21 mbar and 15 mbar detector gas pressure and a beam energy of $E = 55.35$ MeV

Figure 14: The figure shows a comparison between the measured and the simulated energy loss of ^{40}Ca and ^{39}K at different gas pressures within the 10 anode ionization chamber. During the measurement, the pressure was set to 21 mbar. The simulations, marked with dotted lines, were done with SRIM, including the energy loss inside the entrance foil.
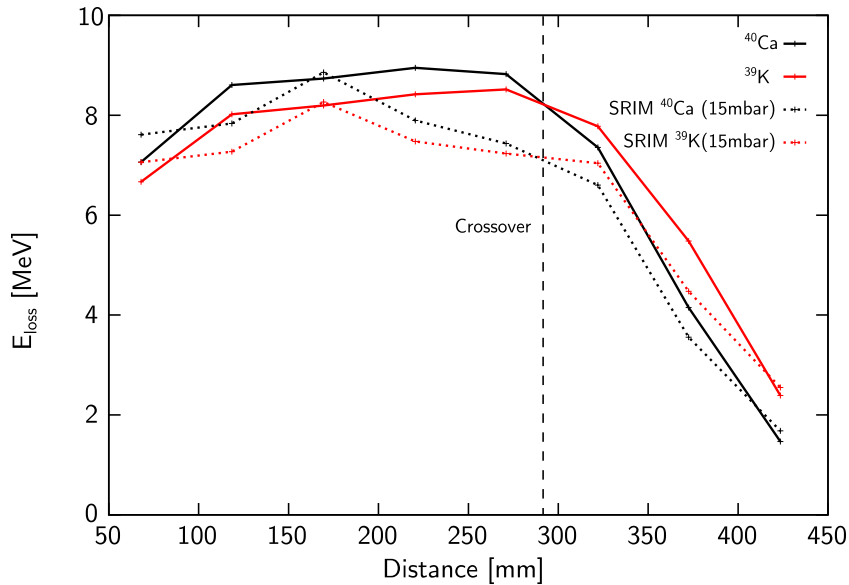
Figure 15: The figure shows the determined crossover point of the energy loss of ^{40}Ca and ^{39}K inside the 10 anode ionization chamber at 21 mbar isobutane gas pressure and a beam energy of 54.78 MeV and 55.35 MeV after the entrance foil, respectively. The crossover point is at 293 mm measured from the beginning of the detector, and therefore at the sixth anode. The SRIM simulation, marked with dotted lines, predict the same point.

way the sum of all anode signals into a single spectrum represents the total energy deposited in the detector. In a second step each channel is assigned to a specific energy based on the calibration done beforehand. Therefore, it is possible to determine the energy loss at each anode individually. The resulting curves, and the corresponding SRIM simulations are shown in fig. 14a and in fig. 14b for ^{40}Ca and ^{39}K, respectively. The dotted lines indicate the calculated values for 21 mbar and 15 mbar isobutane gas pressure.

For both nuclides the simulation with the lower pressure fits much better to the measurement than the simulation with the set pressure. There are several reasons that could explain this discrepancy. First reason could be an incorrect measurement of the isobutane gas pressure. The working principle of the probe is based on the deformation of a membrane, and therefore an absolute measurement, and not depending on a calibration or other correction factors but on the orientation of the probe itself. A second reason could be the used isobutane gas itself. Although, the gas is ordered each time with the same degree of purity of 99.95%, the quality and the required pressure varies. This behavior was observed repeatedly at the 6 MV Tandetron™ accelerator and the used 4 anode ionization chamber.[2] The third reason, that has to be taken into account, is the detector itself. Since anode, Frisch-Grid and cathode are shifted to each other in the direction of the particles flight path and the Frisch-Grid is equipped with a solid wide frame, the generated electric field could be inhomogeneous and distort the detected charges.

As a result from the measurements and the simulations, also the crossover point of Ca and K inside the detector could be determined. Based on their different energy loss inside the detector gas, Ca deposit more energy to the forward anodes, whereas K deposit more energy on the rear anodes, the energy loss curves crosses at a certain point. The so called crossover point is shown in fig. 15. The point was determined at 293 mm, measured from the beginning of the detector, which belongs to the sixth anode. Therefore, to get the optimal separation between Ca and K

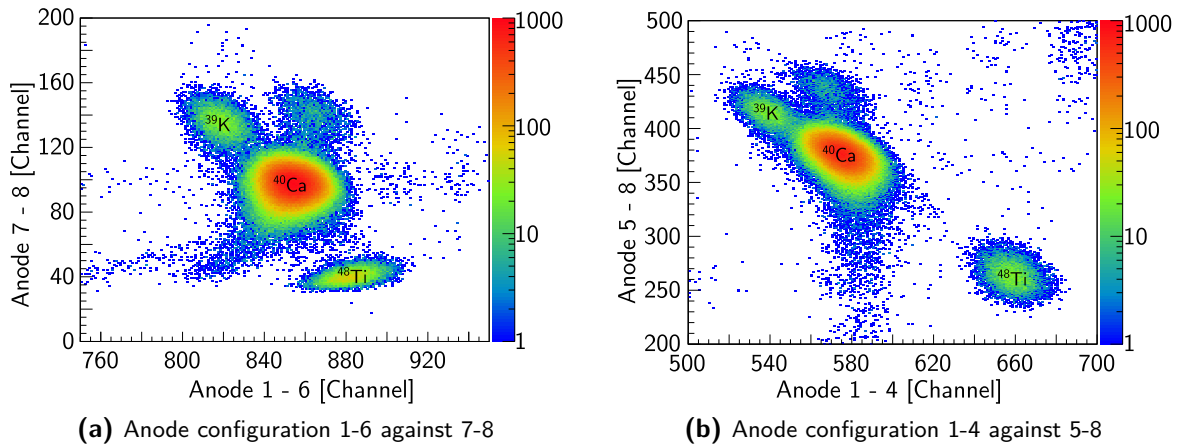[2] private communication Dr. Stefan Heinze

(a) Anode configuration 1-6 against 7-8

(b) Anode configuration 1-4 against 5-8

Figure 16: Both plots show the combined spectrum of the same ^{40}Ca, ^{39}K and ^{48}Ti measurements. All three measurements were performed with an initial beam energy of 63.09 MeV and an isobutane gas pressure of 21 mbar. Figure a) shows the sum of anodes 1-6 plotted again anodes 7-8 which results in a separation factor of $S_f = 2.19$. Figure b) shows the sum of anodes 1-4 plotted again anodes 5-8 with a separation factor of $S_f = 1.88$.

in a 2-dim histogram plot, anodes 1-6 should be plotted against anodes 7-8. This was done in fig. 16a and should be compared to the anode combination shown in fig. 16b, where anodes 1-4 are plotted against anodes 5-8. The separation factor between Ca and K with the optimal anode combination is $S_f = 2.19$ and therefore 16.7% better in comparison to a combination in which the detector is divided into to equal parts, $S_f = 1.88$.

Detector tests with ^{58}Fe and ^{58}Ni

A third test was performed with ^{58}Fe and ^{58}Ni beams, with regard to the upcoming interest for ^{60}Fe measurements at the 10 MV Tandem accelerator. The measurements include investigations concerning the separation, suppression and total energy resolution achievable with the new gas-filled magnet, see chapter 5. For this purpose ^{58}Fe^{9+} and ^{58}Ni^{9+} beams were tuned throughout the system with an energy of 85 MeV, which corresponds to an beam energy of 73.75 MeV and 72.90 MeV after the entrance foil, respectively. The 9^+ charge state was chosen according to the high yield of about 27% achievable at a terminal voltage of 8.5 MV, calculated from eq. 2.7. Also for Fe and Ni, several isobutane gas pressures were tested and calculated with SRIM. Best results were achieved at a pressure of 24 mbar. The resulting energy loss curve is given in fig. 17a and fig. 17b, respectively. For this pressure the total energy resolution of ^{58}Fe is determined to $E_{res} = 2.5\%$.

Similar to the results achieved for ^{40}Ca and ^{39}K, also in this case, the simulation fits best to the measurement for a 6 mbar lower isobutane gas pressure. This was tested several times and at different runs, after restarting the whole system, tuning the beam from scratch and refilling the detector with fresh isobutane gas. Therefore, the explanations given above seem to be substantiate with this additional measurement. For the given pressure and beam energy the crossover point of energy loss is right after the end of the fourth anode. The resulting 2-dim histogram for anodes 1-4 plotted against anodes 5-8 is given in fig. 18a. In this configuration a separation factor of $S_f = 2.49$ was achieved. For comparison only, the 2-dim histogram with anode 1-6 plotted against 7-8 is given in fig. 18b, which results in a significantly worse separation factor of $S_f = 1.46$.
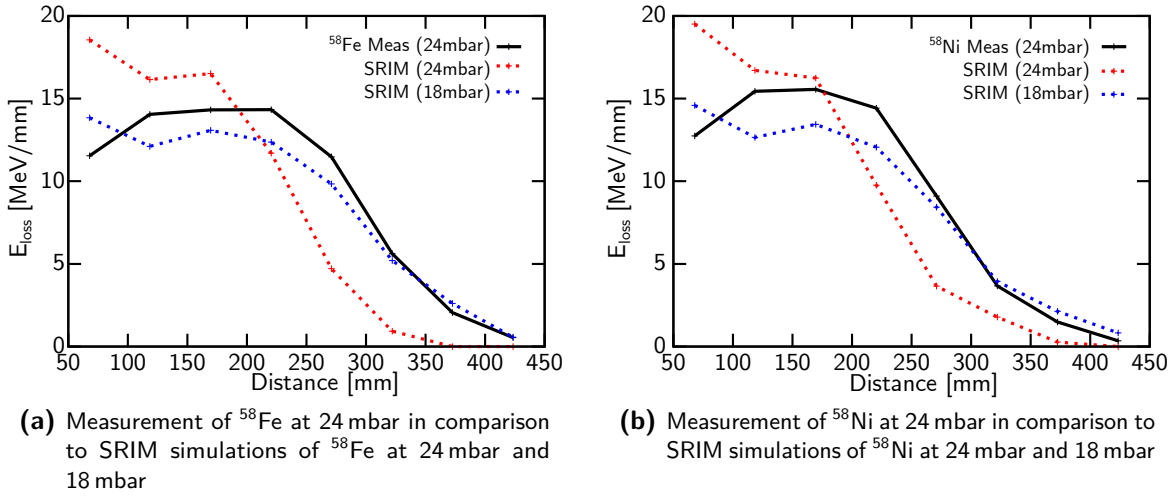
(a) Measurement of ^{58}Fe at 24 mbar in comparison to SRIM simulations of ^{58}Fe at 24 mbar and 18 mbar

(b) Measurement of ^{58}Ni at 24 mbar in comparison to SRIM simulations of ^{58}Ni at 24 mbar and 18 mbar

Figure 17: The figure shows a comparison between the measured and the simulated energy loss of ^{58}Fe and ^{58}Ni within the 10 anode ionization chamber at an initial beam energy of 85 MeV. The simulations, marked with dotted lines, were done with SRIM in consideration of the individual energy inside the entrance foil.

(a) Anode configuration 1-4 against 5-8

(b) Anode configuration 1-6 against 7-8
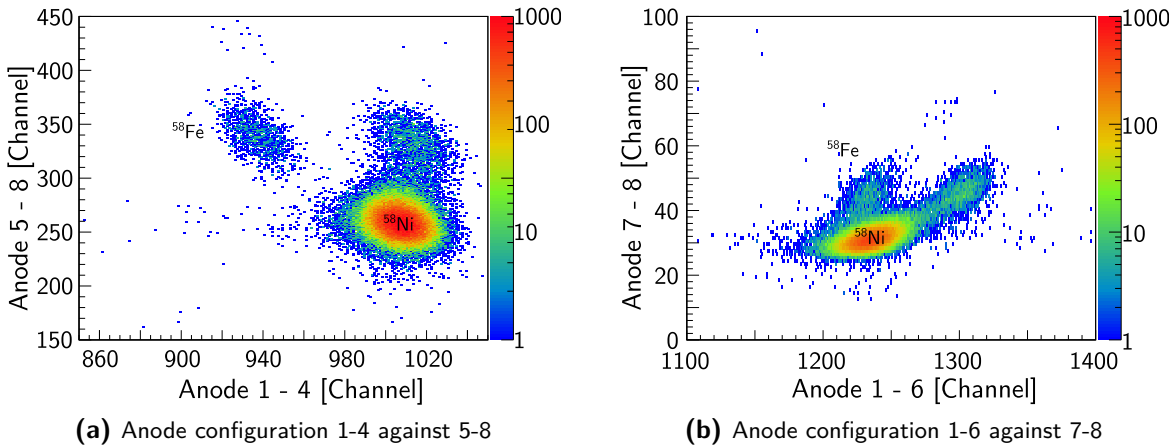
Figure 18: Both plots show the combined spectrum of the same ^{58}Fe and ^{58}Ni measurement. The measurements were performed with an initial beam energy of 85 MeV and an isobutane gas pressure of 24 mbar. Figure a) shows the sum of anodes 1-4 plotted again anodes 5-8 which results in a separation factor of $S_f = 2.89$. For the anode combination of 1-6 plotted against 7-8 the separation factor $S_f = 1.46$ is significantly worse.

For measurements, after the gas-filled magnet described later in this thesis, see chapter 5, the mean energy of ^{58}Fe and ^{58}Ni will not be the same according to the differences in energy loss based on the $\Delta Z = 2$. But due to the appearing energy straggling, the probability of ^{58}Ni ions entering the detector with the same energy than the ^{58}Fe ions, is not neglectable. Therefore, different measurements were performed at different energies, which represents different setup constellations all linked to the reference beam energy of 100 MeV and the 10^+ change state used for the later investigations. In this way it was possible to determine the pure detector separation of both components, without any additional foils or gas, at equivalent beam energies.
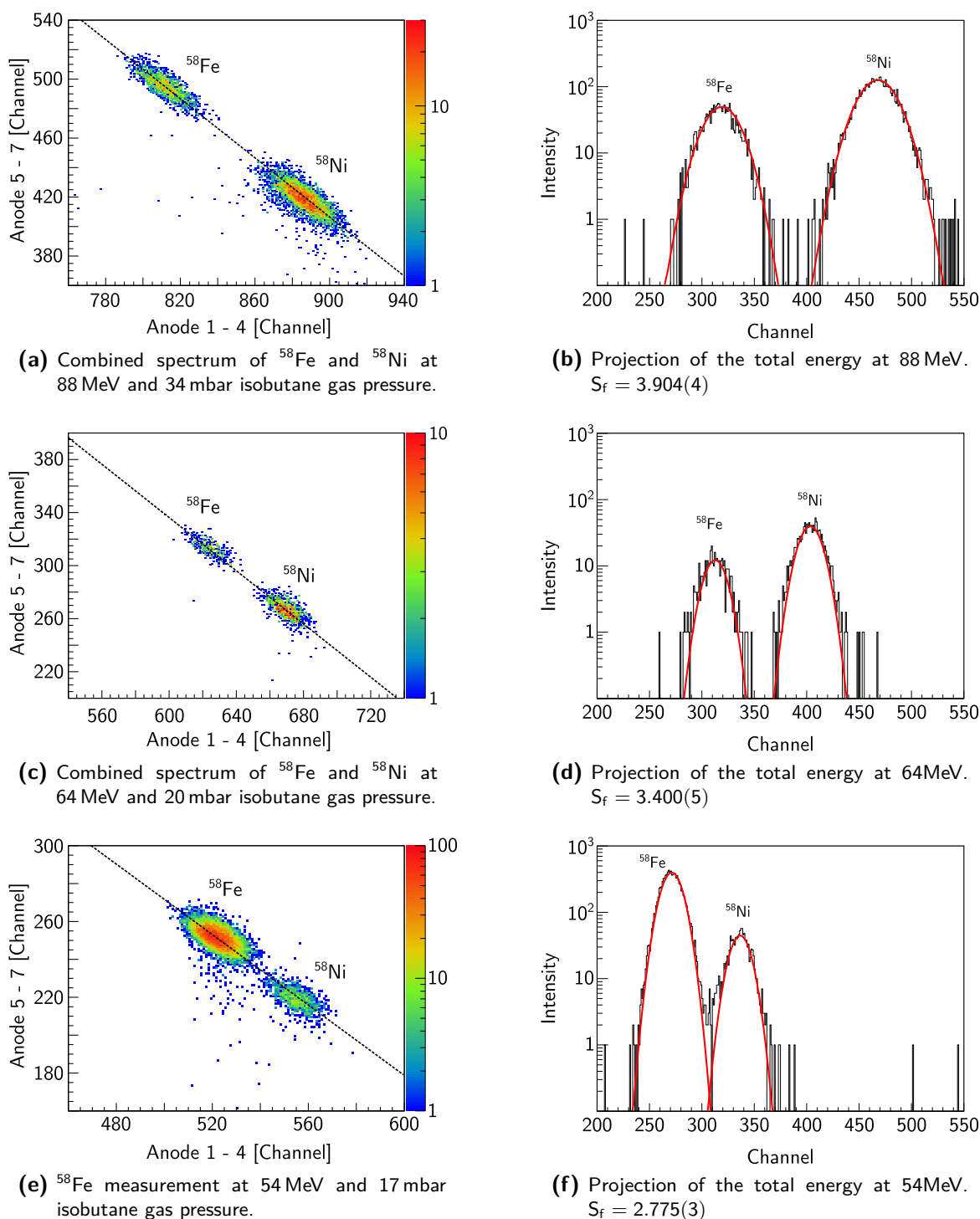
(a) Combined spectrum of ^{58}Fe and ^{58}Ni at 88 MeV and 34 mbar isobutane gas pressure.

(b) Projection of the total energy at 88 MeV. $S_f = 3.904(4)$

(c) Combined spectrum of ^{58}Fe and ^{58}Ni at 64 MeV and 20 mbar isobutane gas pressure.

(d) Projection of the total energy at 64 MeV. $S_f = 3.400(5)$

(e) ^{58}Fe measurement at 54 MeV and 17 mbar isobutane gas pressure.

(f) Projection of the total energy at 54 MeV. $S_f = 2.775(3)$

Figure 19: Figure a), c) and e) show the measurements at 88 MeV, 64 MeV and 54 MeV beam energy, respectively. The diagonal line was added to indicate the line of total energy deposition. Figures b), d) and f) show the corresponding projection to the indicated diagonal line, to determine the separation factor. The comparison of both measurements indicates the importance of high beam energies inside the ionization chamber and therefore thinner windows. The results are given in tab. 4. All measurements were conducted with the 10 anode ionization chamber, mounted after the 30° ESA, see fig. 4.

Table 4: Separation factors S_f for ^{58}Fe and ^{58}Ni at different beam energies with an initial energy of 100 MeV at the 10^+ charge state. Measured with the 10 anode ionization chamber at the 10 MV Tandem accelerator. The suppression S is calculated based on the measured distributions at a transmission of ^{58}Fe of 99.9%.

E [MeV]	Isotope	Det. [mbar]	σ [a.u.]	μ [a.u.]	S_f	$S\,(T_R = 99.9\%)$
88	^{58}Fe	34	14.94(2)	317.17(2)	3.90	8×10^9
	^{58}Ni		16.44(2)	467.48(3)		
64	^{58}Fe	20	10.94(2)	311.72(2)	3.40	1×10^7
	^{58}Ni		11.07(2)	403.54(2)		
54	^{58}Fe	17	9.49(1)	270.90(1)	2.77	9×10^3
	^{58}Ni		9.62(2)	335.95(2)		

In a first run ^{58}Fe^{10+} and ^{58}Ni^{10+} were measured at 88 MeV, which represents the beam energy after passing the 2 μm Mylar foil, used during the first tests as entrance to the magnet chamber. The next two measurements were performed at 64 MeV and 54 MeV which corresponds to a ^{58}Fe measurement with two 200 nm SiN entrance foils and 3.5 mbar N_2 gas pressure and the other one to a measurement with a 2 μm Mylar, a 200 nm SiN and 3.5 mbar N_2 gas pressure. The results as well as the isobutane gas pressures used at the ionization chamber are given in fig. 19. The sub-figures fig. 19a, fig. 19c and fig. 19e show the individual result of the measurements at 88 MeV, 64 MeV and 54 MeV as well as the total energy diagonal as a 2-dim histogram of anode 1, 2L, 2R ,3+4 against anode 5, 6L, 6R, 7. The sub-figures fig. 19b, fig. 19d and fig. 19f, are generated by projecting the measurement along the total energy diagonal. In this way a separation factor was calculated by fitting the resulting 1-dim spectra with a Gaussian distribution, see eq. 2.9. The best separation factor of $S_f = 3.9$ could be achieved for the highest beam energy of 88 MeV, which confirms the direct relation between the beam energy and the separation of different isotopes. The results are given in tab. 4.

3.7 New 5 Anode Gas Ionization Chamber

In the course of this thesis, a new compact 5 anode ionization chamber was developed, built and tested. The existing 2 anode ionization chamber, described by Hackenberg [66], has a total active length of only 54 mm and is therefore very compact. But on the other hand the detector is limited due to the inability to change between different anode combinations for an optimal separation and the comparatively high gas pressures required to stop the incoming beam within the active volume. Beside the 2 anode detector, there is the previously described 10 anode detector, see sec. 3.6. It has a total active length of 509 mm and a single 50 mm anode is nearly the size of the total active length of the 2 anode detector. Therefore, only very low gas pressures are required, as the test measurements revealed. The problem with such low detector gas pressures in combination with a long active detector volume is the larger mean free path of the incoming particles and therefore, the greater impact of angular straggling to the flight path.

For these reasons, a new multi anode ionization chamber was designed to fit between both existing detector designs. The new housing fits to almost every place of the beamline. In the following section the design, dimensions and specifications are explained at first, several measurements with the new detector are shown and the results are discussed.

3.7.1 Detector Design

The detector design was inspired by existing designs of Knie et al. [58] and Kurtz [67]. During the first phase of designing, it becomes clear that not only the size of the detector will be of great importance, but also a easy handling, a great amount of modifiability and the clear separation between the detector and its housing are required. The latter factor becomes crucial for a special position the new detector should be used at, right after the $120°$ bending magnet at the Tandetron™ accelerator, see fig. 5. At this point the distance between the exit of the magnetic field region and the entrance of the detector becomes minimal. The given space is limited to only 225 mm between the exit of the magnet vacuum chamber and the next gate valve to the often used 4 anode ionization chamber of HVE, which must be kept in position.

In order to meet all requirements, the new detector had to be compact and comparatively simple to remove from the beam line, to be able to use the 4 anode detector for the well established ^{10}Be measurements. Because of the limited space and the complex connection of beam tube parts to the vacuum chamber of the magnet, the new detector housing should be left in place, once it is installed, to reduce the required maintenance time. Therefore, the detector housing was built as a solid cuboid with a length of 215 mm, a width of 210 mm and a height of 169 mm including an entrance and exit port. The new housing replaces an existing beam tube and can be installed at almost any location along the beamline. This was done for several tests at the 10 MV Tandem accelerator and the 6 MV Tandetron™ accelerator, which are described in this section. In addition two feedthroughs at each side were integrated, to install a slit pair in the focal plane of the detector. The whole detector housing is shown in fig. 20.

The required detector entrance window is mounted in two steps to the inner front part of the detector. In a first step the entrance foil, which is already mounted to a frame, is fixed between two discs. In a second step, this unit is screwed to the detector housing from the inside. In this way, a entrance window can easily be replaced or removed if the housing is used as a simple beam tube. The used detector window is a 2 μm Mylar foil, which was later replaced by a 1000 nm SiN entrance foil with a size of 20×20 mm^2. To fulfill the second requirement, a fast and easy way to remove the detector itself, the cover plate of the housing was designed to hold the actual detector. To this end, four threaded rods are screwed to the top plate, which in turn contains all necessary feedthroughs. This includes six BNC connections for readout, two SHV for high voltage supplies and a DN16 flange as in- and outlet for the isobutane detector gas. The anode and the cathode are made of 1 mm thick stainless steel laser-cut from our in-house mechanics workshop. Both with a total length of 160 mm and a width of 100 mm, which lead to an active detector length of 150 mm. The Frisch-Grid is made of gold coated tungsten wire with a diameter of 15 μm, which is wrapped around a frame and hold by the serrated outer edge. The distance between each wire is 2 mm, see fig. 21c. The first designed anode plate is divided into five separate anodes, from which the first two anodes, each 25 mm long, are split diagonally. The next two anodes are 30 mm and the last one is 40 mm long. Each anode is interconnected by plastic bolds, which enables the very thin design and a very small spacing between each anode segment of only 0.8 mm, see fig. 21a. Based on the first results, given in sec. 3.7.2 and sec. 3.7.3, also a second anode design was built and used for the other measurements, shown in sec. 3.7.4. This design also consists of five anode segments, but the first one is relatively small, only 20 mm and not split. This was done, to reduce the capacity between the anode segment and the cathode. This, in turn, leads to a larger signal created at the corresponding segment for the same amount of created charge carrier, see Knoll et al. [65, p.140]. The second and third anode, both 30 mm long, are also split diagonal, see fig. 21b. The design of the last two anodes was left untouched. The anode segmentation and the angular resolution is investigated in detail in the Master Thesis of Gereon Hackenberg.
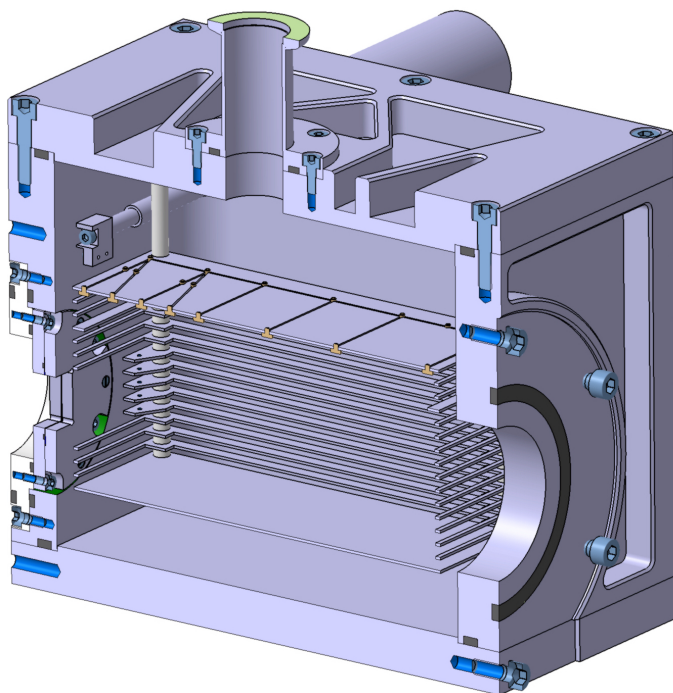
Figure 20: This technical drawing shows the housing of the new 5 anode ionization chamber, the entrance window in the left side, the anode (first design), the cathode, the Frisch-Grid as well as the left x-slit mount. The detector was cut in half, to provide a better overview. On both sides of the housing a additional feedthrough was integrated, to install a pair of slits. All required feedthroughs for the required isobutane gas as well as the electric conduction are integrated to the top plate.

The anode plate is mounted as the most upper layer of the detector. In this way the shortest possible connection between the feedthroughs and the anodes is achieved. The distance between the cover plate and the anode plate is defined to 49 mm by nonconductive spacers, which are slipped over the four threaded rods. The following layers are also separated by a non conduction, 5 mm piece of the same spacer material. To ensure the isolation between each plate and the mounting rods, a step was milled to each spacer that fits into the mounting hole.

In addition to the mentioned three main layers, anode, Frisch-Grid and cathode, the detector has 13 additional layers. Two of them between the anode and the Frisch-Grid and the remaining 11 between the Frisch-Grid and the cathode. All layers are interconnected via resistors to achieve a voltage divider. In this way the field boundary could be smoothed. A second advantage of this approach is, that only one power supply is required to run the detector. This minimizes errors at the charge collection and pre-amplification due to uncertainties and variations in different power supplies. In general a voltage of 500 V was used for the anodes and 250 V for the Frisch-Grid. The cathode is set to ground potential for all measurements.
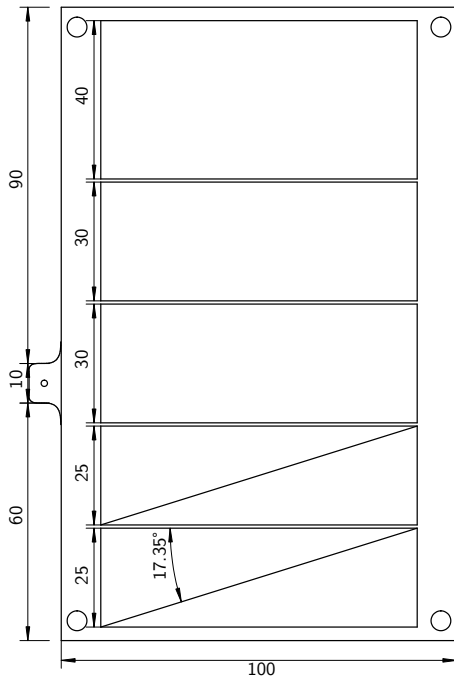
(a) Top view of the first design of the anode board. First two anodes are split diagonally.
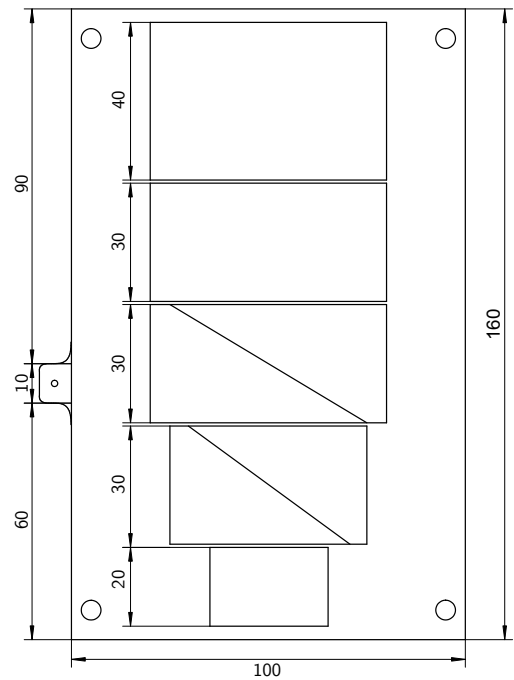
(b) Top view of the second design of the anode board.

(c) Frisch-Grid

Figure 21: The figure shows both designed, built and used anode configuration for the new 5 anode ionization chamber. Figure a) shows the first design, were the first two anodes are split and all anodes are of equal width. Figure b) shows the second design. In this case, the first anode is the smallest and not split, based on the findings from the first set of test measurement, see sec. 3.7.3. Figure c) shows the Frisch-Grid frame design.
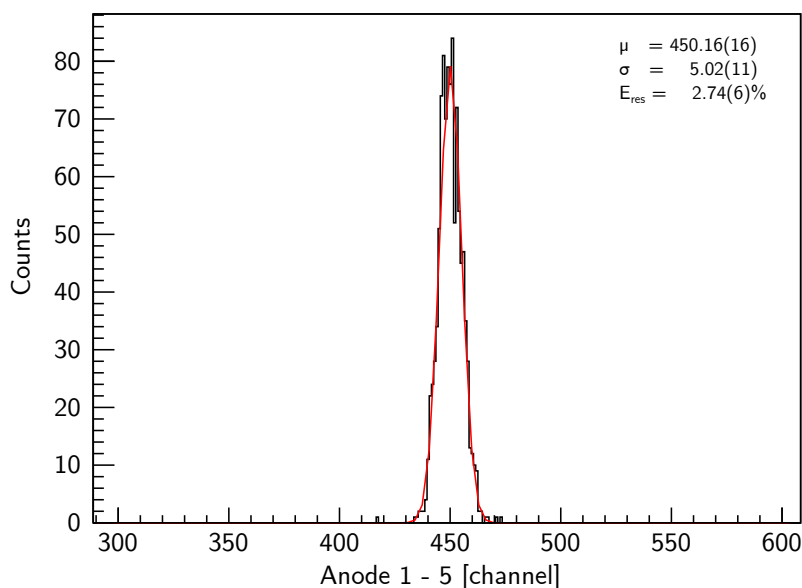
Figure 22: Measured total energy resolution E_{res} of the new designed 5 anode ionization chamber with the first anode design fig. 21a. Investigated with a $^{13}C^{5+}$ beam at 27.5 MeV beam energy, at an isobutane gas pressure of 80 mbar. The total energy resolution was determined to $E_{res} = 2.74(6)\%$

3.7.2 Determination of the Total Energy Resolution with ^{13}C

For a first test measurement, comparable to the measurements performed with the 10 anode ionization chamber described in sec. 3.6, the total energy resolution E_{res} was determined. The total energy resolution of a detector provides information about the ability to separate two different energies from each other. As discussed earlier in this thesis the separation of different $^{m}/_{q}$ interferences and isobars inside the ionization chamber is one of the main task of each AMS measurement, see sec. 2.2. To reduce the tuning effort required for other beam lines and therefore the source of errors, the new 5 anode ionization chamber was mounted to the right 15° port of the switching magnet of the 6 MV Tandetron™ accelerator, see fig. 5. The total energy resolution was determined by using, a $^{13}C^{5+}$ beam at 27.5 MeV beam energy. The procedure is described in sec. 3.6.2. Best results were achieved at 80 mbar isobutane gas and an anode voltage of 500 V. This measured spectrum was fitted and a total energy resolution of $E_{res} = 2.74(6)\%$ could be determined, see fig. 22. In this way also the correct conducting and functioning of all anodes was checked and the required anode voltage was determined.

3.7.3 Investigation of the Spatial Resolution of the Split Anodes

An early method to determine the spatial resolution was to install proportional counter between the anodes, described by Erskine et al. [68] and Shapira et al. [69]. Another method was to install an additional grid between the anode and the Frisch-Grid, the θ grid, described by Sann et al. [70]. Each wire of this grid was read out separately to determine the flight path. The downside of both option is a reduced energy resolution and a further limitation of the acceptable counting rate. A third option is to install a parallel plate avalanche counter in front of the ionization chamber, see Kusterer et al. [71], but in this way additional beam scattering is induced which
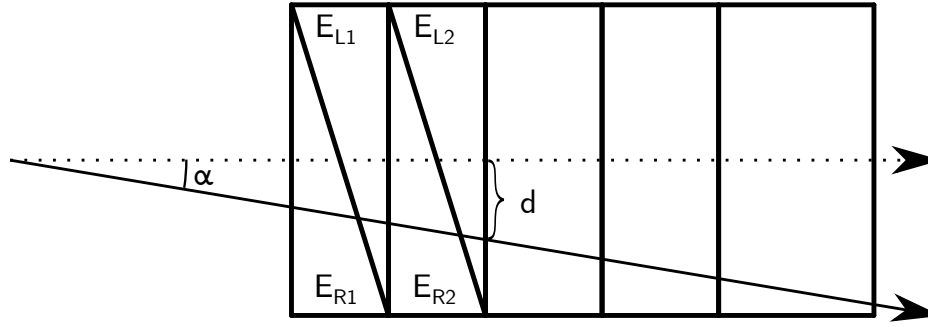
Figure 23: Concept of the split anodes, taking the example of the first anode design. The black line represents the flight path of the incoming beam, inclined by the angle α and the optical axis is given by the dotted line. The split anodes are separated to E_{R1}, E_{L1} as well as E_{R2}, E_{L2}. If the path of an incoming particle is inclined to the right side, the traversed distance of each right anode is larger than the traversed segment of the left anode, and therefore the amount of deposited energy.

leads to a decrease in separation and energy resolution. As described in the previous section, the new detector is equipped with two pairs of split anodes. The idea of a split anode is to measure not only the amount of deposit energy, but provide also information concerning the flightpath and therefore the angle of the incoming particle. This idea was first described and realized by Rosner et al. [72]. By using a split anode design, the position information for the dispersive axis is obtained by comparing the signals of the left and the right part of one split anode. If a particle enters the detector on the central axis, the covered distances on the left triangular part and on the right triangular part of the anode are equal and therefore the amount of energy deposited to each side. But, if the trajectory of the incoming particle is inclined by an angle α, the covered distances on the left and right anode segment differ from each other, see fig. 23. The deviation from the central axis d can be described by the following formula, see Rosner et al. [72].

$$d = \frac{E_R - E_L}{E_R + E_L}$$

To investigate the spatial resolution, two separate 1 mm wide slit pairs were installed on the way to the detector. The first one was mounted 545 mm in front of the entrance window and the second one 5 mm after the entrance window, see fig. 53. In this way the incoming beam is well defined in size and position. To simulate different angles the x-slit inside the detector was moved in steps of ± 1 mm perpendicular the optical axis. For this measurement the first anode design was used, since the second was developed afterwards, descried later in this section. This results is a deviation of the entrance angle of $\alpha = 0.103°/\text{mm}$. For each step and each of the four split anode segments, the position of the detected peak in the spectrum was determined hereinafter, see fig. 24. To describe the changes in energy deposition, the 0 mm shifted position at the center of the detector was set as a reference point and all other measured positions are given in relative terms as a relative energy loss E_{rel}.

$$E_{rel} = \frac{E_{loss}(x)}{E_{loss}(0)}$$

Where $E_{loss}(x)$ represents the energy loss at a specific distance x in mm from the optical axis and $E_{loss}(0)$ the energy loss measured along the optical axis. Furthermore, for each measured angle the length of the flight path along the corresponding anode segment was calculated. Therefore, the
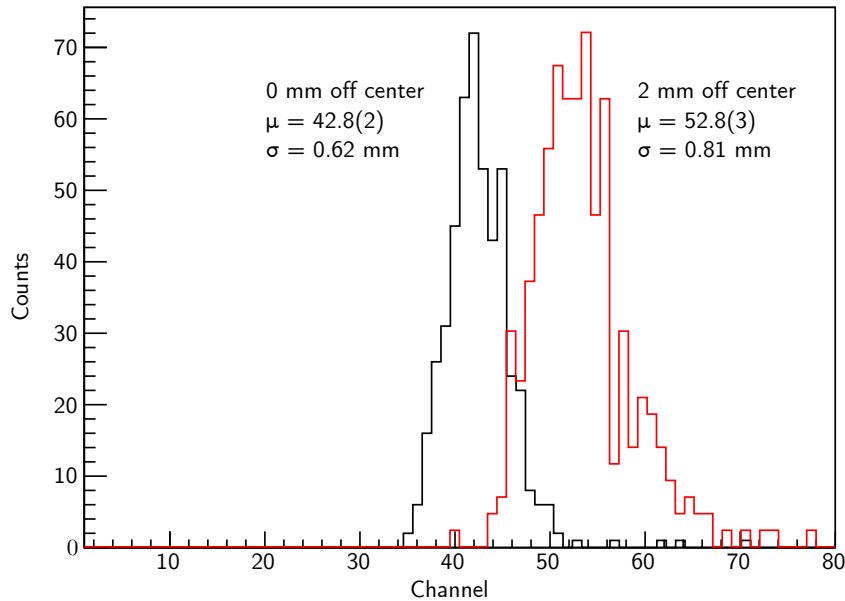
Figure 24: The figure shows the measured distribution of a ^{13}C beam at the first anode segment E_{R1} of the new 5 anode ionization chamber detected with the first anode design. The black line indicates a beam at the center axis. The red line shows the same beam shifted by 2 mm, by using x-slit pairs. The center of both peaks is determined by a Gaussian fit and the fit values displayed next to the corresponding distribution. Based on the known distances inside the detector and the given geometry, the σ can be calculated in units of mm.

reference energy of 1 is achieved at a flight path of 12.5 mm which corresponds to the half anode length. In fig. 25 these relative energy differences are plotted against the flight path, marked by crosses, for anode 1 and 2 individually.

In a second step, a SRIM simulation was done for ^{13}C at 27.5 MeV beam energy, to determine the theoretical energy loss along the first two anodes of the detector. The result of this simulations are also shown in fig. 25, marked by a line in the corresponding color. All simulations fit well to the data, except anode 1R which reveals a great discrepancy. Originating from the reference point, the relative energy loss for longer and shorter flight path should be symmetric around 1, as the overall energy loss must remain constant. This discrepancy can be explained by a shorter effective length of anode segment 1R. If the effective length is shortened by 9 mm the SRIM simulation fits much better to the measured data. The result is given in fig. 25a marked by the dotted line. A reason for the shortening of the effective anode length can be found in the shape of the electric field between the anode and the cathode. Due to the compact form of the detector, field inhomogeneities can occur, which reduce the amount of collectible charges and therefore the detected energy deposition. This corresponds to an energy loss of 0.2 MeV$\sim$ 0.7% of the total energy, which could not be detected. As a first consequence, a second anode plate was designed which is shown in fig. 21b. In this case, the first anode is no longer split and is shortened by 5 mm. Furthermore, the width of the anode is reduced by half to reduce the capacity and enable a higher output signal while the amount of collected charge carrier stays constant. In general the split anodes can help to reduce the isobaric background during an AMS measurement, for example after a gas-filled magnet.

(a) Anode 1   **(b)** Anode 2
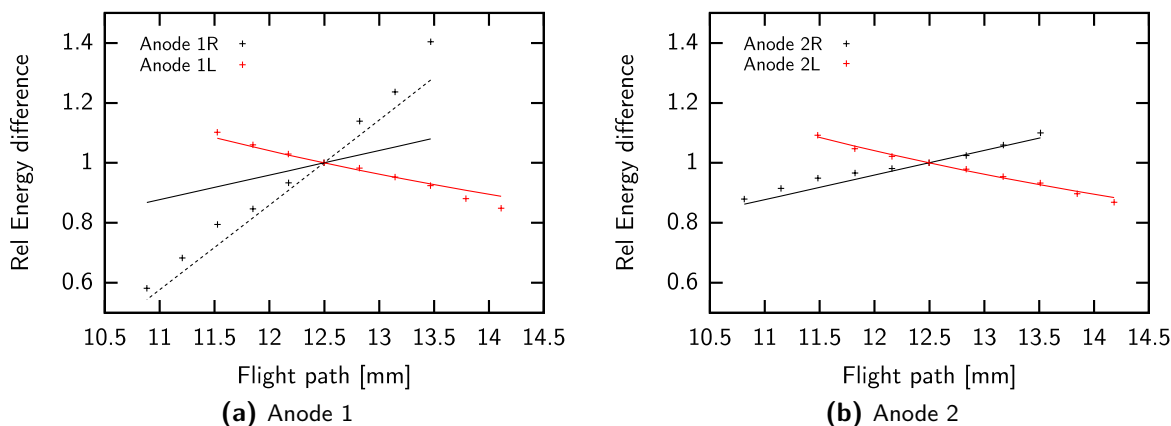
Figure 25: Both figures show the relative energy loss of the ^{13}C particles along their flightpath through the detector. Figure a) represents the losses on anode 1 and figure b) the losses on anode 2. All measured values are indicated by the crosses and the SRIM simulations are indicated by the line with the corresponding color. Except from anode segment 1R in figure a) all simulations fit very well to measured values. By reducing the effective flight path along this anode segment in the simulation by 9 mm, the dotted black line in figure a) was calculated.

3.7.4 AMS Measurements with ^{10}Be at the 6 MV Tandetron™ Accelerator

Origin and Applications of ^{10}Be

The production of ^{10}Be is mainly based on three different mechanisms. First of all the spallation reaction, where high energetic cosmic neutrons collide with atomic nuclei and sputter protons, neutrons or even heavier nuclei, for example ^{16}O(n,^{3}He α)^{10}Be or ^{28}Si(n,x)^{10}Be. Another way of producing ^{10}Be is by capturing negative muons from the incoming cosmic rays. This procedure is also observed for oxygen, ^{16}O(μ^-, α p n)^{10}Be, and for silicon, ^{28}Si(μ^-, x)^{10}Be. The last mechanism is based on the capture of thermal neutrons. It follows the ^{9}Be(n, γ)^{10}Be reaction path and is of great interest for astrophysical considerations. A detailed description is given by Dunai [73].

The produced ^{10}Be has a half-life of $1.36(7) \times 10^{-6}$ a, see Korschinek et al. [74], and is mainly used to investigate changes in geological environments. For in situ produced ^{10}Be two main applications can be distinguished. On the one hand the exposure dating and on the other hand the burial dating. With exposure dating land forming processes as well as erosional features can be investigated. For non eroding surfaced this is done by measuring the amount of the produced radionuclide. If erosion or shielding takes place this has to be taken into account and the calculated age has to be corrected, see Granger et al. [75].

Measurements with ^{10}Be are used also to supervise and reconstruct climatic changes. Atmospheric ^{10}Be is washed out by rain and snow and deposited into polar ice cores. These cores are investigated layer by layer to reconstruct changes in climate, variations in the solar activity or volcanic activities, see Baroni et al. [76].

Another field of application for AMS measurements with ^{10}Be is the investigation of nuclear synthesis during r-processes. For that purpose, ^{9}Be samples are irradiated with a spectrum of neutrons similar to the cosmic energy conditions. The resulting ^{10}Be can be measured with AMS methods to investigate production rates and cross section, see Wallner et al. [77].

AMS Measurement of ^{10}Be

For the final test of the new 5 anode ionization chamber a AMS measurement was conducted with a ^{10}Be^{2+} beam. To verify the acquired data and compare the results to the well known 4 anode ionization chamber from HVE. The detector was mounted right after the 120° bending magnet, at the 6 MV Tandetron™ accelerator. At this position the detector is only 550 mm in front of the often used 4 anode ionization chamber, measured between both entrance windows, see fig. 5. Therefore, very similar settings can be used for both measurements, which reduces the number of error sources and allows maximum comparability. For this measurement, the new designed anode plate was used, see fig. 21b. The settings used for the following ^{10}Be AMS measurements were determined and optimized by Dr. Stefan Heinze during the last years of standard operation, they are given in tab. 23 in the appendix. Based on this well known and often confirmed settings, the new designed ionization chamber was tested. At the end of a ^{10}Be beam time, the new 5 anode ionization chamber was installed. The procedure includes, installing the entrance window as well as injecting the isobutane gas and the connection of the new setup to

(a) ^{10}Be standard ICN 01-5-1 (2.709×10^{-11})

(b) ^{10}Be standard ICN 01-5-3 (6.320×10^{-12})

(c) ^{10}Be standard ICN 01-6-2 (5.349×10^{-13})
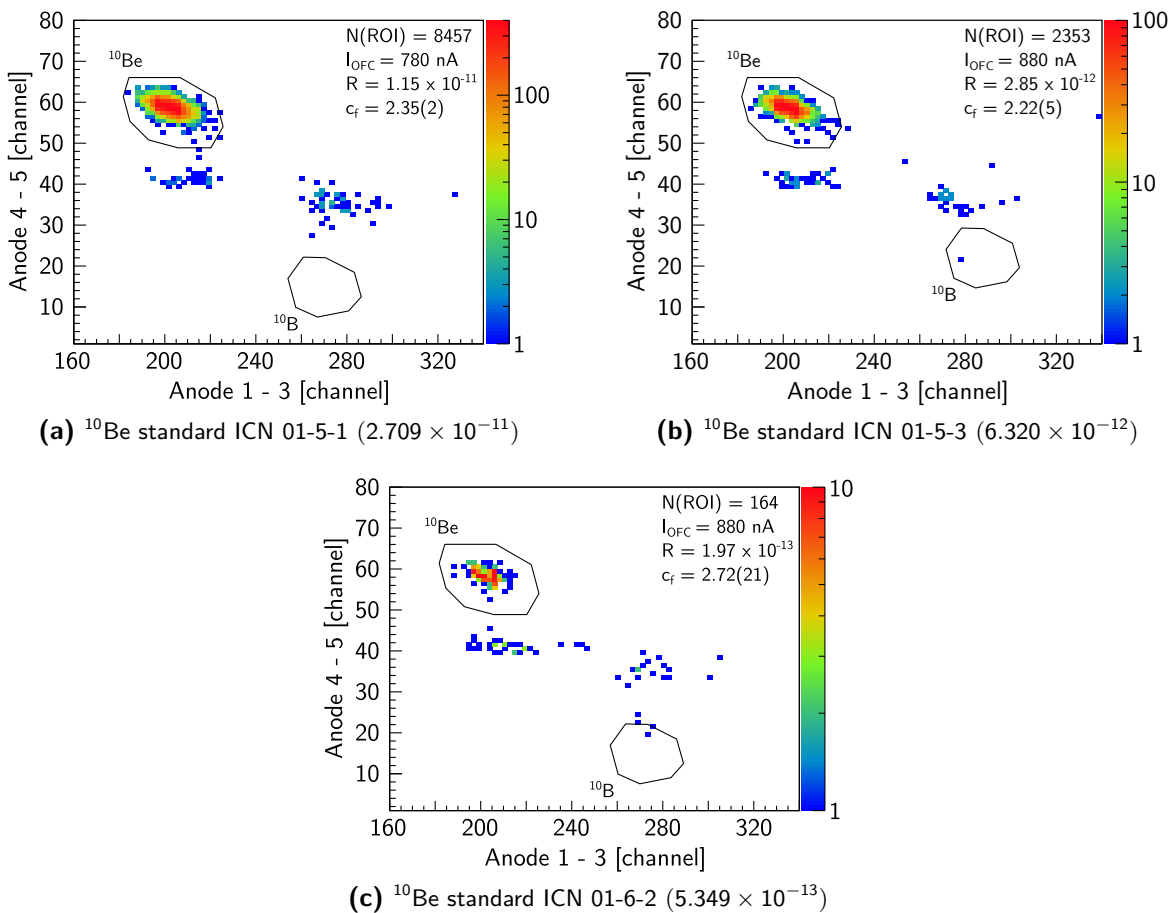
Figure 26: Measurements at the AMS with a ^{10}Be beam to test the new 5-Anode ionization chamber with verified system settings. The measured standard samples are ICN 01-5-1 (^{10}Be/Be $= 2.709 \times 10^{-11}$) , ICN 01-5-3 (^{10}Be/Be $= 6.320 \times 10^{-12}$) and ICN 01-6-2 (^{10}Be/Be $= 5.349 \times 10^{-13}$), see Nishiizumi [78]. The measured ^{10}Be counts N(ROI), ^{10}Be/Be ratios R, Offset Faraday cup (OFC) currents I$_{OFC}$ as well as the resulting correction factor c$_f$ are given in the corresponding figure keys.

(a) ^{10}Be standard ICN 01-5-1. Including all anode signals, without further coincidence condition.

(b) Projection to the total energy diagonal line
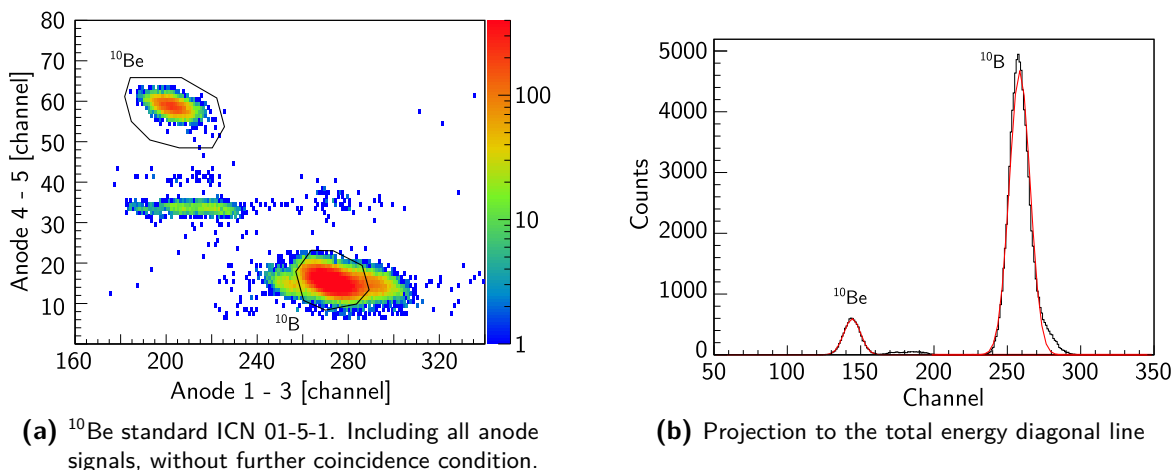
Figure 27: Figure a) shows the spectrum of fig. 26a, but without any coincidence condition for the last anode. In this way the ^{10}B component becomes visible and the determination of the separation factor is possible. Figure b) shows the projection of the peak intensities to the total energy diagonal. In this way the spectrum is projected to a 1-dim spectrum and the separation factor was determined to $S_f = 2.98$, as described in sec. 2.2.2.

the data acquisition system. After that, the beam time was continued with the new detector and already measured standard samples were measured with the new detector. For the following measurements, a ^{10}Be^{2+} beam at an energy of 13.53 MeV was chosen. Several combinations of anode and Frisch-Grid voltages as well as different isobutane gas pressures were tested. Best results were achieved with an isobutane gas pressure of 43.5 mbar and an anode voltage of 500 V. The used standard samples for this measurement are ICN 01-5-1 (^{10}Be/Be $= 2.709 \times 10^{-11}$), ICN 01-5-3 (^{10}Be/Be $= 6.320 \times 10^{-12}$) and ICN 01-6-2 (^{10}Be/Be $= 5.349 \times 10^{-13}$), see Nishiizumi [78]. By using standard samples of different orders of magnitude, it is possible to determine the ratio between ^{10}Be and the stable ^{9}Be as well as to compare the resulting correction factors c_f. The results are given in tab. 5. The corresponding 2-dim histograms are given in fig. 26. The determined ratios R of each measured sample fits well to the expected values.

Another aspect for most AMS measurements is the separation factor S_f between the isotope and its isobar. In case of ^{10}Be the corresponding isobar is ^{10}B, with a $\Delta Z/Z = 4$. Based on the very low nuclear charge Z, the differences in energy loss in matter between ^{10}Be and ^{10}B are much higher, than the differences for ^{41}Ca and ^{41}K, for example. This means, that by choosing the right detector gas pressure, the majority of the isobaric background can be stopped at the second last anode and will therefore not be counted in any spectrum containing the last anodes signals. Nevertheless, the detected information is still recorded to the listmode files, if acquired and can therefore be investigated by offline analysis with ROOT, see sec. 4.3. In this way, a spectrum can be generated including all signals, whether or not they are detected on the last anode. The resulting plot is given in fig. 27a. By projecting the peak intensities to the total energy diagonal line, the histogram can be reduced to a 1-dim spectrum and fitted by two Gaussian distributions. The result is given in fig. 27b. Based on the fit, the separation factor is determined to $S_f = 2.98$.

In a last step the results obtained from measurements with the new 5 anode ionization chamber are compared to the results measured with the existing 4 anode ionization chamber of HVE. In both cases, the same standard samples are compared. The corresponding values are displayed in tab. 5. The determined ratios as well as the determined correction factors match each other within the 2σ error limits. Only the lowest measured standard sample ICN 01-6-2, with a given

Table 5: Results from the first AMS measurement at the 6 MV Tandetron™ accelerator using the new 5 anode ionization chamber, in comparison to results measured with the existing and routinely used 4 anode ionization chamber. The determined ratios as well as the determined correction factors match each other within the 2σ error limits. The sample ICN 01-5-1 was not measured during former runs, and is therefore only given for comparing the correction factor.

Det.	Standard Sample	$N(^{10}Be)$	$\bar{I}(Be)$ [nA]	$R(^{10}Be/Be)$	c_f
New	ICN 01-5-1 (2.709×10^{-11})	8457(92)	650	$1.13(1) \times 10^{-11}$	2.35(2)
	ICN 01-5-3 (6.320×10^{-12})	2353(48)	880	$2.85(6) \times 10^{-12}$	2.22(5)
	ICN 01-6-2 (5.349×10^{-13})	164(13)	880	$1.97(15) \times 10^{-13}$	2.72(21)
HVE	ICN 01-5-3 (6.320×10^{-12})	2162(46)	932	$2.70(6) \times 10^{-12}$	2.34(5)
	ICN 01-6-2 (5.349×10^{-13})	294(17)	1515	$2.26(13) \times 10^{-13}$	2.36(14)

ratio of $R_{lit.}(^{10}Be/Be) = 5.349 \times 10^{-13}$, provided an elevated correction factor, which could be caused by used up sample and instable beam.

3.8 Results of the Developments and the Test Measurements

A major improvement was the commissioning of the new 135° gas-filled magnet at the 10 MV Tandem accelerator. This includes the installation of three new power supplies and their integration to the existing LabVIEW™ based control software via Ethernet. In this way a full 16-bit connection was established. An identical power supply was installed at the 90° magnet of the low energy mass spectrometer, whereby the existing 11-bit control was replaced by the 16-bit control. This enables a by one order of magnitude higher precision of the current applied to the magnet. Furthermore, two NMR probes were mounted to radial ports of the 135° magnet, at the top of two movable rods. In this way, the homogeneity of the magnetic field was measured to $B_{hom} < 1.64 \times 10^{-4}$ in a range of ± 50 mm from the optical axis, which confirms the specifications of the manufacturer of $B_{hom} = 4 \times 10^{-4}$ in the same region. To enable a gas-filled mode, a gas handling system was designed and installed to the vacuum chamber of the magnet. The system is able to evacuate, ventilate and control the injected gas pressure of the vacuum chamber as well as the ionization chamber mounted downstream, individually and with a high reproducibility.

Another task investigated was the recommissioning of an ionization chamber obtained from the University of Utrecht. The detector is equipped with ten anodes and has an active detector length of 509 mm. According to the used MPA3 data acquisition system, only eight anodes signals could be detected simultaneously. A $^{12}C^{5+}$ beam was used for testing the functionality of the anodes, the Frisch-Grid and the used data acquisition system in principal and to determine the total energy resolution. The measurements with $^{40}Ca^{7+}$, $^{39}K^{7+}$ and $^{48}Ti^{7+}$ as well as $^{58}Fe^{9+}$, $^{58}Fe^{10+}$ and $^{58}Ni^{9+}$, $^{58}Ni^{10+}$ gave a first assessment concerning the feasibility of AMS measurements with the intended ^{41}Ca and ^{60}Fe isotopes in combination with this ionization chamber. Key aspects for later measurements were investigated, like the beam energy, suitable isobutane gas pressures, energy resolutions and separation factors. The determined energy resolutions are good and comparable to the resolutions achieved with other ionization chambers, see sec. 3.7.2. Furthermore, the energy loss for each anode was measured and compared to the simulations done with SRIM. Hereinafter three possible reasons for the 6 mbar discrepancy, between the measured

and the simulated pressure, are given. On the one hand the used gas pressure probe, although based on an absolute measurement method, is sensitive to the mounting orientation. On the other hand, the composition of the used isobutane gas can lead to different pressures required for the same measurement results. The third reason could be an inhomogeneous electric field inside the ionization chamber. In this way the charge collection is distorted. Based on the measured energy losses, also the separation between ^{40}Ca and ^{39}K as well as the separation between ^{58}Fe and ^{58}Ni was determined. In this context, the importance of the right combining of anode signals and the correct data handling became clear. More detailed information concerning the data handling and offline data analysis is given in sec. 4.1. According to the limitation of simultaneously detectable anode signals, the uncertainties in required gas pressures and the large active detector length in combination with the available beam energies, the 10 anode ionization chamber seems to be inappropriate for the intended measurements.

During the investigation concerning ^{58}Fe and ^{58}Ni at different beam energies, the importance of the right and preferably thin entrance foil was revealed. The energy loss difference of 100 MeV ^{58}Fe in 200 nm SiN in comparison to 2 µm Mylar foil is 10 MeV, and therefore remarkable high. Since the gain of energy is crucial for all upcoming measurements the former entrance foil was replaced by a 200 nm SiN window.

In parallel to the performance tests and measurements with the 10 anode ionization chamber, a new 5 anode ionization chamber was designed and built as a compact and easy to handle detector setup. The new type of housing makes it extremely versatile and allows to install the detector at almost any position along the beamline. For this purpose, actually two different housings are available and a third is at the planing stage, to install them at frequently used positions. The detector itself is, due to the simple layer-by-layer structure, also modular and can be adapted to any upcoming requirements.

To test the proper functioning of the new setup, several test measurements and also AMS measurement with ^{10}Be were performed. As a first test, the total energy resolution E_{res} was investigated by measuring the energy deposition of a ^{13}C beam over the total active detector volume. The achieved value is $E_{res} = 2.74(6)\%$. In a next step also split anodes were tested by varying the ion beam entrance angle to the detector. The AMS measurement with ^{10}Be^{2+} at a beam energy of 13.53 MeV was performed at the 6 MV Tandetron™ accelerator. The resulting isotopic ratios and corresponding correction factors are in good accordance with the measurements performed at the well established 4 anode ionization chamber. For both measurements the same standard samples were used. The weighted mean correction factors, on the one hand determined by the new detector is $c_f = 2.43(21)$ and on the other hand determined with the existing setup $c_f = 2.35(14)$, match each other within the error limits.

Chapter 4

AMS Data Acquisition and Processing

In this chapter the data acquisition and handling during AMS measurements will be described with regard to the used hardware and software at the 6 MV Tandetron™ accelerator as well as at the 10 MV Tandem accelerator. The data acquisition at both accelerators is done with a similar MPA3 ADC system from FAST ComTec. The system can handle between 4 and 16 ADC channels, is able to resolve coincidence times of multiple signals between 150 ns and 3 ms and can add the timing information from a 48-bit RealTimeClock, see [79]. The Tandetron™ accelerator provides a permanently installed version of the system with 4 ADC channels. For the 10 MV Tandem accelerator a system with 8 ADC ports was installed to a movable rack system, see Müller-Gatermann [56]. The benefits from the permanently installed system are the interconnection between the data acquisition and the control system of the accelerator itself. In that way, it is possible to optimize the beam tuning with respect to the detector counts in an efficient way. The larger system, used at the Tandem accelerator, on the other hand is much more flexible and can be used dynamically at different setups. Furthermore, it provides twice the number of ADC channels.

4.1 AMS Data Acquisition

After tuning the beam for an AMS measurement, as it is described later in this thesis, also the detector system and data acquisition have to be configured. Based on the isobutane gas pressure chosen for the detector and the number of anodes available, the spectra to be recorded can be set. Since the principle for AMS measurements is based on the detection of single ions by their energy loss in matter depending on their nuclear charge Z, the correct combination of available detector signals is crucial for the best results, compare fig. 16 and fig. 18. To this end, the range of ions in matter should be predicted with a suitable software, like SRIM. In that way, a good separation between the desired radionuclide and the isobar can be achieved. In the case of nuclides without existing isobar, at least at the detector, a correct gas pressure is still important for a optimal energy deposition inside the active detector volume and to separate possible m/q interferences.

For this purpose, the MPA3 software provides the signals from each anode individually and several possibilities to combine different signals into one diagram (1-dim) or histogram (2-dim). The range of the implemented 16-bit ADC can be preset from 256 to 65536 channels, per ADC input channel. The most used function is the sum of two spectra. In this case the signals of two anodes are combined into one spectrum with a preset range, on the condition that the incoming signals were coincident. Two signals are accepted as coincident if the time span between the detection is less than the preset condition, which is usually about 20 µs. The preset for the ranges of a single ADC spectrum of 1024 channels turned out to be a good compromise between software performance and achieved resolution. For a full overview of the possible combinations of the spectra and presetting possibilities of the MPA3 software see [79].

The second important pre-measurement configuration is the 2-dim histogram plot. To this end, two 1-dim spectra can be set to the axes of the 2-dim histogram. Only if these histogram plots, so called maps, are configured correctly, conclusions can be drawn concerning peak position and shape as well as the allocation of a measured peak to a expected beam component. Furthermore, the so called region of interest (ROI) has to be defined within the 2-dim histogram. All events inside this region are counted separately. In general ROI's are used to count the amount of the intended isotope or the measured isobar. Based on this value N(R), all isotopic ratios are calculated, see sec. 2.2.1.

In general the recorded data from a single measurement with the MPA3 software is stored, into a `mpa` file, after the measurement is stopped. The data can be stored in ASCII, binary, GANAAS or csv format, whereby ASCII is the most common and easiest to handle. The `mpa` file includes a header, with all settings and preset parameters, followed by the data of each spectrum. First of all the single spectra from each recorded ADC channel are listed. Each starts with a initial line `[DATA<id>,<Range>]`, where the id represents the ADC channel number and range the amount of channels recorded in this spectrum, followed by a short header with information about the name, the given titles and another line `[DATA]`. After this line the recorded data is given as a list, sorted by the channels number, followed by the number of detected counts. Also the calculated spectra are given in the same way. The corresponding header line is `[CDAT<num>,<Range>]`, where `num` represents just an increasing integer number, which starts at zero. The calculated spectra include all pre-configured sum spectra (or similar, see [79]) as well as the 2-dim histograms. In the case of the 2-dim histograms two different data structures are possible depending on the software settings. The corresponding option is `Drop 'Zero events'` and can be chosen at the `Data Operation` dialog box of the MPA3 software. If the option is untagged also channels with zero counts were written to the file. The resulting data formate is a single integer number per row, which contains the number of counts for one point at the 2-dim histogram. In the case of a 1024×1024 channel spectrum $1\,048\,576$ lines were written. On the other hand, if the option is tagged, only non zero channels from the spectrum were stored to the mpa file. In this case the data structures changes from one to three integer values per line and contains the number of events, the channel number on the x-axis and the channel number on the y-axis, respectively. Of course, the stored data itself stays unaffected by the structure.

One disadvantage resulting from the fact that only the detected events for all ADC's as well as the predefined spectra are stored into the `mpa` file is the loss of any timing information for single events. Therefore, it is not possible to construct histograms from the ADC spectra during offline analysis, due to the missing coincidence information of single events. In order to retain the possibility, it is necessary to activate another option at the `Data Operation` dialog box, called `Write Listfile`. A listfile will than be stored under the same name and into the same folder as the corresponding `mpa` file, but with the file extension `lst`. It should be noted, the in contrast to the `mpa` files, a `lst` file is written continuously during the measurement and not in the end. Therefore, it is very important to safe the `mpa` file with a new file name or at a different location before starting a new measurement, to not overwrite existing data stored from the last measurement in the listfile. The list mode data is stored as a binary file to enable a higher information density in comparison to the plain ASCII files. For this reason, the file is not that easy to handle and has be converted into a more usable structure. To this end, a set of existing C++ tools written in-house by Dr. Nigel Warr were used to convert the list mode data into so called ROOT-Trees. Such a tree can contain branches. These in turn, contain so called leafs. For each anode signal detected during a measurement, such a leaf is created and contains all events and timing information. For detailed information about the ROOT framework see [80] or

the full manual available at the CERN documentation servers.[3] In the course of this thesis, and in collaboration with Mario Cappellazzo, the existing C++ tool was modified to comply with the requirements of an AMS measurement. Now a single C++ script, stored at the Institutes server, is sufficient to translate a raw list mode file into a ROOT file. It is further possible to combine multiple list mode files into one ROOT-Tree.

4.2 MPA Data Analysis

Each AMS measurement of isotopic ratios performed at either the 10 MV Tandem accelerator or the 6 MV Tandetron™ accelerator produces several mpa files. Depending on the number of measurements and the required amount of tuning runs. A single day measurement at the Tandetron™ accelerator results, for example, in about 237 individual mpa files. Therefore, the handling and analysis of mpa files is of great importance. For this purpose, several useful Python tools were developed as part of this work. The main task of the scripts is to convert the recorded 2-dim histogram data into a simple three column format, consisting of the coordinates x and y and the corresponding number of counts stored in ASCII format. In this way measured spectra can easily be plotted without loading them to the MPA3 software again. As described in sec. 4.1, the required procedure depends on the settings the data were recorded with. For both cases, with and without Zero events recorded, a tool was developed and given in code block B.3 and code block B.4, respectively. Both codes extract the data of a certain 2-dim spectrum and stores it into a new file. This provides the possibility for a fast look into the data and a comparison between different runs, settings and samples, but it also opens the field of offline analysis, which was done in the following section.

4.3 List Mode Data Analysis with ROOT

In comparison with the possibilities provided by analyzing the mpa files, the offline analysis based on list mode files is much more powerful but also more complex and time consuming. Therefore, it is always a good approach to start with the mpa analysis to get a first overview of the data. After converting the list mode data to ROOT files, see sec. B, it is possible to plot each single spectrum directly and each possible combination in 1-dim and also as 2-dim histograms. In addition new conditions and coincidences for the summation and subtraction of events can be set. As a consequence it is possible to take various aspects into account, like the influence of a specific detector anode to a measured peak or the changes in transmission, if the ROI would be set in a different way. All conditions can be concatenated and the resulting spectra displayed, including ROI's and the number of counts inside and outside the selected region. In this way the background generated by a isobar may be reduced.

As an example for the resulting possibilities of a offline analysis with ROOT, a test measurement with stable ^{40}Ca and ^{39}K beams performed at the 10 MV Tandem accelerator is shown in fig. 28. The measurements were done after another, for ^{40}Ca and ^{39}K separately. For this measurement the 10 anode ionization chamber was used, from which five anodes were read out. On the x-axis the counts from anodes 1 to 3 where plotted against the counts from anodes 4 to 5 on the y-axis. In fig. 28a and fig. 28c the raw data of the individual measurement for ^{39}K and ^{40}Ca are shown. The figures fig. 28b and fig. 28d show the results of a software cut. In total six ROI's were defined based on different anode combination (1 against 2, 1 against 3, 1 against 5, 2 against 5, 3 against

[3] Full manual of ROOT, Retrieved February 21,2019 https://root.cern.ch

(a) Measurement of stable ^{39}K

(b) Measurement of stable ^{39}K including applied ROOT cuts

(c) Measurement of stable ^{40}Ca

(d) Measurement of stable ^{40}Ca including applied ROOT cuts
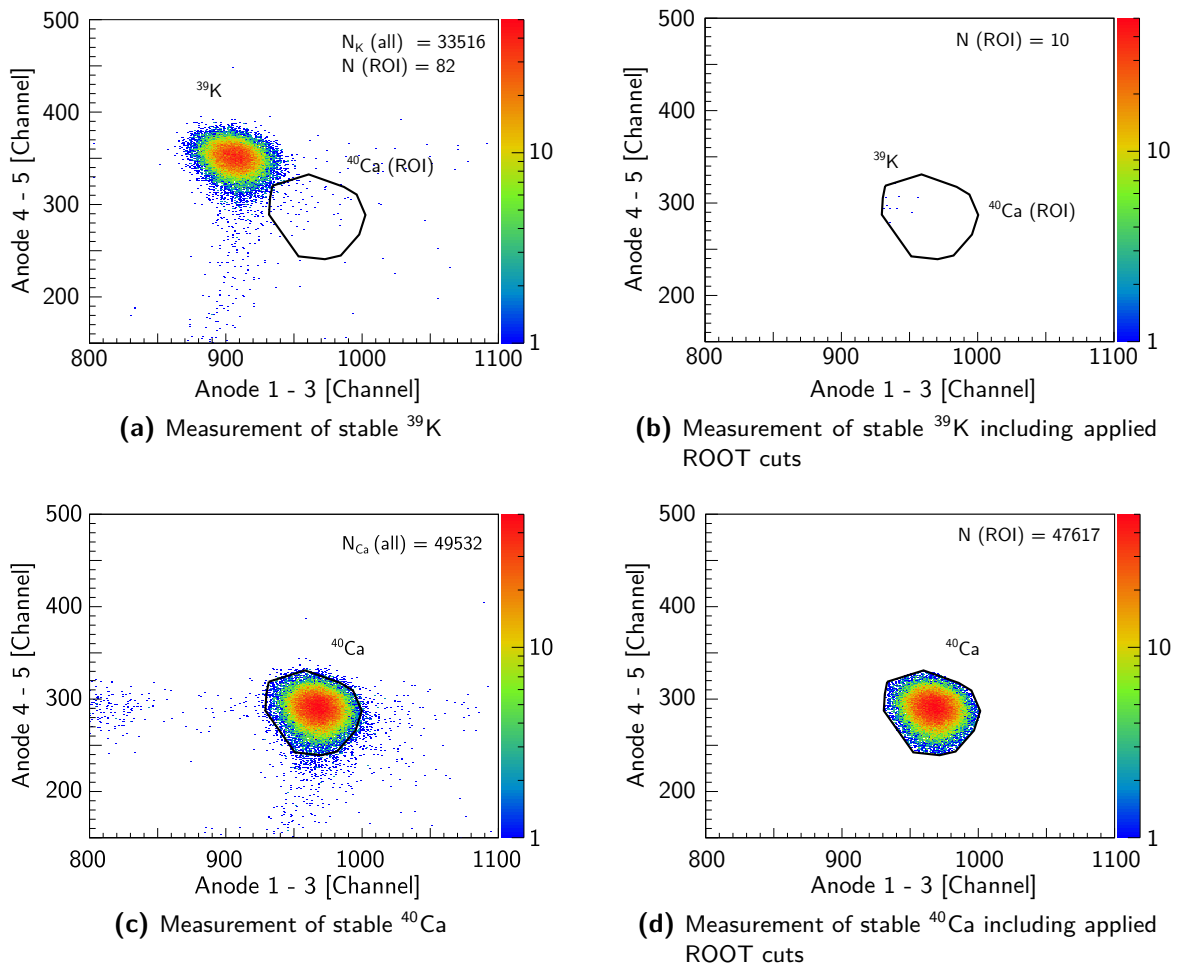
Figure 28: The plots show separate measurements for K and Ca performed at the 10 MV Tandem accelerator with the first 5 anodes of the 10 anode ionization chamber, in which stable beams were used for test purpose, see the test measurements sec. 3.6.2. In figure a) and c) the measurements with stable ^{39}K and ^{40}Ca are shown, respectively. The plots on the right hand side, b) and d), show both spectra after several software cuts are applied with ROOT. In this way it is possible to reduce the amount of ^{39}K counted inside the ^{40}Ca ROI from 82 to 10, but keep 97% of the intended ^{40}Ca counts.

5, 1-3 against 4-5). Further conditions had no positive effect. Based on this cuts the number of ^{39}K counts inside the ^{40}Ca ROI could be reduced from 82 to 10. This resulted in a false counting rate of 1 ^{39}K in about 4763 ^{40}Ca counts. A second example for the use of list mode files is given in chapter 6.3.3. During the analysis of the results from several ^{41}Ca measurements, the question has been raised if the background according to the potassium contamination could be corrected. Since no ROI was set to the spectra during measurement this would not be possible with the mpa files. But by using the list mode data in combination with the ROOT framework, it was possible to set a ROI, apply it to each recorded spectrum, read the counts inside and print the result into a single file. These investigations indicates the possibilities of list mode data in combination with the ROOT data analysis framework. But, on the other hand, it had to be mentioned, that the process of finding suitable cuts and conditions can take several hours for each list mode measurement. It thus is advisable to do this kind of offline analysis after a set of

test measurements and apply the resulting conditions directly to the MPA3 software for all later measurements.

4.4 Batch Mode Analysis

The batch mode analysis is specially required for routine measurements a the 6 MV Tandetron™ accelerator. As explained in sec. 3.2, each sample is measured several times to compensate possible system fluctuation. Beside the `mpa` and `lst` file, an analysis file is generated for each run by the HVE software, with the file extension `fsires`. Each file contains information about the sample ID, presettings, run time and live time of the detector, the number of counts inside chosen ROI, stable beam currents and isotopic ratios. In the case of the ^{41}Ca measurement, which is described in detail in chapter 6, this leads to a total sum of 2308 individual files related to 170 samples.

To analyze measurement aspects like beam stability, sample lifetime, stable beam current, total counts and counting statistics, it is therefore necessary to look at all `fsires` files of each individual sample. The task was simplify by a python tool written in the course of this thesis, see code block B.2, which extracts all relevant informations of all `fsires` files into a single output file. The file contains the information in ASCII format line-by-line sorted by the run number. In this way it can easily be imported to any common spreadsheet program. For each sample, the corresponding statistical error and deviations were calculated in the same way. Several aspects, concerning data reduction and analysis can be found in Tuniz et al. [81]. A complete description of the used procedure is given by Wacker et al. [82]. To calculate mean values over several runs the measured quantities should be weighted by the measured beam current of the corresponding stable isobar. The weight w can be defined as the measured current multiplied with the corresponding detector live time. The individual error ΔR is dominated by the counting statistics.

$$w_i = \overline{I}_i \cdot t_i$$

Where $\overline{I}_i$ is the detected mean current during a singe run i and t_i the corresponding time of the run. Based on this weight, the weighted mean ratio $\overline{R}$ and the corresponding error can be calculated.

$$\overline{R} = \sum_i \frac{(R_i \cdot w_i)}{\sum_i w_i} \tag{4.1}$$

$$\Delta\overline{R} = \frac{1}{\sum_i w_i} \sqrt{\sum_i (w_i \, \Delta R)^2}$$

Chapter 5

Measurements with ^{58}Fe at the 10 MV Tandem Accelerator

The first AMS measurements at the new dedicated AMS beam line at the 10 MV Tandem accelerator were performed with ^{53}Mn by Schiffer [3]. Within the scope of this thesis, the new 135° gas-filled magnet was installed and set into operation as described in sec. 3.5. For upcoming measurements of ^{60}Fe, this beamline in combination with a new 135° gas-filled magnet is well suited. The corresponding isobar ^{60}Ni is easier to separate due to the difference in nuclear charge of $\Delta Z = 2$, in comparison to ^{53}Mn. The challenge of measuring ^{60}Fe are the very low ratios of the order of $R = 10^{-16}$ and the suppression of the stable isobar ^{60}Ni with a natural abundance of 26.22%, see fig. 29. Therefore, on the one hand FeO$^-$ is extracted from the source, which suppresses NiO$^-$ by an order of one magnitude. On the other hand, the gas-filled magnet should be used because of the high suppression capability, induced by the much larger energy loss of Ni compared to Fe inside the N_2 gas based on the higher nuclear charge of Ni. Isotopic ratios achievable for AMS measurements are 4.2×10^{-16} see Ludwig [83]. In this chapter the preparatory measurements with ^{58}Fe and ^{58}Ni are presented. These isotopes are both stable and therefore suitable to achieve good system settings and perform reproducible test measurements. Furthermore, the separation of ^{58}Fe and ^{58}Ni was investigated by testing different N_2 gas pressures inside the gas-filled magnet and isobutane gas pressures inside the used 5 anode ionization chamber.

5.1 Origin and Applications of ^{60}Fe

The isotope ^{60}Fe that can be measured here on earth, is produced by nucleosynthesis in s-processes in stars and supernova. The production rate strongly depends on the mass of the star, its temperature and the corresponding available neutron flux, since the main path of production is ^{59}Fe(n,γ)^{60}Fe, see Limongi et al. [84], whereby ^{59}Fe is also produced by neutron capture from ^{58}Fe and has a half-life of $T_{1/2} = 44$ d. The temperature range, in which ^{60}Fe is produced, is $T = 4 \times 10^8$ K to $T = 2 \times 10^9$ K. Beyond this point not enough neutrons are produced and the decay of ^{59}Fe hinders the production and above this temperature ^{60}Fe is destroyed by photodisintegration. Therefore, ^{60}Fe is most abundant in star with a mass range of $11\,M_\odot$ to $120\,M_\odot$, see Feige [85] for a good overview. The half-life of ^{60}Fe was determined by Rugel et al. [86] to $T_{1/2} = 2.62(4) \times 10^6$ a, and later confirmed by Ostdiek et al. [87] to $T_{1/2} = 2.55(26) \times 10^6$ a. In both cases the activity of a certain sample was measured as well as the ratio of ^{60}Fe/Fe of the same sample. The half-life was then calculated from this. The main application for ^{60}Fe AMS measurements is the investigation of interstellar processes like supernova, nucleosynthesis and the particle transport as well as the distribution of interstellar material. This is done by determine the ^{60}Fe/Fe ratio in see sediments or nodules as well as deep see crusts, see Fitoussi et al. [88].

Figure 29: Part of the nuclide chart showing ^{60}Fe as well as the corresponding isobar ^{60}Ni. Also indicated are, ^{56}Fe, ^{58}Fe and ^{58}Ni used for tuning purposes and first measurements.[4]

5.2 ^{58}Fe Tuning

The first and also important step before measuring a radionuclide for the first time, is to achieve stable and reproducible settings for the accelerator system and all beam focusing elements. For testing purposes, this was done with a stable ^{58}Fe beam, which is available in a sufficient intensity. For the following first test phase a 2 µm Mylar foil was glued to a 105 mm disk with a centered, 80 mm aperture, and installed right at the ISO-300 entrance flange of the new 135° magnet. In this way it was possible to test the settings and optical elements with a high acceptance. The disadvantage of is a higher energy loss compared to a SiN window, which is used for the later described measurements. The resulting energy loss for an 100 MeV ^{58}Fe beam can be calculated, by LISE++, to 11.173 MeV for a 2 µm Mylar foil compared to 1.116 MeV generated from a 200 nm Si$_3$N$_4$ window.

The injector was, in a first stage, tuned to ^{56}FeO$^-$ which has a quite high abundance of 91.75%.[5] This was done to test different sample materials. The best results could be obtained for Fe$_2$O$_3$ + Ag with a mixing ratio of about 1:1, which produced a beam output of 1.7 µA after the low energy 90° magnet. Due to the new power supply installed at the low energy magnet, the applied current is controllable via an Ethernet connection, with a resolution of 16-bit, see sec. 3.5.1. Therefore, it is not longer necessary to fine tune the beam by changing the bouncer voltage. A trace of an Fe$_2$O$_3$ sample, measured right after the low energy 90° magnet is given in fig. 30. Such a trace is a good opportunity to verify the selected mass and the beam tuning, by checking the ratios of stable isotopes like ^{63}Cu (69.15%) and ^{65}Cu (30.85%), which are sputtered from the cathode material. The resulting values are given in tab. 7.

[4] Generated with Nuclids2tex, Lifetimes, Decays and Abundances extracted from National Nuclear Data Center, Retrieved February 11,2019 from www.nndc.bnl.gov

[5] National Nuclear Data Center, Retrieved February 11,2019 www.nndc.bnl.gov
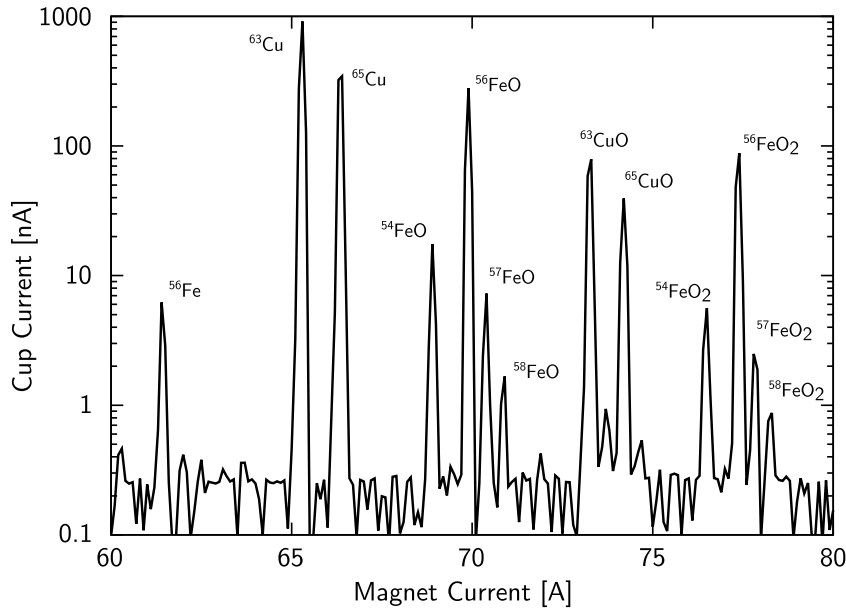
Figure 30: Mass spectrum after the 90° LE magnet using a Fe$_2$O$_3$ sample. The spectrum clearly shows all relevant masses and molecules, such as Fe, FeO and FeO$_2$ as well as Cu and CuO produced by sputtering the cathode itself. The related currents and measured abundances are given in tab. 7. The high mass resolution of 353(43), see [89], and the small step size of the magnet power supply, in the plotted case $\Delta I = 0.1$ A, allow a clear mass selection, even at m = 90 [u].

The next section is the low energy side from the pre-acceleration up to the LE Faraday cup in front of the accelerator itself. The installed Einzel lens in combination with the 70 kV pre-acceleration provide good focusing possibilities. To get a good transmission of up to 100%, it is crucial to tune the beam with open x-slits, which are installed right after the 20° magnet, which is only used for the second Cs sputter source and the Duoplasmatron. The transmission through the 10 MV Tandem accelerator was determined for protons by Markus Schiffer [3], to be about 50%. In the case of ^{56,58}Fe a measurable current, at the HE Faraday cup, 10-times the current at the LE Faraday cup was reproducible achievable, which includes the injected iron as well as the oxygen. For ^{56,58}Fe and ^{58}Ni the 10^+ charge state was chosen with an energy of 100 MeV. Therefore, the terminal voltage U$_T$ was set to 9.25 MV and the magnetic field of 90° analyzer magnet II to B = 9966 G. The magnetic field, measured by a NMR probe, turned out to be very reliable. Therefore, the terminal voltage can be tuned to achieve the best transmission to the analyzer Faraday cup, installed right after the 90° analyzer magnet II. In this way it was possible to detect a terminal voltage offset of about 30 kV, by measuring different charge states with pre-calculated values for the magnetic field. Based on the selected energy and the chosen charge state, the settings for the following elements can be calculated with good accuracy. The resulting transmission from the Faraday cup in front of the ESA to the Faraday cup behind the ESA is about 100% and also the transmission to the TOF Faraday cup right in front of the 135° magnet is at 100%. The x-slit pair after the ESA can also be used to ensure a beam position at the optical axis. The installed quadrupoles, in front of and after the ESA, should be operated symmetric.

At this point it is absolutely necessary to reduce the beam intensity to 200 pA or less otherwise the entrance foil to the magnet could be destroyed. The best way to achieve this is to cut the beam at the x-slits, on the low energy side, after the 20° magnet or if necessary reduce the ionizer

current. In this way, the beam focusing remains unchanged. Detailed descriptions concerning the tuning of the 135° magnet and the performed test measurements are given in the following sections.

Table 6: Settings for the 10 MV Tandem accelerator, the used MC-SNICS ion source and the new 135° magnet to measure ^{58}Fe at 100 MeV.

Section	Component	Value		Section	Component	Value	
MC-SNICS	Cathode Volt.	4.700	kV	HE	Steerer x1	1.20	kV
	Sputter Curr.	0.160	mA		Steerer x2	0.0	kV
	Cs-Focus	3.800	kV		Steerer y1	0.0	kV
	Extraction	12.008	kV		Steerer y2	−0.89	kV
	Einzel Lens	10	V		Quadrupole 1	0.443	A
	Ionizer	19	A		Quadrupole 2	0.453	A
	Cs-Oven	0	A	HEM	Magnet Curr.	190.0	A
Injector	Steerer y1	263	V		Magnet	9980.7	G
	ESA Volt.	1608.91	V		Steerer y1	0.15	A
	Magnet	60.873	A	HEQ	QP Triplet 1	31.3	A
	Bouncer HV 1	20	V		QP Triplet 2	28.3	A
	Bouncer HV 2	0	V	HEE	Slits x	open	
	Bouncer HV 3	0	V		Quadrupole 1	9.291	A
	Steerer x1	133	V		Quadrupole 2	18.177	A
	Steerer y2	−135	V		ESA Volt.	83.580	kV
	Steerer x2	62	V		Quadrupole 3	18.177	A
	Steerer y3	42	V		Quadrupole 4	9.291	A
LE	Pre-Acc.	54.000	kV		Slits x	open	
	Einzel Lens 0	15.000	kV	GFM	Quadrupole 5	13.100	A
	Einzel Lens 1	35	kV		Quadrupole 6	17.420	A
	Steerer x1	0.85	kV		Magnet Window	200	nm
	Steerer x2	−0.42	kV		Magnet Curr.	117.5	A
	Steerer y1	0	kV		Magnet	7780.6	G
	Steerer y2	0.1	kV		Pressure	5	mbar
	Einzel Lens 2	46.0	kV	Detector	Window	1000	nm
	Einzel Lens 3	0.5	kV		Pressure	40	mbar
ACC	Terminal Voltage	9.240	MV		Anode Volt.	500	V
	Terminal Steerer	−10.00	au		Frisch-Grid Volt.	250	V

Table 7: The table shows the measured low energy mass distribution after the 90° magnet of a Fe$_2$O$_3$ sample compared to the literature values,[6] the corresponding spectrum is fig. 30. The obtained distribution is in very good agreement with the predicted one, especially for FeO$^-$ and CuO$^-$. By comparing the measured abundances to the predicted the selected mass can be validated.

Mass [u]	Beam	I [nA]	Abundance [%]	Abundance [%] (lit.)
54	^{54}Fe$^-$	0.26	3.93	5.85
56	^{56}Fe$^-$	6.02	90.17	91.75
57	^{57}Fe$^-$	0.22	3.22	2.12
58	^{58}Fe$^-$	0.18	2.68	0.28
63	^{63}Cu$^-$	914.32	72.60	69.15
65	^{65}Cu$^-$	345.13	27.40	30.85
70	^{54}FeO$^-$	17.31	5.68	5.85
72	^{56}FeO$^-$	278.76	91.52	91.75
73	^{57}FeO$^-$	7.07	2.32	2.12
74	^{58}FeO$^-$	1.46	0.48	0.28
79	^{63}CuO$^-$	78.94	66.85	69.15
81	^{65}CuO$^-$	39.14	33.15	30.85
86	^{54}FeO$_2^-$	5.41	5.63	5.85
88	^{56}FeO$_2^-$	87.87	91.41	91.75
89	^{57}FeO$_2^-$	2.29	2.38	2.12
90	^{58}FeO$_2^-$	0.56	0.58	0.28

5.3 Charge State Investigations for ^{58}Fe and ^{58}Ni after the 135° Magnet

The investigation of all populated charge states generated by passing the entrance foil was the next step of putting the 135° magnet into operation. In this way the beam tuning and transport properties were tested. A detailed investigation concerning the optimal N$_2$ gas pressure and the resulting spectra is given in sec. 5.4.1. The charge states populated most for ^{58}Fe (Z = 26) and ^{58}Ni (Z = 28) at 100 MeV, after passing a 2 µm Mylar foil, are 18$^+$ and 19$^+$, respectively. All relevant charge states where calculated from eq. 2.7 and following Betz [29], see tab. 8. During the measurements, all calculated charge states with an abundance of 1% and more could be detected at the GFM Faraday cup which was installed right after the new 135° magnet. For later measurements the Mylar foil was replaced by a much thinner, 200 nm, SiN foil to reduce the energy loss and straggling. The result of these first scans with the new magnet are combined and given in fig. 31. The black line indicates the ^{58}Fe scan and red line indicated ^{58}Ni. The given charge states refer to both isotopes. For ^{58}Fe the charge states 15$^+$ to 21$^+$ and for ^{58}Ni the charge states 17$^+$ to 22$^+$ could be identified, respectively. The distribution reproduces the theoretical values given in tab. 8 and indicated in fig. 32. In addition it was possible to determine

[6] National Nuclear Data Center, Retrieved April 15,2018 www.nndc.bnl.gov
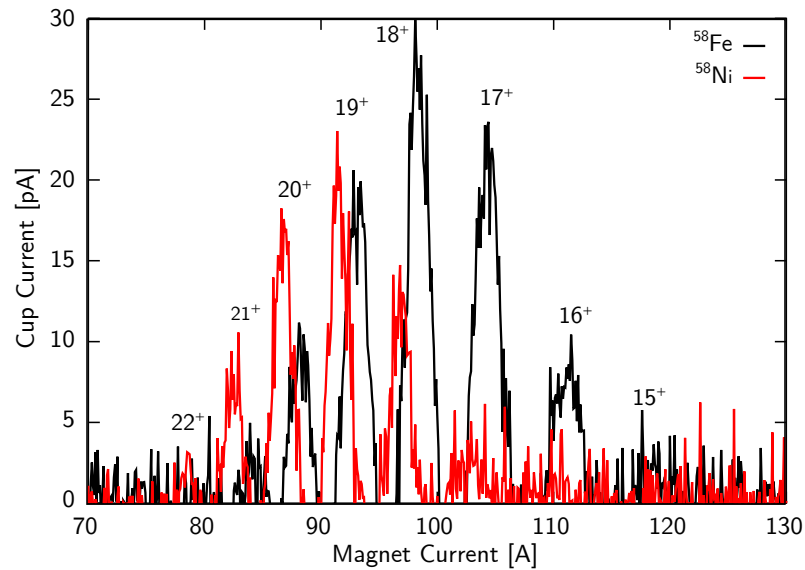
Figure 31: This plot shows the combined spectra of the first performed charge state measurements of ^{58}Fe (black) and ^{58}Ni (red) at 100 MeV beam energy, after the new 135° magnet without N$_2$ gas, with a 2 μm Mylar entrance window. The indicated charge states refer to both isotopes. For ^{58}Fe the states 15^+ to 21^+ and for ^{58}Ni the states 17^+ to 22^+ could be identified. The infected beam intensity, measured at the TOF Faraday cup was 100 pA and 80 pA for ^{58}Fe and ^{58}Ni, respectively.

the transmission through the magnet, without gas. Due to the lower energy and angular straggling it is no identical to the transmission that can be achieved in the later intended gas-filled mode. The transmission was calculated by determine the maximum beam intensity of all detectable charge states. Based on the known injected beam intensity of 100 pA, the achieved transmission is 53%.

During this test measurements also single charge changing processes should be investigated.

Table 8: Charge state distributions of ^{58}Fe and ^{58}Ni both at 100 MeV beam energy after a 2 μm Mylar foil. Measured in the GFM Faraday cup after the 135° magnet. The literature values are calculated from eq. 2.7. The measured distributions both in charge state as well as the related abundance fit the calculated values.

Charge State	Fe			Ni		
	I Cup [pA]	Meas. [%]	Calc. [%]	I Cup [pA]	Meas. [%]	Calc. [%]
15	3	3.77	1.60	0	0	0.19
16	9	10.60	7.69	0	0	1.60
17	22	24.38	19.94	2.50	4.65	7.22
18	28	29.31	29.23	12.50	21.97	18.44
19	20	19.83	25.08	19.50	32.46	27.75
20	10	9.42	12.38	16	25.31	25.40
21	3	2.69	3.37	7.50	11.30	14.02
22	0	0	0.48	3	4.31	4.49
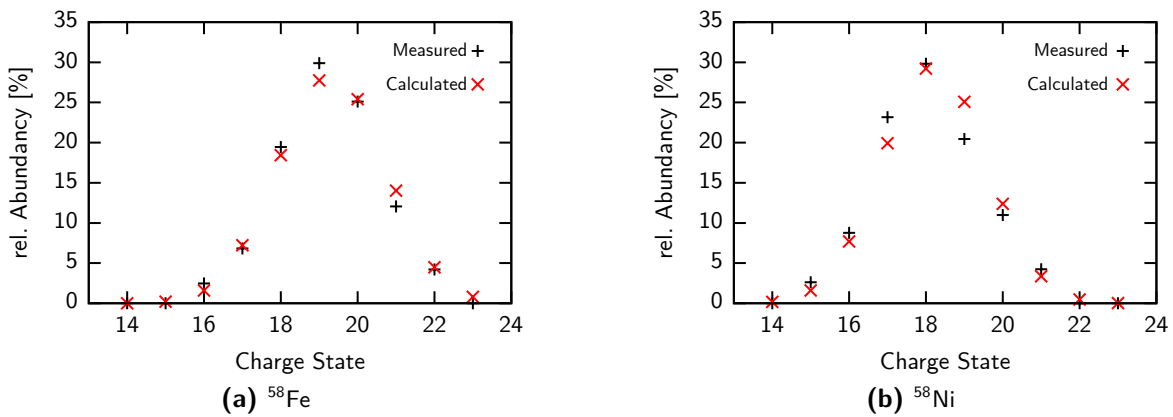
(a) ^{58}Fe

(b) ^{58}Ni

Figure 32: Charge state distribution of a) ^{58}Fe and b) ^{58}Ni, measured at 100 MeV initial beam energy, after a 2 µm Mylar foil. Theoretical values calculated from eq. 2.7 are listed in tab. 8.

Due to the short mean free flight path, of a few mm, and the relatively long distance of 2121 mm through the magnet a quite low pressure is required to detect charge states close to the injected 10^+. This was realized by differential pumping the magnet from both sides, entrance end exit, without a foil. Hereby it was possible to set pressures of about 2 mbar. Higher gas flows could affect the closest turbo molecular pumps. In fig. 33 a trace of the 135° magnet is given. During the trace a ^{58}Fe^{10+} beam was injected at a N$_2$ gas pressure of approximately 2 mbar. The measurable states are between 10^+ and 16^+. The spectrum was calibrated with the 10^+ state. All higher states tend to the mean charge state 12^+. Due to the energy loss from single interactions without changing the charge state the peak form of the 10^+ and 11^+ probably show tails to the left side. For further investigations of single charge transfer, a dedicated gas cell should be build.
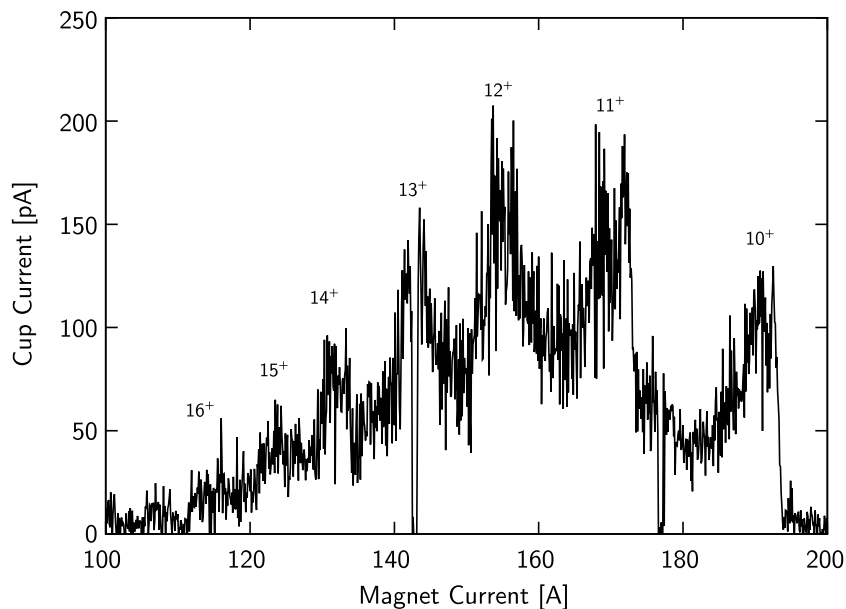
Figure 33: Trace of the 135° magnet of an ^{58}Fe beam at approximately 2 mbar N$_2$ gas pressure, without the entrance foil. The pressure was achieved by differential pumping from both sides of the magnet vacuum chamber.

5.4 Separation and Suppression Studies for ^{58}Fe and ^{58}Ni

The most important aspect for AMS measurements of ^{60}Fe at very low ratios in the order of $R = 10^{-16}$ is the separation and suppression of the very abundant ^{60}Ni. To this end several measurements and tests were carried out to investigate the capabilities of the dedicated AMS beam line at the 10 MV Tandem accelerator in combination with the new 135° gas-filled magnet. In this context the separation between ^{58}Fe and ^{58}Ni using the 10 anode ionization chamber, at identical beam energies, was determined, see sec. 3.6.2, as well as the separation of the new 135° magnet in a gas-filled mode was tested. Furthermore, the new 5 anode ionization chamber was installed for a second set of measurements. In order to determine the position, width and spatial separation, a silicon detector (Si-Detector) was installed after the 135° magnet. A big advantage of ^{60}Fe, over other isotopes of interest for AMS measurements, is the existence of the stable isotopes ^{58}Fe and ^{58}Ni. This makes it possible to determine the expected separation of ^{60}Fe and ^{60}Ni background and the transmission throughout the new beam system, without using extreme rare ^{60}Fe sample material. The objective of these investigations is to provide a way to measure background levels of down to ^{60}Fe/Fe $= 2 \times 10^{-17}$ as presented by Ludwig [83] in the future. In the mentioned case the separation of ^{58}Fe and ^{58}Ni was also achieved with the 135° gas-filled magnet.

5.4.1 Optimization of the N$_2$ Gas Pressure at the New 135° Magnet

To optimize the N$_2$ gas pressure means, on the one hand to maximize the isobar separation and on the other hand, to keep the energy loss and the angular straggling as low as reasonable achievable to allow a good transmission and a good separation inside the subsequent ionization chamber. The importance of the remaining energy was pointed out in sec. 3.6.2. The measurements described below were conducted with a ^{58}Fe^{10+} and a ^{58}Ni^{10+} beam at a initial beam energy of 100 MeV each.

In this section test measurements with different N$_2$ gas pressures performed with the Faraday cup after the gas-filled magnet for both isotopes, ^{58}Fe and ^{58}Ni, are descried. The energy loss in this pressure region of 2 to 8 mbar, per mbar of N$_2$ gas is about 9.0 MV/mbar and 9.8 MV/mbar for ^{58}Fe and ^{58}Ni, respectively. In fig. 34 the results of eight different measurements at four different pressures are plotted. Both isotopes were measured right after another, to keep the beam focusing untouched. In this way it was possible to ensure the same conditions for each measurement. For a better comparability of ^{58}Fe and ^{58}Ni the currents were normalized to the area under each Gaussian fit. The resulting mean μ and width σ of the measured beam distributions obtained from fitting are given in tab. 9. The determined separation factors are only to a limited extend comparable to later measurements since the resulting spectra and distribution width are a superposition of the ion beam distribution, the changed ion optics by tuning the magnet and the large Faraday cup aperture. Furthermore, the rising gas pressure inside the vacuum chamber, and therefore also inside the Faraday cup, leads to imprecise current measurements. These problem was solved by measurements with a silicon detector in combination with a narrow aperture, described below.

(a) Measured distribution of ^{58}Fe and ^{58}Ni at 2 mbar N_2 gas pressure. $S_f = 2.58(2)$

(b) Measured distribution of ^{58}Fe and ^{58}Ni at 4 mbar N_2 gas pressure. $S_f = 3.05(2)$

(c) Measured distribution of ^{58}Fe and ^{58}Ni at 6 mbar N_2 gas pressure. $S_f = 3.51(2)$

(d) Measured distribution of ^{58}Fe and ^{58}Ni at 8 mbar N_2 gas pressure. $S_f = 3.52(3)$
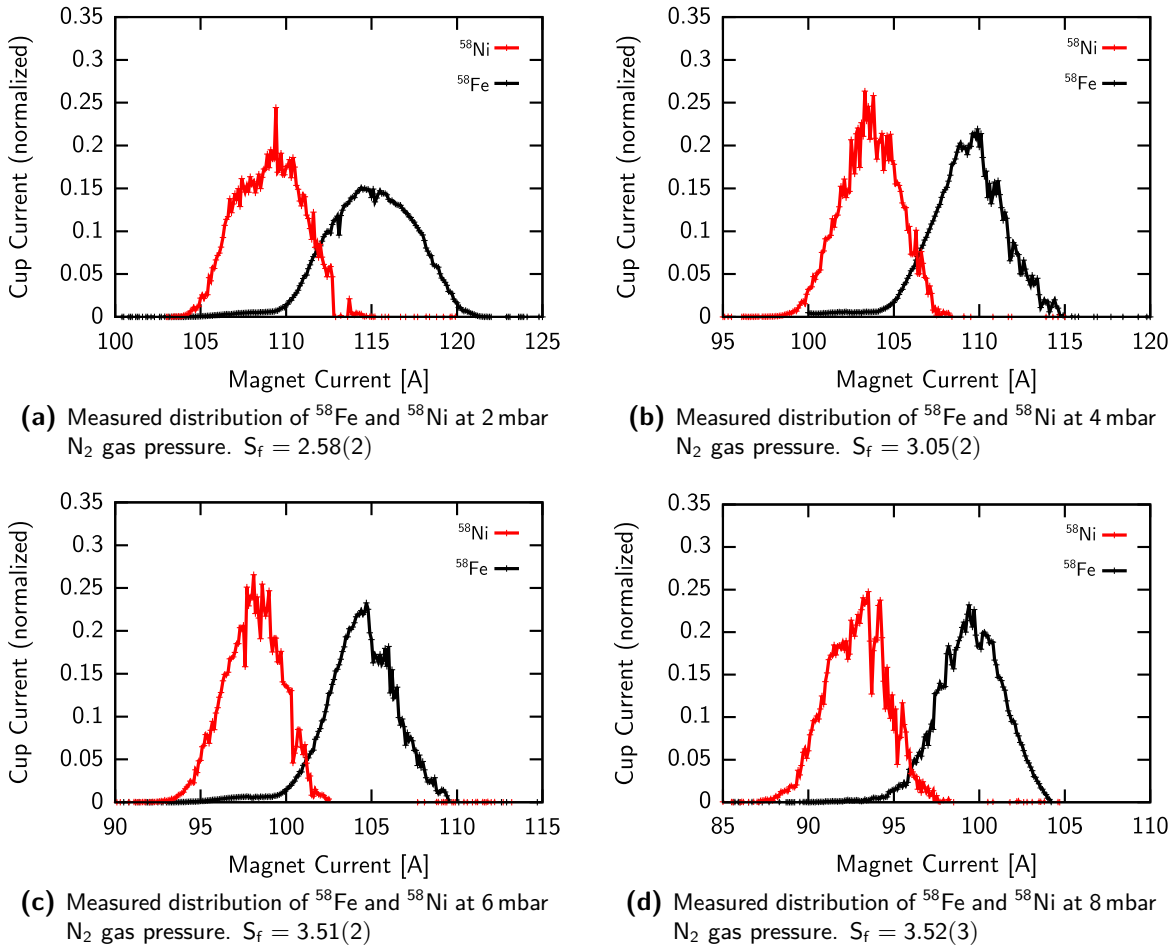
Figure 34: Indicated are from (a) to (d) the measured separation of ^{58}Fe(black) and ^{58}Ni(red) for N_2 gas pressures of 2 to 8 mbar in steps of 2 mbar. For each tested pressure the sample was changed and the beam tuning stays untouched to obtain reproducible circumstances. Each measured distribution was fitted with a Gaussian distribution the result is given in tab. 9.

Table 9: Separation factors S_f for ^{58}Fe/^{58}Ni at different N_2 gas pressures with an initial energy of 100 MeV at the 10^+ charge state and a 2 μm Mylar window. Measured at the 10 MV Tandem accelerator with the GFM Faraday cup by tuning the magnetic field.

N_2 gas [mbar]	Isotope	E_{Loss} [MeV]	σ [A]	μ [A]	S_f
2	Fe	18.12	2.59(2)	115.08(2)	2.58
	Ni	19.62	2.08(2)	109.05(3)	
4	Fe	36.28	2.00(2)	109.38(2)	3.05
	Ni	39.20	1.77(2)	103.63(2)	
6	Fe	54.44	1.89(1)	104.44(1)	3.51
	Ni	58.68	1.71(2)	98.13(2)	
8	Fe	72.50	1.89(1)	99.57(1)	3.52
	Ni	77.96	1.82(3)	92.85(3)	

Another point that could be observed for each tested Fe sample is a measurable Ni background. This contamination is in the percentage range and visible in all shown measurements. To provide an indication of the extent of the contamination, see fig. 34. Neither different iron sample materials and cleaned up pressing tools, nor a different sample order during the measurement could prevent this background. Therefore, also a short term memory effect could be excluded. A long term memory effect, of the source, or a contamination of the used cathodes or the sample wheel could not be excluded. Another explanation could be the contamination of the used material itself.

Based on this findings, a new entrance window was mounted to the vacuum chamber of the magnet. The new 200 nm thick and 12×12 mm^2 entrance window reduces the energy losses for Fe and Ni by almost 10 MeV, which is about 10% of the total beam energy. To further improve the performance, the entrance window was mounted to the top of a 250 mm rod and inserted into the vacuum chamber. Therefore, the different charge states are populated inside the magnetic field and not in front of it. In this way losses should be reduced which are induced by energy loss and charge state changes in a field free region. After changing the entrance window of the magnet vacuum chamber, the beam intensity of the used stable ^{58}Fe and ^{58}Ni beams had to be reduced further to $I_{Beam} < 100$ pA and no stable beam current could be measured at the Faraday cup after the gas-filled magnet any more. Therefore, the existing Faraday cup was removed and a Si-Detector was installed from the right side towards beam direction. The detector was mounted to a linear actuator with a total driving distance of 100 mm, which covers the entire width of the beam tube, and was equipped with a 1 mm wide (x-direction) slit aperture. Furthermore, the Si-Detector was connected to the MPA data acquisition system. In this way, the spatial separation, width, shape and relative energy loss of ^{58}Fe and ^{58}Ni beam at different N$_2$ gas pressures could be determined in x-direction. In a first step the stable ^{58}Fe beam was tuned through the whole system and into the ionization chamber. From this point on, only the N$_2$ gas pressure and the magnetic field of the 135° magnet were changed. In a second step the Si-Detector was moved in steps of 5 mm though the beam and the corresponding count rate was recorded. The width and shape of ^{58}Fe and ^{58}Ni were investigated separately on the optical axis, by tuning the 135° magnet, to achieve comparable conditions for both components. In a third step, a beam was extracted from a mixed Fe-Ni sample, and the ^{58}Fe component was shifted to the right side (in beam direction), by reducing the magnetic field. Therefore, both components ^{58}Fe and ^{58}Ni could be detected by moving the Si-Detector through the beam tube, provided that they are separated not more than 100 mm. The resulting spatial separation for all three tested N$_2$ gas pressures, 3 mbar, 5 mbar and 7 mbar, is given in tab. 10. The indicated values are

Table 10: The table listed the spatial separation d between ^{58}Fe and ^{58}Ni measured at three different N$_2$ gas pressures after the new 135° gas-filled magnet. All measurements were performed with a silicon detector. The position μ and the width σ are determined by Gaussian fits.

N$_2$ gas [mbar]	Isotope	E$_{Loss}$ [MeV]	σ [mm]	μ [mm]	d [mm]	S$_f$
3	^{58}Fe	27.14	13.9(10)	31.5(14)	58(2)	1.93
	^{58}Ni	29.38	10.6(15)	89.5(15)		
5	^{58}Fe	45.25	13.3(7)	20.7(7)	68(1)	2.07
	^{58}Ni	48.79	13.6(10)	88.9(10)		
7	^{58}Fe	62.99	12.0(3)	19.2(3)	84(1)	3.48
	^{58}Ni	67.44	7.7(7)	103.3(6)		
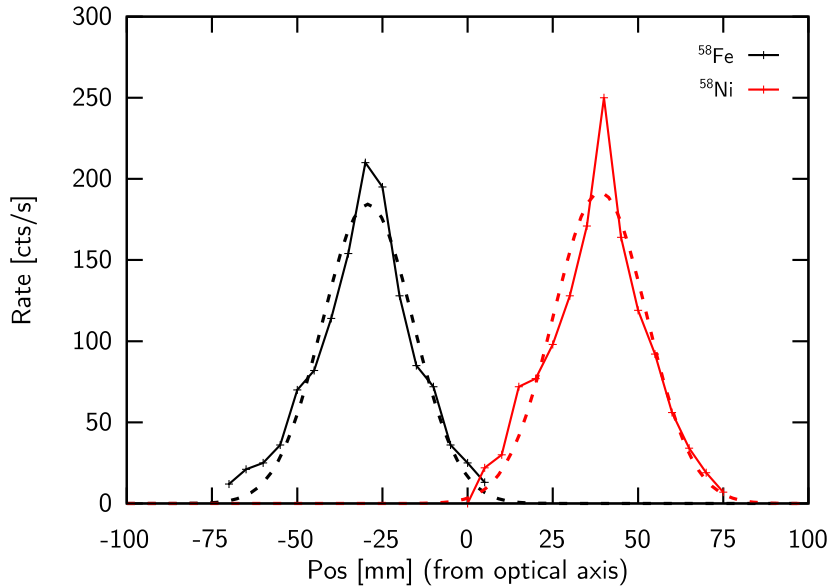
Figure 35: The figure shows the spatial separation between ^{58}Fe and ^{58}Ni after the gas-filled magnet at 5 mbar, measured with a silicon detector. The measurement was performed in two steps. First the beam profile was scanned, with both components tuned to the optical axis. In the second step the separation was determined. Both distributions are shifted to the corresponding position to indicate the achieved separation. The mean and width of each distribution was determined with a Gaussian fit, which is displayed by the dotted line.

a combination of both measurement steps, the individual beam width determination as well as the separation. Due to the relatively large spatial distance between the components, it is not possible to measure the beam profile and separation in the same measurement. Therefore, the measured profiles are shifted to the position detected in the second measurement, see fig. 35. The mean and the width were determined with two Gaussian fits and added to the figure as dotted lines. The achieved spatial separation, of up to 84 mm, is similar to the spatial separation given by Knie et al. [58] (about 80 mm for 7.5 mbar at 160 MeV), Paul et al. [45] (about 100 mm for 18.7 mbar at 350 MeV) or Ludwig [83] (about 100 mm for 7 mbar at 130 MeV).

The installed Si-Detector allowed also to measure the remaining total energy. In general it would be possible to measure absolute energy values with this type of detector. According to the used preamplifiers, the high voltage signals provided by the Si-Detector during a measurement of particles with an energy of about 30 MeV, could not be handled and had to be attenuated by the factor of about 20. Therefore, only statements concerning the relative energy loss are given hereinafter. By comparing the peak position detected by the Si-Detector, of each N_2 gas pressure, with the corresponding calculated energy loss E_{calc}, the relative energy loss E_{rel} could be calculated and is given in fig. 36. The calculation revealed a good agreement of the energy loss calculated with LISE++, based on the set pressure, and the measured remaining energies.

5.4.2 ^{58}Fe Measurements with the 5 Anode Ionization Chamber

The 10 anode ionization chamber used so far is, in its actual configuration and with the available MPA3 system, suitable to only a limited extent for the used isotopes and beam energies, as described in sec. 3.6. Therefore, it was replaced with the new 5 anode ionization chamber. This

(a) Energy spectra of ^{58}Fe at three different N$_2$ gas pressures.

(b) Combined energy spectra of ^{58}Fe and ^{58}Ni 5 mbar N$_2$ gas pressure.
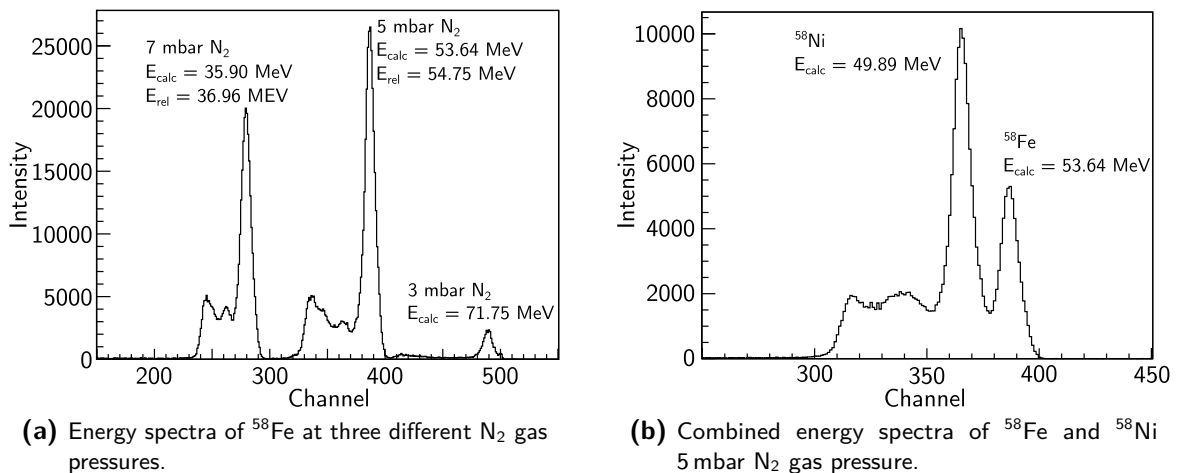
Figure 36: The figures shows energy spectra measured with the Si-Detector installed after the 135° gas-filled magnet. Figure a) shows three measurements of ^{58}Fe at different N$_2$ gas pressures. All shows a linear connection in distance and therefore in energy. The given energies are calculated with LISE++. Figure b) shows the ^{58}Fe and ^{58}Ni measurement 5 mbar. The resulting energy resolution is 0.17(4) MeV/Channel.

new ionization chamber was tested beforehand during a ^{10}Be AMS measurement at the 6 MV Tandetron™ accelerator and provided good results, see sec. 3.7.4. The detector is mounted to a stable structure based on aluminum profiles, which holds the housing on both sides as well as the preamplifiers close to the detector. A 1000 nm thick SiN foil, with a size of 20×20 mm^2, is used as entrance window, which is the largest actual available SiN window. But based on the measurements performed with the Si-Detector, this will reduce the acceptance to about 56% for a beam width of $\sigma = 13$ mm.

In the following described set of measurements, the position of ^{58}Fe and ^{58}Ni beam components and the separation achieved with the new 5 anode ionization chamber were investigated. For this purpose ^{58}Fe and ^{58}Ni were measured with the exact same system settings except the magnetic field of the 135° gas-filled magnet. The ^{58}Fe beam was optimized by the count rate at the ionization chamber. The change of the magnetic field was required, due to the lack of measurable ^{58}Ni within an appropriate time, for the system tuned to ^{58}Fe. During the investigation, the pressure was set to a low value of 20 mbar and stepwise raised to 40 mbar. If the pressure is too low, the particles are not stopped withing the active detector volume and the important dE/dx information of the Bragg-Peak gets lost. As a result of this, the separation of the radionuclide and the corresponding isobar gets worse. A good example is given in fig. 37a. The plot shows in total four measurements at the same system settings and a N$_2$ gas pressure of 5 mbar, but with two different isobutane gas pressures, 25 mbar and 40 mbar. Since not the total particle energy is deposited to the active detector volume, the position of the ^{58}Fe peak is beyond the ^{58}Ni peak, which looses more energy per length unit in the same gas pressure than ^{58}Fe. At this point a second important observation was made. The ^{58}Ni component is shifted to lower energies compared to the ^{58}Fe peak position. Even for a good isobutane gas pressure the components do not form the former described total energy diagonal. The fact is related to the difference in energy loss and mean charge state q$_m$, between Fe and Ni inside the gas-filled magnet, see fig. 36b.

This is clearly shown in fig. 37b. The graph displays in total six measurements at three different N$_2$ gas pressures, 3 mbar, 5 mbar and 7 mbar. The effect and therefore the shift of the

(a) Different isobutane gas pressures

(b) Different N$_2$ gas pressures
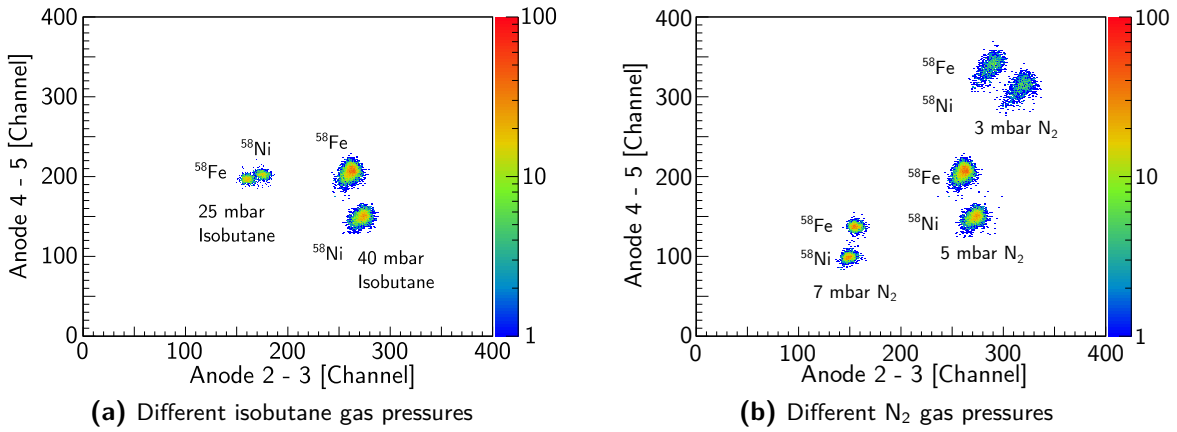
Figure 37: In figure a) two different isobutane gas pressures for ^{58}Fe and ^{58}Ni at 5 mbar N$_2$ gas pressure are shown, 25 mbar and 40 mbar. If the pressure is two low, not all of the particles energy is deposited inside the active detector volume and therefore the separation is decreasing. Figure b) shows the shift of the ^{58}Ni regarding the ^{58}Fe peak position according to the N$_2$ gas pressure inside the gas-filled magnet. The first anode was left out, since the detected signals indicate a disruption of the electric field, which could not be fixed.

Ni component becomes larger for higher pressures, which is described in sec. 2.2.7. Since the separation of both components can not longer be calculated by projecting the 2-dim histogram to an 1-dim distribution along the total energy diagonal, see fig. 38a, each measured peak has to be fitted by a 2-dim Gaussian distribution P(x,y), compare fig. 38b.

$$P(x, y) = \frac{1}{2\pi\sigma_x\sigma_y\sqrt{1-\rho^2}} \exp\left[-\frac{z}{2(1-\rho^2)}\right] \tag{5.1}$$

$$\text{where:} \quad z = \frac{(x-\mu_x)^2}{\sigma_x^2} - \frac{2\rho(x-\mu_x)(y-\mu_y)}{\sigma_x\sigma_y} + \frac{(y-\mu_y)^2}{\sigma_y^2} \tag{5.2}$$

The correlation coefficient between x and y is given by ρ. As ρ increases, the contour according to the xy plane, changes from a roundish shape to an ellipsoidal shape. This ellipsoidal shape is described by eq. 5.2 and determines the 1σ environment of the measured peak. After fitting both peaks, ^{58}Fe and ^{58}Ni, all parameters are known including each peak centers. Between this centers, a straight line was defined and equated with both ellipsoids, respectively. The distance between the resulting intersection points is the closest distance between both peaks, see de Maesschalck et al. [90]. Furthermore, the intersection points determine the 1σ width of each measured distribution in the direction of the corresponding isobar. In this way it is possible to calculate a separation factor for two components independent from their position to each other. Furthermore, this approach overestimates the width of the distribution to a lesser extend than a projection does. The best result could be determined at 7 mbar N$_2$ gas pressure and 28 mbar isobutane gas pressure and is given in fig. 39. The separation factor is S$_f$ = 4.76. A better comparability to earlier measurements, performed with the 10 anode ionization chamber described in sec. 3.6.2, is given by the measurements at 5 mbar, since the remaining energy after the N$_2$ gas is in both cases around 54 MeV. The achieved separation factor at 40 mbar isobutane gas is S$_f$ = 4.25. During the test measurements with the 10 anode ionization chamber the separation

factor was $S_f = 2.78$ and therefore 64% smaller, which results from the difference in energy between the isotope and its isobar entering the detector. It should be noted here, that all shown ^{58}Fe and ^{58}Ni spectra in this section are combined from at least to different measurements, at two different magnetic fields for the 135° magnet. As long as the system is tuned to ^{58}Fe, even if a Ni sample is put into the MC-SNICS ion source, no counts could be detected inside the ^{58}Fe ROI within several minutes of measurement.

(a) Determination of the energy diagonal line and the resulting separation factor, without different energy losses. The Gaussian fits are given in a logarithmic scale.

(b) Example of a 2-dim Gaussian fit to an ^{58}Fe and a ^{58}Ni peak. The fits are raist in z position in the interest of greater legibility.
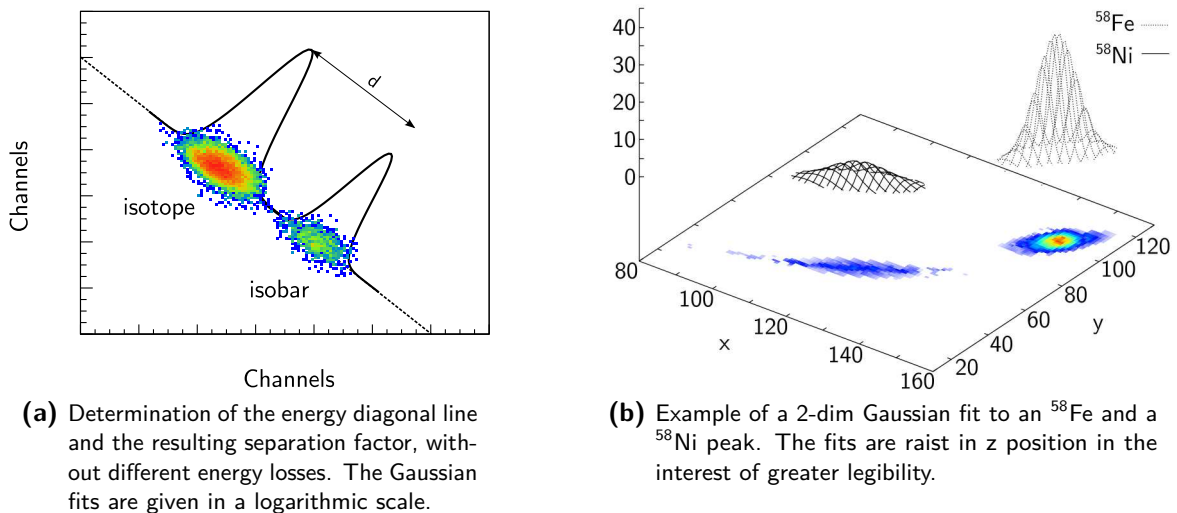
Figure 38: The figure explains the differences between the standard way of determine the separation factor and the 2-dim Gaussian analysis required for measurements performed with a gas-filled magnet.
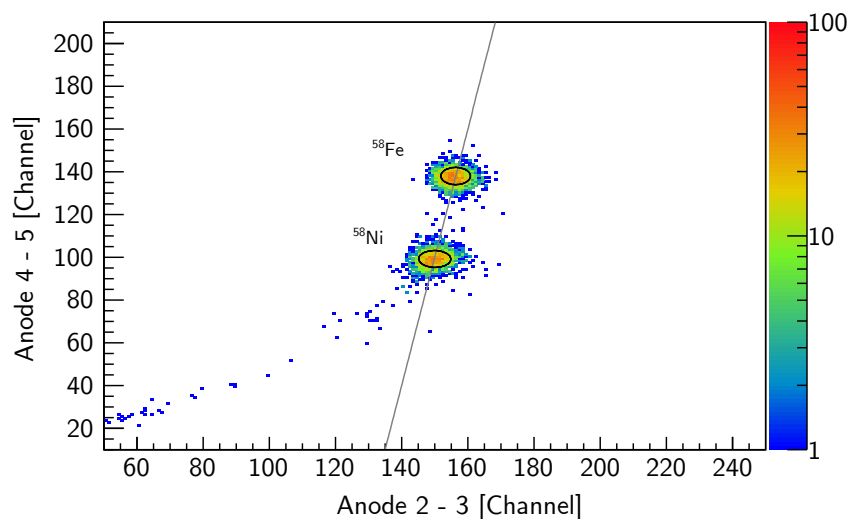
Figure 39: The plot shows the result of the measurement with the best achieved separation factor between ^{58}Fe and ^{58}Ni of $S_f = 4.76$ at 7 mbar N_2 gas pressure inside the gas-filled magnet and 28 mbar isobutane gas pressure inside the ionization chamber. The separation was determined by using the 2-dim Gaussian analysis. The straight is defined by both mean values μ_{Fe}, μ_{Ni} and the plotted ellipses are the projection of the Gaussian distributions at half maximum (FWHM).

Chapter 6

Accelerator Mass Spectrometry of ^{41}Ca at the 6 MV Tandetron™ Accelerator

Measurements of the cosmogenic radionuclide ^{41}Ca are described from various institutes around the world. In the course of this thesis reproducible settings and procedures were developed to measure reliable isotopic ratios for ^{41}Ca at the Cologne 6 MV Tandetron™ accelerator. In the beginning of the chapter, a short introduction to the origin of ^{41}Ca on earth and the actual applications are given. This is followed by descriptions concerning beam focusing as well as the first test measurements with blank and standard samples with a well known ratio of ^{41}Ca/^{40}Ca. The results according to blank level, correction factors and the isobaric contamination with ^{41}K are discussed afterwards. In a second part, the first measurements and results of neutron irradiated concrete samples are given. The concrete was irradiated in a controlled way, to produce samples with ^{41}Ca/^{40}Ca ratios of several orders of magnitude. In this section the potential of AMS measurements with respect to the classification of construction material used for nuclear facilities will be discussed.

6.1 Origin and Applications of ^{41}Ca

The radionuclide ^{41}Ca is produced by thermal neutron capture, through the reaction ^{40}Ca(n,γ)^{41}Ca, with a capture cross section of $\sigma = 0.40(4)$ barn, see Cranston et al. [91]. A second production way is spallation of Ti, Cr or Fe, see Dunai [73] and Nishiizumi et al. [92]. The half-life of ^{41}Ca is $T_{1/2} = 1.04(5) \times 10^5$ a, see Nishiizumi et al. [92], and was determined by measuring the activity of a sample with a liquid scintillator and the amount of ^{41}Ca atoms in the same sample by thermal ionization mass spectrometry, see Jörg et al. [93].

The applications reach from exposure dating and the determination of terrestrial ages of meteorites, see Welten et al. [94], through medical investigation of ^{41}Ca as a biomarker in teeth, see Wallner et al. [95], to medical investigation of metabolic processes inside the human skeleton, see Freeman et al. [96] or investigations concerning bone cancer, see Shen et al. [97]. The estimated isotopic ratio of ^{41}Ca/^{40}Ca in meteoroids and other silicate rocks is $10^{-11} - 10^{-15}$. The ratio expected for teeth is about $< 10^{-14}$, for other biomedical applications it is between $10^{-10} - 10^{-11}$, compare Fink et al. [98]. The very low ratios in geological samples, in combination with the ^{41}K background, are challenging and in many cases unachievable, compare tab. 11.

A totally different application is the characterization of construction material used for nuclear facilities according to their radioactive contamination. In this way the upcoming task of decommissioning and dismantling can be handled. The radionuclide ^{41}Ca can possibly be used to classify the large amount of expected concrete and separate the contaminated parts from simple rubble. An overview to this topic is given in the report from the IAEA [99]. In the course of this thesis, this application is of special interest.

Figure 40: Part of the nuclide chart showing ^{41}Ca isotope as well as the corresponding isobar ^{41}K.[7]

6.2 Development of a Measuring Procedure for ^{41}Ca at the 6 MV Tandetron™ Accelerator

The measurement of ^{41}Ca at medium size accelerator facilities is common and used for a wide range of applications, see tab. 11. The Cologne 6 MV Tandetron™ accelerator is predestined for this type of measurements due to the high beam transmission through the accelerator itself as well as the following separation units. The project was investigated for the first time by Claus Feuerstein, see [10]. Since then routine operation was never accomplished due to high ^{41}K background and resulting low separation factors, which is discussed later on. In this section the measuring procedure is described and the results of the first measurements at the 4 anode HVE ionization chamber are discussed.

6.2.1 ^{41}Ca Tuning

The tuning procedure applied for ^{41}Ca at the 6 MV Tandetron™ accelerator is described hereinafter and differs from that used at the 10 MV Tandem accelerator, see sec. 5.2. Due to the fact that the whole beam system of the Tandetron™ accelerator is digitized and controllable from one PC unit, it is possible to load and restore former used settings with a high level of reproducibility. In the case of ^{41}Ca, no acceptance test where performed by HVE, as it is common for other isotopes. Beforehand the tuning started, the required voltages, for electric lenses and currents for the bending magnets were calculated from former known and often used settings of other isotopes. In this case the settings for ^{10}Be, ^{14}C and ^{36}Cl form the basis of the calculation. The calculated and the used E/q values and P/q values are given in tab. 12, for known settings and ^{40}Ca

[7] Generated with Nuclids2tex, Lifetimes, Decays and Abundances extracted from National Nuclear Data Center, Retrieved February 11,2019 www.nndc.bnl.gov

as well as ^{41}Ca. Each value for ^{41}Ca and ^{40}Ca, was calculated from the three known isotopes and averaged, although the variations are below 1%.

In a first step the stable ^{40}Ca beam was extracted from the SO-110 ion source as ^{40}CaF$_3^-$ and tuned through the system up to the Faraday cup after the high energy magnet (HEM). The terminal voltage was set to 5.8 MV following the report from DREAMS were the same accelerator is used for ^{41}Ca measurements, see Rugel et al. [108]. By running a tracing routine for each main component, like LE ESA, LE magnet and HEM, the beam was tuned to the optical axis. The deviation between the estimated field of $B_{est.} = 0.5625$ T and the set HEM magnetic field of $B_{set} = 0.5612$ T was $\Delta B = 0.0013$ T. For this reason it seems suitable to pre-calculate the settings from known values. Therefore, also the HE ESA as well as the dipole switching magnet (DSW) were set to the stated values. The measured electrical current for ^{40}Ca^{4+} at the accelerator (ACC) Faraday cup was $I = 154$ nA and $I = 107$ nA at the HEM Faraday cup, which is in the same order of magnitude as the reference values given in tab. 11. This results in a transmission to the selected charge state of about $T = 17\%$, which is in good agreement to the calculated value of about $T_{Sayer} = 12\%$. To ensure a high transmission the argon gas stripper pressure was tuned between 1×10^{-1} mbar and 8×10^{-3} mbar. Best results could be obtained for lower pressures of the order of $p_{Ar} = 8 \times 10^{-3}$ mbar. Even lower pressures are not stable and not reproducible due to the hardware limits of the thermo-leak which controls the gas inflow to the stripper channel. The beam was further tuned up to the GIC Faraday cup in front of the ionization chamber. In this way also the HE ESA and DSW magnet settings were checked. To verify the system settings, the 5^+ charge state was chosen and measured with an abundance of

Table 11: Institutes measuring ^{41}Ca. The majority of the institute use CaF$_3$ as a sample material exept CIAE, where CaF is used.

Institute	I_{NE} [nA]	TV [MV]	q	E [MeV]	Blank level	Measured R	
PSI	120	0.50	3^+	1.7	5.0×10^{-12}	4.0×10^{-11}	[100]
CNA	100	0.97	2^+	NaN	5.0×10^{-12}	4.0×10^{-11}	[101]
CIAE	95	8.50	9^+	82.5	1.5×10^{-13}	1.8×10^{-9}	[102]
CologneAMS	150	5.80	4^+	25.6	6.3×10^{-14}	4.7×10^{-13}	
UTTAC	100	6	7^+	44.5	6.0×10^{-14}	5.7×10^{-13}	[103, 104]
SUERC	320	5	5^+	27	3.0×10^{-14}	4.0×10^{-11}	[105]
VERA	150	3	4^+	13	1.0×10^{-14}	1.0×10^{-13}	[106, 107]
DREAMS	300	5.80	4^+	25.6	2.0×10^{-15}	1.0×10^{-12}	[108]

Table 12: The table shows the key parameters used to start the ^{40}Ca beam tuning. The bold parameters for ^{40}Ca and ^{41}Ca are calculated based on the E/q and p/q values for similar, well known beams and averaged.

Isotope	TV [MV]	E [MeV]	$\frac{E}{q} \left[\frac{MeV}{e}\right]$	$\frac{p}{q} \left[\frac{\sqrt{MeV \cdot u}}{e}\right]$	HEM [T]	ESA [kV]	DSW [T]
^{10}Be^{2+}	4.50	10.744	5.3721	7.3294	0.3647	64.83	0.4807
^{14}C^{4+}	5.50	27.535	6.8874	6.9416	0.3451	82.94	0.4518
^{36}Cl^{5+}	6.00	36.035	7.2070	10.1870	0.5060	86.97	0.6662
^{40}Ca^{4+}	5.80	25.606	6.4015	11.3151	**0.5625**	**77.19**	**0.7395**
^{41}Ca^{4+}	5.80	25.641	6.4103	11.4635	**0.5699**	**77.30**	**0.7492**
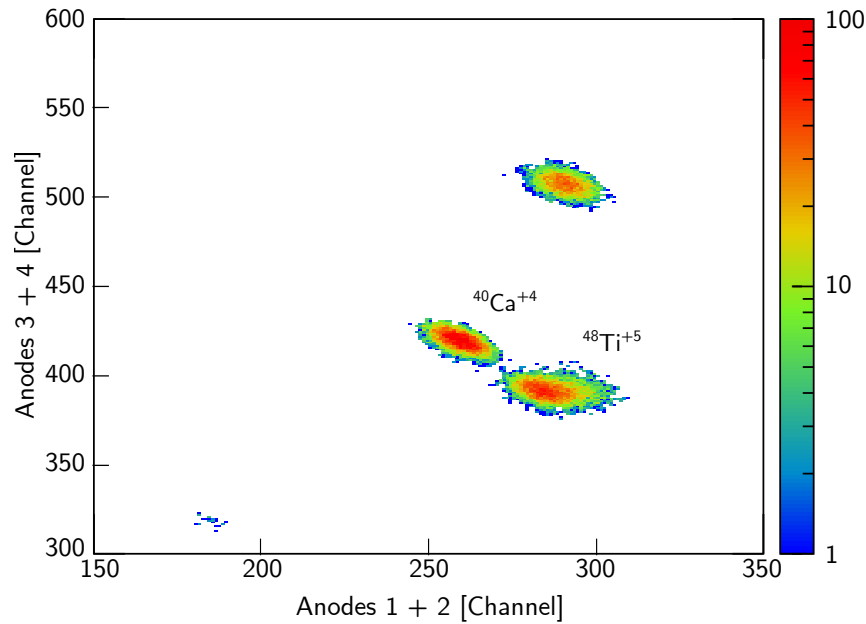
Figure 41: The combined spectra of a Ca and a Ti measurement. Both injected at the same total kinetic energy of E = 25.641 MeV. In this way the detector was calibrated and the correct component could be identified.

about 7% at the pre-calculated settings.

The used 4 anode ionization chamber from HVE has an active detector length of 330 mm, see [109], and was calibrated by injecting the stable ^{40}Ca beam. In this way it is possible to determine the position of ^{40}Ca isotopes, with the same energy than the later investigated ^{41}Ca isotopes, in all recorded spectra. To not damage the detector entrance foil, the beam intensity was reduced to $I < 100$ pA. The isobutane gas pressure was set to 13.5 mbar, which corresponds to a range of 265 mm, calculated with SRIM. A combined spectrum of the ^{40}Ca^{4+} and the ^{48}Ti^{5+} is shown in fig. 41. The counts measured on anode 1-2 are plotted against anode 3-4. Three clearly separated possible positions for ^{40}Ca^{4+} were found. To identify the correct beam component ^{48}Ti was injected with the same beam energy, by setting the terminal voltage to $U_{TV} = 5.128$ MV for the 4^+ charge state and $U_{TV} = 4.273$ MV for the 5^+ charge state. The latter one is even the better choice due to the much lower change for additional p/q interferences. By using ions with the same energy the measured peak position in a two dimensional histogram must lie on one diagonal line in a spectrum which includes all measured anodes and therefore the total energy deposition inside the detector. The difference in position depends on the nuclear charge Z and therefore on the specific energy loss.

After the stable ^{40}Ca^{4+} beam was successfully transported through the system up to the detector, the settings for ^{41}Ca for the HEM magnet, the HE ESA and the DSW magnet were calculated and set in the way described above. Also the LE magnet was slightly tuned from $I_{LE,^{40}Ca} = 134.227$ A (m = 97) to $I_{LE,^{41}Ca} = 134.970$ A (m = 98). Due to the relatively small bending radius of r = 400 mm the mass separation of the LE magnet is limited. This means that there was still a measurable current at the ACC Faraday cup, which could be cut by reducing the LE x-slit width to a total gap width of 4 mm. The offset Faraday cup, downstream the HEM magnet, was set to position 215 a.u. to measure the stable ^{40}Ca beam part. To measure both components ^{41}Ca and ^{40}Ca in a fast sequence, a so called bouncer system is installed to the LE magnet, as described in sec. 3.2. For this purpose, the vacuum chamber of the magnet is

Table 13: Determined system settings for the 6 MV Tandetron™ accelerator to measure ^{41}Ca at 5.8 MV terminal voltage. These settings were determined by optimizing the count rate of ^{41}Ca^{4+} inside the ionization chamber.

Section	Component	Value		Section	Component	Value	
	Cathode Volt.	6.99	kV		Q-Pole Focus	46.325	%
	Sputter Curr.	0.22	mA		Q-Pole Astig.	0.379	%
	Extraction	28	kV	HES	X-Steerer 1	3474	V
SO-110	Einzel Lens	14.74	kV		X-Steerer 2	2161	V
	Y-Steerer	180.84	V		Y-Steerer 1	2	V
	Ionizer	18	A		Y-Steerer 2	−2815	V
	Cs-Oven	105	°C	HEM	Magnet	103.398	A
	ESA	3948	V		Magnet	0.5688	T
	Magnet	134.140	A		X-Slits	open	
	Blanking St.	−48.65	V		ESA 1	77.398	kV
	X-Steerer 1	0	V		ESA 2	77.398	kV
BI	X-Steerer 2	−131.99	V	HEE	Y-Steerer	6249	V
	Y-Steerer 2	−50	V		Q-Pole Focus	31.404	%
	Einzel Lens	22.725	kV		Q-Pole Astig.	−6.581	%
	X-Slits	3	mm		Magnet	100.343	A
	Terminal	5.805	MV		Magnet	0.7414	T
	Stripper Gas	0.008	mbar	DSW	Q-Pole Focus	56.606	%
ACC	Q-snout	42.022	kV		Q-Pole Astig.	−1.893	%
	Q-Pole Focus	57.485	%	Detector	Pressure	15	mbar
	Q-Pole Astig.	−2.698	%				

electrically isolated from the beam tubes. As the magnet is a p/q filter, the required bouncer voltage for ^{41}Ca can be calculated by the following equation based on the energy and mass ratios of ^{41}Ca in comparison to ^{40}Ca.

$$p_1 = \sqrt{2\,m_1\,E_1} \overset{!}{=} \sqrt{2\,m_2\,E_2} = p_2$$

$$\Rightarrow E_2 = \frac{m_1}{m_2}\,E_1 = \frac{97}{98}\cdot 34.9974\,\text{keV} = 34.6429\,\text{keV}$$

Where m is the mass, p the momentum and E the energy of the first and the second element species, which is in this case ^{40}Ca and ^{41}Ca. The required bouncer voltage was calculated and set to $U_{\text{bouncer}} = -359.7$ V. First measurements with a ^{41}Ca C16 standard with a ratio of $R_{\text{lit.}}(^{41}\text{Ca}/^{40}\text{Ca}) = 1.155 \times 10^{-10}$, see Nishiizumi [92], in the detector resulted in a ratio of $R(^{41}\text{Ca}/^{40}\text{Ca}) = 3.5 \times 10^{-11}$ and a correction factor of $c_f = 3.3$. By measuring a blank sample it could be ascertained that the identified isotope is ^{41}Ca. The achievable blank value was $R(^{41}\text{Ca}/^{40}\text{Ca}) = 2 \times 10^{-13}$. To improve the results, in a first step all ion optical main components (bending magnets and ESAs) were traced with respect to the count rate inside the selected ROI in the MPA3 software, so called detector window counts. In a second cycle also the minor components were traced. By this the correction factor could be lowered to $c_f = 1.61$. In the step, the isobutane gas pressure was investigated to further improve the measurement. Therefore, a several measurements were performed with constant system settings but different gas pressures.

The pressure was set to 16 mbar and reduced in steps of 0.5 mbar down to 10 mbar. The best separation of ^{41}Ca and ^{41}K could be observed at 15 mbar, which corresponds to a calculated rage of 251 mm. At lower pressures, around 13 mbar, the ^{41}K component starts to move away from the intended diagonal line, which means that not the total energy is deposited inside the active detector volume anymore. By optimizing the detector gas pressure the correction factor was reduced to $c_f = 1.25$.

As mentioned before the LE x-slits are able to suppress the amount of ^{40}Ca right after the LE magnet. Therefore, multiple measurements with the 4 anode ionization chamber were performed to get a better understanding of the influence of these slit pair. Best results were achieved at 3 mm. Narrower slits would cut and reduce the desired beam intensity. The results obtained from a first batch measurement, after this optimization steps, are discussed in sec. 6.2.2. A complete list of the settings is given in tab. 13.

6.2.2 First Results for ^{41}Ca Standard and Blank Measurements

The first AMS batch measurement with ^{41}Ca in the course of this thesis, at the 6 MV Tandetron™ accelerator, was performed with two C16 standard samples and two blank samples, each one 13 times for 5 minutes, so called runs. During this relatively short measurement the correctness of the chosen tuning procedure as well as the resulting settings for the whole system could be verified.

The results of the first measurement are given in tab. 14. The table includes the total ^{41}Ca counts N(^{41}Ca) detected in the 4 anode HVE ionization chamber and the corresponding error based on the counting statistics, the mean ^{40}Ca current $\bar{I}$ measured at the offset Faraday cup, the determined ratio R(^{41}Ca/^{40}Ca) as well as the resulting correction factor c_f related to the given ratio of $R_{lit.}$(^{41}Ca/^{40}Ca) $= 1.155 \times 10^{-10}$. The individual ratios per run of the investigated samples is displayed in fig. 42. The resulting sample lifetime of about 60 min is absolutely sufficient to gain an adequate number of counts and therefore a low counting statistics error. In fig. 42 each ratio is given with the corresponding statistical error. The mean value for all 13 runs is indicated by the red line. For the measured blank samples the resulting ratios are raising over time, which should not be the case for a reliable sample. If this is the case for a blank sample there are initially two explanations. On the one hand, the high C16 standard could cause a so called memory effect over time and therefore effect higher count rates even for the blank samples. On the other hand, this could also be caused by the sample lifetime. Based on the results of additional measurements with a wide range of samples, blanks and expected ratios, the theory

Table 14: First ^{41}Ca batch measurement with two standard and two blank samples. Given are the literature ^{41}Ca/^{40}Ca ratio, see [92], the total ^{41}Ca counts N and the corresponding statistical error in percent, the mean ^{40}Ca current $\bar{I}$, the determined ^{41}Ca/^{40}Ca ratio R as well as the resulting correction factor c_f.

Sample	Lit. Ratio	N(^{41}Ca)	ΔN[%]	$\bar{I}$(^{40}Ca) [nA]	R(^{41}Ca/^{40}Ca)	c_f
C16-1	1.155×10^{-10}	50 209	0.45	98.62	$9.14(13) \times 10^{-11}$	1.26
C16-2	1.155×10^{-10}	47 671	0.46	93.87	$9.12(12) \times 10^{-11}$	1.27
Blank-1	—	72	11.79	60.86	$2.12(81) \times 10^{-13}$	
Blank-2	—	69	12.04	103.94	$1.19(44) \times 10^{-13}$	

(a) ^{41}Ca C16 standard sample 1

(b) ^{41}Ca C16 standard sample 2

(c) ^{41}Ca blank 1

(d) ^{41}Ca blank 2
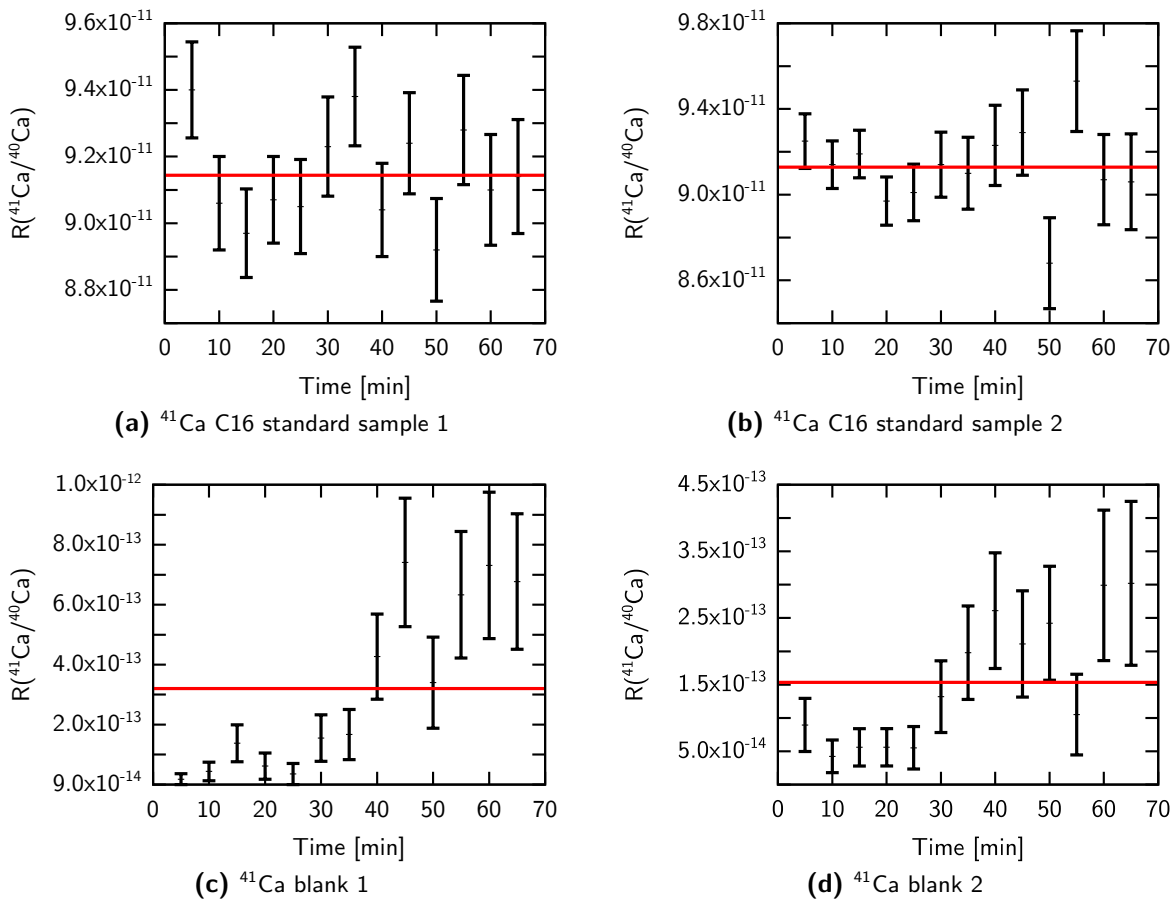
Figure 42: Displayed are the ^{41}Ca/^{40}Ca ratios, measured at the 6 MV Tandetron™ accelerator. Figure a) and b) show the measured C16 standard samples. Figure c) and d) the measured blank samples. The indicated errors are calculated from the counting statistics error of the individual ^{41}Ca counts. The red line indicated the resulting mean. The measured standard samples fit very well to the expected statistical fluctuation. The measured blank ratios on the other hand start increasing after about 30 min.

of a memory effect during a batch measurement could be rejected, which is further explained in sec. 6.3.1. Also the sample lifetime, at least during this measurement, seems not to be the reason for a raising ratio. In the case of an empty sputtered sample, the determined ratios are fluctuating and not continuously rising, as shown later in this thesis during the measurements of irradiated concrete samples, in fig. 46. Another possible reason for this result was found during the second batch run, and is based on the fact that the blank samples seems not to be ^{41}Ca free. An indication to contaminated blanks can also be seen in fig. 43, which shows the two dimensional histograms of a C16 standard sample and a blank sample measurement. In the case of the standard sample, the detected ^{41}Ca peak is much larger than the ^{41}K contamination. For this measurement, the separation factor was determined to $S_f = 2.65$, see fig. 44.

(a) ^{41}Ca Blank sample
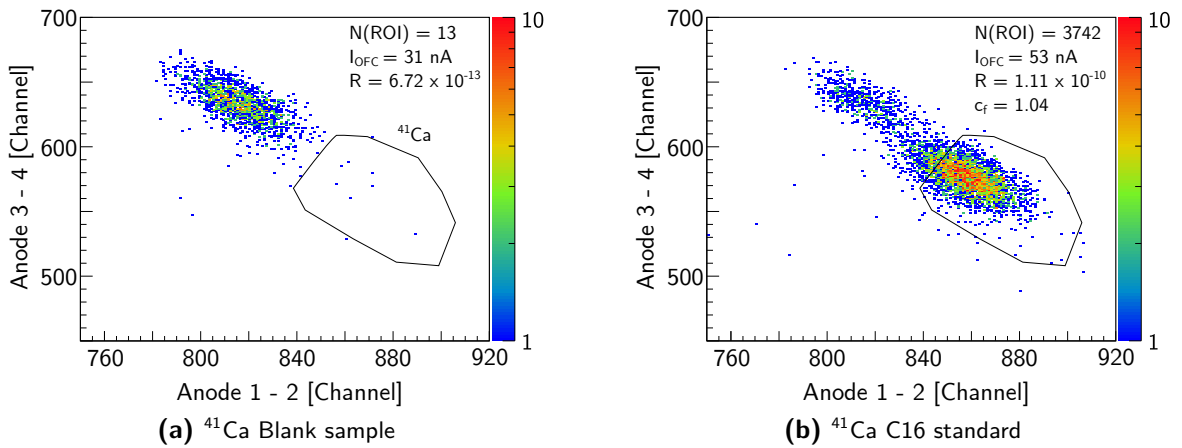
(b) ^{41}Ca C16 standard

Figure 43: Figure a) shows the result of a blank sample. Figure b) shows a measurement of a C16 standard, see Nishiizumi [92]. The amount of detectable ^{41}K is very similar, see sec. 6.2.2. The separation factor was determined to $S_f = 2.65$. The ^{41}K background is relatively low.
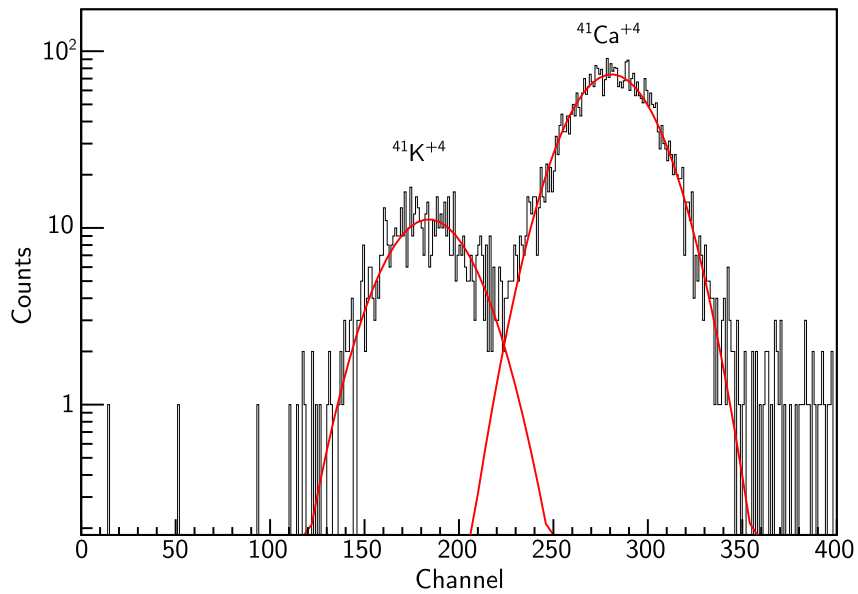
Figure 44: Projection of the ^{41}Ca and ^{41}K C16 standard sample measurement, compare fig. 43b, to the total energy diagonal. The determined separation factor is $S_f = 2.65$.

Second Batch Measurement of C16, C18 and C20 ^{41}Ca Standard Samples

In the course of a second batch measurement three different types of standard samples as well as blank samples were measured, to proof the determined correction factor and investigate a possible memory effect. This includes the C16 ($R_{\text{lit.}} = 1.155 \times 10^{-10}$), C18 ($R_{\text{lit.}} = 5.139 \times 10^{-12}$) and the C20 ($R_{\text{lit.}} = 5.884 \times 10^{-13}$) standard samples, see Nishiizumi [92]. Furthermore, the measurement should clarify if the separation is sufficient for lower ratios than $R(^{41}\text{Ca}/^{40}\text{Ca}) = 10^{-10}$ and if the background level is at about $R_{\text{Blk}} = 2 \times 10^{-13}$ as determined during the first measurement. The C20 standard is the lowest available standard and of the same order of magnitude than the blank level measured during the first batch. The beam was tuned with the same settings than before, see tab. 13, except of the bending- and analyzing magnets, which were retuned to achieve optimal conditions.

To further investigate the sample lifetime, each sample was measured for at least 19 runs, the measurement took about 16.5 h and resulted in 217 runs in total. Similar to fig. 42, the measured ratios and mean values for each first measured standard and blank sample are given in fig. 55. Based on the progression of the detected curve, it can be concluded that a well produced sample will last at least for 1 h, which is in good agreement with Rugel et al. [108]. Furthermore, a memory effect seems to be very unlikely due to the very constant results over this long time period and with respect to the measured range of more than two orders of magnitude between the lowest and the highest sample ratio.

The next question to be investigated during this second beam time was the blank level and the quality of the sample material according to the assumed contamination. For this purpose the resulting correction factors from all samples can be compared. The correction factor indicates the percentage loss of ^{41}Ca ions between the offset Faraday cup and the detector. This loss has to be the same for every measured ratio of the same isotope. The determined correction factors are $c_f = 1.27$ (C16), $c_f = 1.22$ (C18) and $c_f = 1.25$ (C20), which is in very good agreement with the first measurement. An exemplary run for each of the three standard samples as well as a blank sample is given in fig. 45. The given isotopic ratios and the corresponding correction factors only refer to this individual run. The detected contaminations of the blank sample is low and the corresponding ratio is $R = 2.39 \times 10^{-14}$. The individual values are given in tab. 15. The third C20 sample, was left out for all investigations due to the fact that the measured ratio was only stable for the first 6 out of 20 runs. After this, the sample seems to be empty. This conclusion results from the later real sample measurements, see sec. 6.3.2 which showed a similar behavior. A correction of the counted ^{41}Ca particles, of all later measurements, by the counts of the measured blank samples was renounced, to avoid a distortion of the data. This was concluded from the following consideration. Assuming a measured sample as a blank sample, a sample without ^{41}Ca, the detected counts inside the ^{41}Ca ROI would come from straggling or contamination of any kind. In this case for each measurement, the number of ^{41}Ca counts had to be corrected by this constant value. The so called blank correction. Following this approach, the correction factor c_f of the C20 sample would increase to $c_f = 1.46$, due to the reduced number of counts. For the other standard samples, C18 and C16, this very low correction would have only very little effect to the corresponding correction factors. Under this assumption the resulting correction factor of the C20 sample would differ by about 20% from the correction factors of the C16 and C18 samples. Therefore, it can be concluded, that the detected counts during the blank measurement are not from systematic errors or continuous background, but from a contamination of the blank material itself.

Another important value of an AMS measurement is the total transmission T through the accelerator system. This value can be estimated from the measured number of ^{41}Ca atoms of

(a) Blank sample

(b) C16 Standard sample

(c) C18 Standard sample

(d) C20 Standard sample
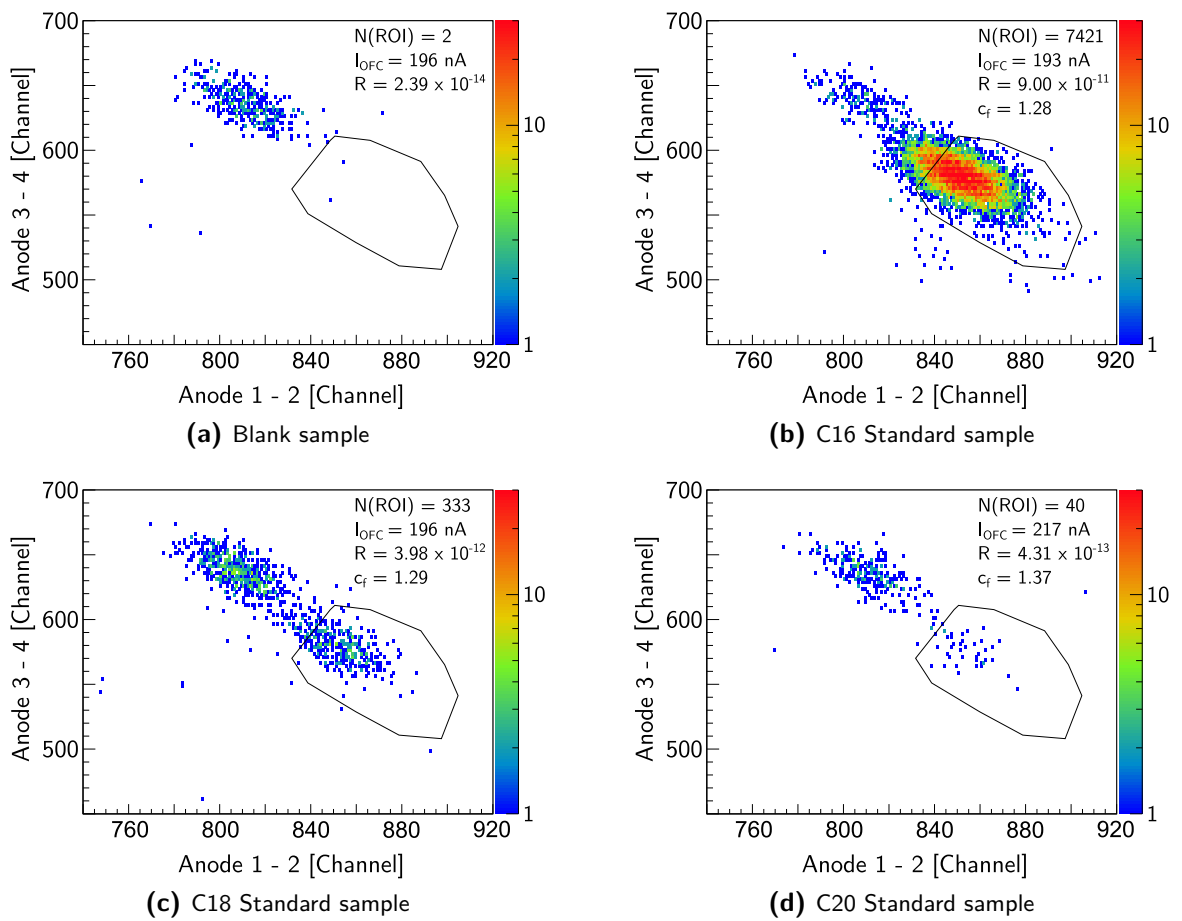
Figure 45: The figure shows four individual runs from the second batch measurement for ^{41}Ca, a C16, a C18, a C20 standard and a blank sample. All displayed runs took 300 sec and are plotted with the same intensity scale. The black polygons indicate the chosen ROIs. In figure a) the blank sample is displayed, which contains two counts inside the ROI. The following figures b), c) and d) show the standard samples C16, C18 and C20, respectively. All ^{41}Ca/^{40}Ca ratios, measured from standard samples, are in very good agreement with the given literature values, see tab. 15.

the standard samples. Each sample contained about m = 2 mg of CaF$_2$.[8] Based on the given literature ratio R(^{41}Ca/^{40}Ca) for each standard sample, the amount of ^{41}Ca from a single cathode can be calculated by eq. 6.1.

$$N(^{41}Ca)_{\text{lit.}} = \frac{R_{lit.} \cdot m \cdot N_A \cdot m_{^{41}Ca}}{m_{CaF_2} \cdot M_{Ca}} \qquad (6.1)$$

The equation includes the given ratio $R_{\text{lit.}}$, the mass of the sample m, the molecular mass of CaF$_2$(78),the mass of ^{41}Ca and the molar mass of calcium M_{Ca}. The fraction between the calculated and the measured amount of ^{41}Ca atoms is the transmission from the source up to the detector.

---

[8] private communication PD Dr. Erik Strub

Table 15: Results from the second ^{41}Ca AMS batch measurement at the 6 MV Tandetron™ accelerator. In total 11 samples where measured, each about 90 min. The bold values are the sum or mean values over a set of same samples, respectively. The sample C20 2, emphasized, was removed from further consideration due to heavy fluctuations of the beam current and the ^{41}Ca between the individual runs.

Sample	Lit. Ratio	N(^{41}Ca)	ΔN[%]	$\bar{I}(^{40}$Ca) [nA]	$\bar{R}(^{41}$Ca/^{40}Ca)	c_f
Blank-1	—	34	17.15	83.63	$5.00(294)\times10^{-14}$	—
Blank-2	—	32	17.68	83.16	$4.73(273)\times10^{-14}$	—
Blank-3	—	51	14.00	68.95	$9.09(418)\times10^{-14}$	—
Sum / Mean value		**117**	**9.25**	**78.58**	$\mathbf{6.27(328)\times10^{-14}}$	—
C16-1	1.155×10^{-10}	62 303	0.40	80.51	$9.03(11)\ \times10^{-11}$	1.28(2)
C16-2	1.155×10^{-10}	57 771	0.42	74.13	$9.10(13)\ \times10^{-11}$	1.27(2)
C16-3	1.155×10^{-10}	63 054	0.40	79.65	$9.25(11)\ \times10^{-11}$	1.25(2)
Sum / Mean value		**183 128**	**0.23**	**78.10**	$\mathbf{9.13(12)\ \times10^{-11}}$	**1.27(2)**
C18-1	5.139×10^{-12}	3162	1.78	90.42	$4.08(23)\ \times10^{-12}$	1.26(7)
C18-2	5.139×10^{-12}	3006	1.82	80.31	$4.37(23)\ \times10^{-12}$	1.18(6)
Sum / Mean value		**6168**	**1.27**	**85.37**	$\mathbf{4.23(23)\ \times10^{-12}}$	**1.22(7)**
C20-1	5.884×10^{-13}	389	5.07	97.53	$4.65(80)\ \times10^{-13}$	1.26(22)
C20-2	*5.884×10^{-13}*	*540*	*4.30*	*102.47*	*$6.15(86)\ \times10^{-13}$*	*0.96(14)*
C20-3	5.884×10^{-13}	377	5.15	93.56	$4.74(79)\ \times10^{-13}$	1.24(21)
Sum / Mean value		**766**	**3.61**	**95.55**	$\mathbf{4.70(79)\ \times10^{-13}}$	**1.25(21)**

$$T_{\text{tot.}} = \frac{N(^{41}Ca)_{\text{meas.}}}{N(^{41}Ca)_{\text{lit.}}}$$

The calculation was done separately for all three different standard samples C16, C18 and C20. The resulting mean transmission is $8.82(4) \times 10^{-5}$. This includes the sputter source extraction efficiency, the transmission through the accelerator, the abundance of the selected charge state after the high energy magnet and the detector efficiency and beam transport losses. The largest contribution comes from the ion source extraction efficiency, compare sec. 3.4.

6.3 ^{41}Ca Measurements of Irradiated Concrete Samples

A task becoming increasingly important is the dismantling of nuclear power plants used over the last decades. In this context, the question which part of the reactor has to be classified as high-level, intermediate-level, low-level waste or rubble arises. Therefore, it is important, especially with respect to the large amount of material, about 10^6 kg,[9] the biological shield is built of, to determine the local radioactive activities and classify the material. Up to now these values are estimated by the calculated neutron flux over time and the individual neutron capture cross section. Measurements were performed with nuclides like ^{60}Co ($T_{1/2} = 5.27$ a) or ^{137}Cs ($T_{1/2} = 30.08$ a)[10] with easy measurable γ-energies. The downside of these method is the comparable short half-life of both isotopes and therefore the increasing error for any estimation concerning the overall activity. Another method used to determine the radioactive activity is the liquid scintillation counting (LSC). But due to the low energy of the emitted Auger electrons, in the case of ^{41}Ca, the counting efficiency is limited to 25%, which is low in comparison to other investigations with LSC, see Hou [110]. Therefore the required measurement time is long (hours). Another problem during LSC measurements of ^{41}Ca are interfering signals of radionuclides as ^{55}Fe or ^{63}Ni, which can only be reduced by pre-treatments, see Hampe et al. [111]. In order to be more precise and classify the upcoming rubble faster and in a more sensitive way, ^{41}Ca was selected as a possible reference nuclide measurable with AMS techniques. For this purpose, test samples, made of heavy concrete with a composition comparable to a concrete used for biological shields, were produced to investigate the abundance distribution of ^{3}H, ^{14}C and ^{41}Ca for different total neutron irradiations. In the following section the sample production and preparation for ^{41}Ca is explained. Furthermore, the measurements and results are investigated in detail. This includes the sample lifetime and possible contaminations, the achievable background level as well as a measurement of a sample from a real biological shield. Since the sample lifetime and possible corrections, of the events detected by the ionization chamber, change the determined results, these topics are described before the measurement results are explained in detail.

6.3.1 Production of ^{41}Ca Sample Material

Under the leadership of PD Dr. Erik Strub from the Nuclear Chemistry department of the University of Cologne, a solid cuboid made of baryte concrete was produced, samples were extracted and AMS samples were prepared. Baryte concrete is a special kind of heavy concrete and further defined by DIN 25413-2 [112]. Heavy concrete in general is specified by a bulk density of more than $\rho = 2600$ kg/m^3, see [113, 114]. In the case of the biological shield of a nuclear power plant additional ingredients like baryte (Ba[SO$_4$]), hematite (Fe$_2$O$_3$), limonite (FeO(OH)) or other iron containing minerals were added to reach a bulk density of about $\rho = 4000$ kg/m^3.[11] A barium concentration of about $45 - 54\%$ is striven to call a heavy concrete mixture baryte concrete, see DIN 25413-1 [115]. These additives are necessary to provide the required shielding against neutrons and γ-rays. The resulting material samples come very close to original used reactor concrete, see the results of a XRF analysis provided by PD Dr. Erik Strub, tab. 24. This approach was chosen to circumvent problems concerning the sample extraction from real nuclear reactor biological shields and the production of reference samples which are not irradiated. To extract

---

[9] private communication PD Dr. Erik Strub
[10] National Nuclear Data Center, Retrieved February 20,2019 `www.nndc.bnl.gov`
[11] private communication PD Dr. Erik Strub, Prof. Dr. Alfred Dewald

samples from the cuboid, several core drillings were performed, each 1 cm in diameter. These cylinders were cut in half lengthwise. Each half was further cut into three discs. In this way six equivalent pieces were produced from each drilling. The sample nomenclature is described below.

1	**a**	**th**	**1**
irradiation group	piece	neutron class (thermal)	sample set

The first digit stands for the irradiation group, which corresponds to the irradiation time. Group 1 and 3 were irradiated for 30 s, group 2 for 300 s, group 4 for 1000 s and group 5 for 3000 s. The first character ranges from a to f and represents the part of the disc, cut from the core drilling described above. The second character group, th or ep, provides information about the neutron energy the samples were irradiated with, thermal or epithermal, respectively. The last digit stands for the sample set, three of which were produced to provide the possibility of measuring each sample three different times to receive more reliable results.

The sample cylinders were irradiated at the research reactor TRIGA Mark II in Mainz with a neutron flux of $\Phi = 1.7 \times 10^{12} \, \text{cm}^{-2}\,\text{s}^{-1}$, for the intended time span of 30 s to 3000 s. This dose is admittedly two to three orders of magnitude below the neutron density of $1 \times 10^{19} \, \text{cm}^{-2}$ reached during the long-time power operation of a real nuclear power plant, but sufficient for investigations with AMS techniques. In the course of this thesis, the expected amount of produced ^{41}Ca and the resulting ratios were calculated based on the amount of ^{40}Ca inside the used baryte concrete, see tab. 24. The production process of a nuclide N_B originating from a number of particles N_A, including the decay is described by the following equation.

$$\frac{\mathrm{d}N_B}{\mathrm{d}t} = \sigma \cdot \Phi \cdot N_A - \lambda \cdot N_B \tag{6.2}$$
$$\text{with: } \lambda = \frac{\ln(2)}{T_{1/2}}$$

Based on this first order linear inhomogeneous differential equation, the activity of the produced nuclide B can be calculated by integrating eq. 6.2 equation of the time t.

$$A(t) = \sigma \cdot \Phi \cdot N_A \left(1 - \exp\left(-\frac{\ln(2)\,t}{T_{1/2}} \right) \right) \tag{6.3}$$

The estimated activities, number of ^{41}Ca particles and ratios $R(^{41}\text{Ca}/^{40}\text{Ca})$ are calculated by equation eq. 6.3 and listed in tab. 16. The calculated numbers are based on the given neutron flux Φ, the amount of ^{40}Ca in 1 g concrete N_A, the irradiation time t and the half-life of ^{41}Ca $T_{1/2} = 9.94(15) \times 10^4$ a, see Jörg et al. [93]. The thermal neutron capture cross section for ^{40}Ca is $\sigma = 0.40(4)$ barn, see Cranston et al. [91]. Since the energy spectrum of the TRIGA reactor also includes epithermal and even faster neutrons, the neutron capture cross section was modified to fit to the energy spectrum described by Ziegner et al. [116]. The required cross section for the different energies are taken from the JANIS database of the Nuclear Energy Agency (NEA).[12] The resulting effective cross section is $\overline{\sigma} = 0.28$ barn.

The concrete samples were processed chemically into CaF_2 powder and mixed with pure silver with a ratio of 1:4. This was done by Raphael Margreiter from the Nuclear Chemistry department of the University of Cologne. A good description of the required chemical procedure is given by Nottoli et al. [117]. In this way in total $3 \times 37 = 111$ samples cathodes from irradiated material,

---

[12] Retrieved February 8, 2019 https://www.oecd-nea.org

Table 16: Estimations for ^{41}Ca production in heavy concrete irradiated with neutrons. The irradiation was done at the research reactor TRIGA Mark II in Mainz, with a neutron flux of $\Phi = 1.7 \times 10^{12}\,\mathrm{cm^{-2}\,s^{-1}}$. The underlining neutron capture cross section was modified from $\sigma = 0.40\,\mathrm{barn}$ to $\overline{\sigma} = 0.28\,\mathrm{barn}$, according to the neutron energy distribution emitted from the core of the TRIGA reactor, see Ziegner et al. [116], and the corresponding neutron capture cross section taken from the JANIS database of the Nuclear Energy Agency (NEA).[13]The calculation includes therefore also the contribution of epithermal neutrons.

Irradiation Time [sec]	A(^{41}Ca) [Bq/g]	calculated N(^{41}Ca)	$\overline{R}$ (^{41}Ca/^{40}Ca)
30	2.87(4) $\times 10^{-3}$	1.30(2)$\times 10^{+10}$	1.45(2)$\times 10^{-11}$
300	2.87(4) $\times 10^{-2}$	1.30(2)$\times 10^{+11}$	1.45(2)$\times 10^{-10}$
1000	9.57(18)$\times 10^{-2}$	4.33(6)$\times 10^{+11}$	4.83(7)$\times 10^{-10}$
3000	2.87(4) $\times 10^{-1}$	1.30(2)$\times 10^{+12}$	1.45(2)$\times 10^{-9}$
30 000	2.87(4)	1.30(2)$\times 10^{+13}$	1.45(2)$\times 10^{-8}$

10 blank, 8 C16 and 8 C20 standard samples as well as 3 cathodes from not irradiated concrete were produced.

6.3.2 Sample Lifetime

The sample lifetime was already investigated during the first measurements of ^{41}Ca standard samples, but during the investigation of the irradiated concrete samples, the lifetime was proven to be much shorter than expected before, see fig. 46. The figure shows the measured ^{41}Ca/^{40}Ca ratio, the ^{40}Ca current measured at the offset Faraday cup and the total ^{41}Ca counts for each run for four different samples. All indicated samples are C16 standard samples made from the same material with the same addition of silver. However, the older samples, 1a and 2a, show a much more stable behavior over the whole measurement time of 100 min. The later produced samples, 1b and 2b, are only stable for about 30 min, which corresponds to 6 measurement runs. After this time span the ^{40}Ca current as well as the amount of detected ^{41}Ca atoms decreased rapidly and the resulting ratio starts fluctuating, with an up to 100% higher ratio compared to the mean value of the first six runs. Further investigations revealed that the samples were measured down to the stainless steel pin at the very end of the cathode. This pin is inserted during the sample preparation to seal the cathode on the backside and is made of pure stainless steal and should therefore not contain any ^{41}Ca. The measured current as well as the detected counts could be extracted material from inner walls of the cathode, which becomes a more and more inhomogeneous process. The same behavior could be observed for the very majority of samples in both batch runs. An possible explanation is, that the later produced samples are pressed with less material or less pressure, which could result in losses inside the source. Therefore, the number of runs, taken into account for the analysis, was reduced to six. Even with this reduced number of runs, the amount of detectable counts, accumulated over 30 min (six runs) lead to a statistical error below 3% for each concrete sample measured.

---

[13] Retrieved February 8, 2019 https://www.oecd-nea.org
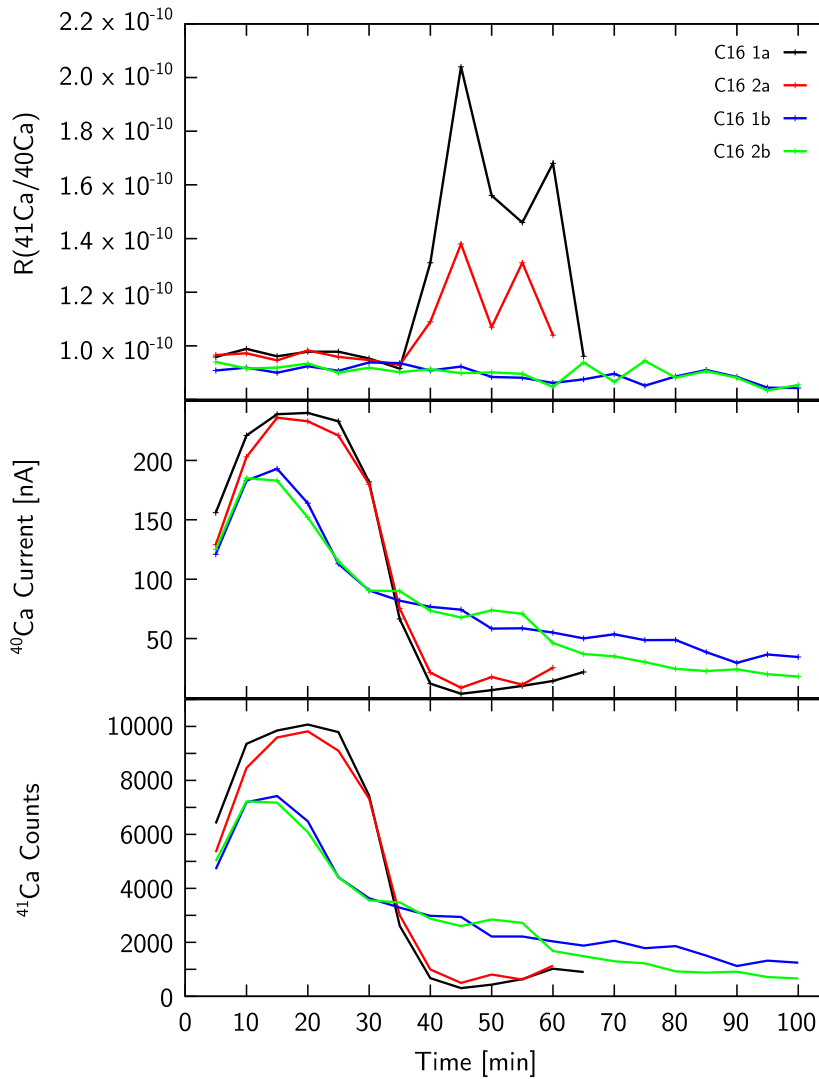
Figure 46: This plot shows the sample lifetime of two sets of C16 ^{41}Ca standard samples. Each sample was produced from the same C16 material and mixed with the same amount of pure silver. Nevertheless, the measured ^{40}Ca current as well as the detected ^{41}Ca counts results in a different curve progression. The new samples start fluctuating to higher ratios after about 30 min. This could be traced back to the fact that the samples were sputtered empty.

6.3.3 Potassium Correction

During all batch runs with concrete samples and new produced standard samples, a considerably high contamination of ^{41}K was detected. An example is given in fig. 47. Results from a single run of a C20 standard sample, produced for the first test measurement is shown in fig. 47a. The total number of counts inside the ^{41}Ca ROI is $N(R) = 37$ at a mean current of $\bar{I}_{OFC} = 185\,\mathrm{nA}$ determined at the offset Faraday cup, which results in a ratio of $R = 4.66 \times 10^{-13}$ and a correction factor of $c_f = 1.26$. This result was reproducible and fits to the determined correction factors of similar measurements with C16 and C18 standard samples, see tab. 15. The result of a recent C20 standard sample, available for the concrete sample batch measurements, is displayed in fig. 47b. In this case the number of detected ^{41}Ca counts is $N(R) = 231$, within the same time span, at a comparable mean current of $\bar{I}_{OFC} = 145\,\mathrm{nA}$. This results in a ratio of

(a) ^{41}Ca C20 standard sample first production

(b) ^{41}Ca C20 standard sample later production
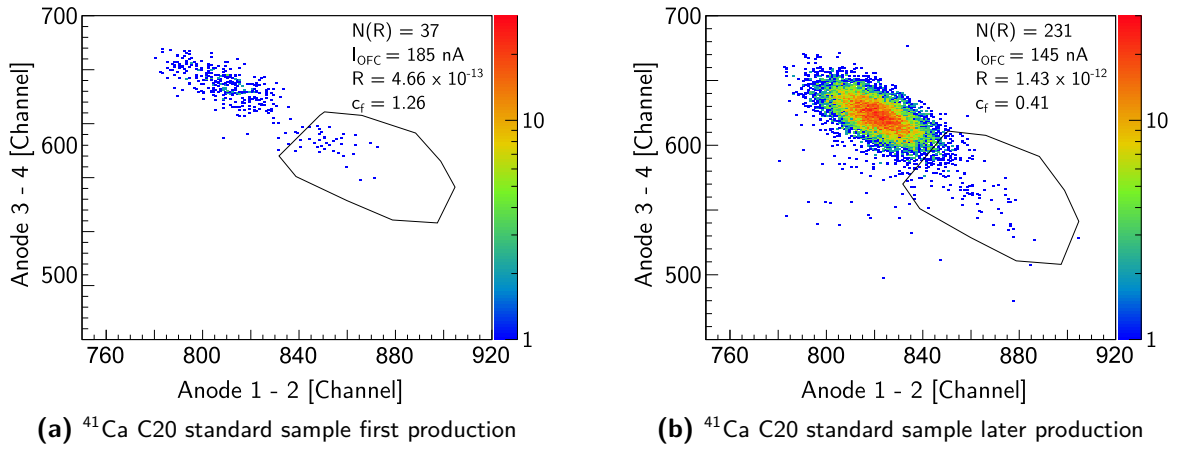
Figure 47: This figure shows two different ^{41}Ca C20 standard samples, measured at the Tandetron™ accelerator with comparable settings. The results shown in figure a) are from a sample used during the first test measurements, see tab. 15. The determined correction factors for all measured standard samples, with different ratios, is equivalent within the measurement uncertainty. Figure b) clearly shows a much larger contamination with ^{41}K than before, which results in a correction factor smaller 1.

$R(^{41}Ca/^{40}Ca) = 1.43 \times 10^{-12}$ and a correction factor of $c_f = 0.41$. The contamination inside the set ROI result in a significantly too low correction factor. Both samples were made from the same standard material in combination with the same amount of silver, taken from the same supply.

To reduce the amount of detected ^{41}K inside the ^{41}Ca ROI, the size of the ROI could be reduced for all measurement. The downside of this approach is a loss of ^{41}Ca events. A different approach is the introduction of a K correction factor c_K. Hereinafter, the capabilities of a potassium correction and the associated difficulties should be discussed. In eq. 6.4 the general approach to calculate the ratio R for a ^{41}Ca standard sample is given, including a potassium correction term.

$$R_{Std} = c_f \cdot \left(\frac{N_{Std}(^{41}Ca) - \frac{N_{Std}(K)}{c_K}}{N_{Std}(^{40}Ca)} \right) \tag{6.4}$$

Where $N_{Std}(^{41}Ca)$ and $N_{Std}(^{40}Ca)$ are the measured ^{41}Ca and ^{40}Ca events at the ionization chamber and at the offset Faraday cup, respectively. Inside a second ROI the number of potassium events was counted, $N_{Std}(K)$ for the standard sample. The correction factor is c_f and the new factor c_K describe the ratio between the total K counts and the counts wrongly detected inside the set ^{41}Ca ROI. Since the correction factor c_f depends on the ratio of ^{41}Ca/^{40}Ca, which has to be corrected by the factor c_K, this equation has two unknowns. Therefore, both indicated measurements A and B were taken into account and eq. 6.5 can be inferred under the assumption, that the ^{41}Ca ROI of sample A is potassium free.

$$\frac{N_{Std,A}(^{41}Ca)}{N_{Std,A}(^{40}Ca)} = \frac{N_{Std,B}(^{41}Ca) - \frac{N_{Std,B}(K)}{c_K}}{N_{Std,B}(^{40}Ca)} \tag{6.5}$$

$$c_K = \frac{N_{Std,B}(K)}{N_{Std,B}(^{41}Ca) - \frac{N_{Std,A}(^{41}Ca) \cdot N_{Sdt,B}(^{40}Ca)}{N_{Std,A}(^{40}Ca)}}$$

The resulting equation for the potassium correction c_K depends on the detected events N for ^{41}Ca and ^{40}Ca for measurement A and B as well as the counts for ^{41}K of measurement B. According to the given numbers in fig. 47 and a measurement time of 275 s each, the correction factor $c_K = 59.48$. Since the number of counts inside the ^{41}Ca ROI becomes negative, after subtracting the supposed potassium background, in many cases, the background seems to be overestimated by this large correction factor. Therefore, no potassium correction was applied to the later given data. To determine a better correction factor, a clear blank sample should be measured. In this way only counts from scattered potassium would be counted inside the ^{41}Ca ROI.

6.3.4 Results of Concrete Samples Irradiated with Neutrons

The following section describes the results of the three ^{41}Ca AMS batch measurements of all 84 concrete samples irradiated with the full neutron spectrum ejected from the TRIGA reactor core. The measurement was performed within two different beam times. In this way possible sources of error due to beam tuning, detector settings or the set ^{41}Ca ROI should be minimized by rerunning everything from scratch for the second beam time.

The results of all three batch measurements, including the statistical ratios, are given in tab. 17. The table includes the determined weighted mean ratios for all irradiated concrete samples sorted by their irradiation time in seconds, the ratios determined from the C16 and C20 standard samples and the blank as well as the untreated samples. Furthermore, the corresponding correction factors c_f are given. The results obtained from samples irradiated for 30 seconds are split into two groups according to the ID starting with a 1 or a 3, which corresponds to two individual irradiation runs.

The given ratios are calculated according eq. 4.1 and corrected by the corresponding correction factor c_f. For each batch measurement a separate correction factor was determined based on the C16 standard, which is required due to the changes in beam focusing. As an example see fig. 48, showing a single run of sample 1bth2 and 5bth2. The determined ratio of the C20 standard, also measured in each batch, is too high and not usable to calculate the correction factor. As explained

Table 17: ^{41}Ca ratios determined from all three batch measurements of irradiated concrete samples. The measured ratios are averaged over all samples of the same batch and with the same irradiation time the samples were produced with. The measured C16 and C20 standard samples as well as the blanks and the untreated samples are given in the lower part. The calculated values correspond to sec. 6.3.1. The given correction factors c_f are determined by the C16 measurement and applied to each measured concrete sample.

Sample	$\overline{R}_c$ (Batch 1)	$\overline{R}_c$ (Batch 2)	$\overline{R}_c$ (Batch 3)	R Calculated
30 (ID 1)	2.35(25) $\times 10^{-11}$	1.64(10)$\times 10^{-11}$	1.59(13) $\times 10^{-11}$	1.45(2)$\times 10^{-11}$
30 (ID 3)	2.39(20) $\times 10^{-11}$	1.84(12)$\times 10^{-11}$	1.83(15) $\times 10^{-11}$	1.45(2)$\times 10^{-11}$
300	1.53(3) $\times 10^{-10}$	1.46(3) $\times 10^{-10}$	1.49(4) $\times 10^{-10}$	1.45(2)$\times 10^{-10}$
1000	4.85(5) $\times 10^{-10}$	4.69(4) $\times 10^{-10}$	4.75(6) $\times 10^{-10}$	4.83(7)$\times 10^{-10}$
3000	1.48(1) $\times 10^{-9}$	1.44(1) $\times 10^{-9}$	1.45(1) $\times 10^{-9}$	1.45(2)$\times 10^{-9}$
Untreated	—	1.45(31)$\times 10^{-12}$	—	
C16	9.80(15) $\times 10^{-11}$	1.03(1) $\times 10^{-10}$	1.04(2) $\times 10^{-10}$	
C20	8.16(225)$\times 10^{-13}$	1.02(14)$\times 10^{-12}$	1.08(21) $\times 10^{-12}$	
Blank	9.69(397)$\times 10^{-13}$	3.75(82)$\times 10^{-13}$	6.70(681)$\times 10^{-13}$	
c_f	1.18	1.12	1.11	

(a) Sample 1bth2, run 2   **(b)** Sample 5bth2, run 2
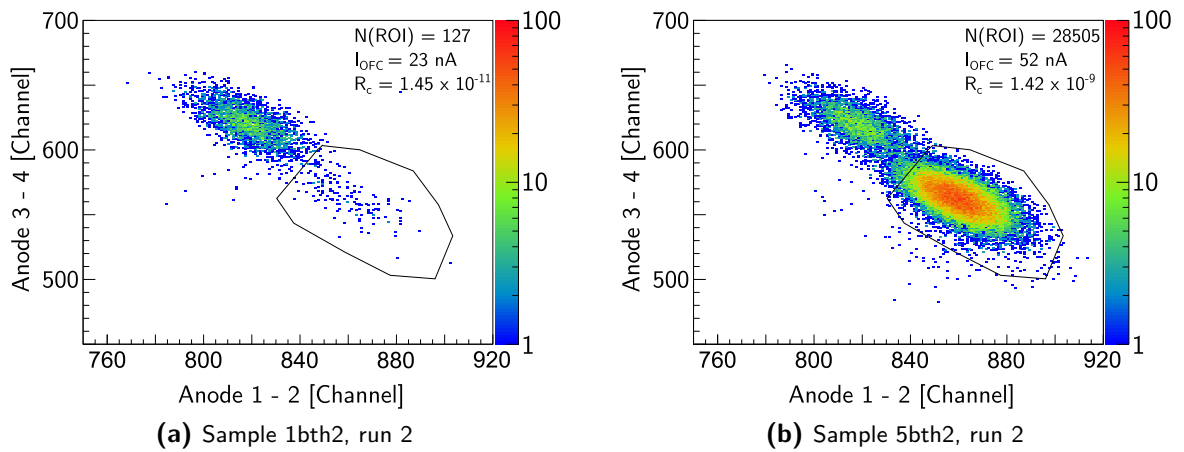
Figure 48: Plot a) shows the run 2 of the irradiated sample 1bth2 and plot b) shows run 2 of sample 5bth2. The measured mean current for ^{40}Ca, the detected number of counts inside the ROI, N(ROI) as well as the corrected ratio R_c are given.

above, this problem can be traced back to a potassium contamination. In the case of the blank samples, the problem of the unknown quality of the material and the potassium background are combined, both described in this chapter, which makes a blank correction impossible.

The individual results of the second batch measurement, for each sample, are listed in tab. 18. The results of the first and third set of samples are listed in the appendix, see tab. 25 and tab. 26, respectively. The tables include the irradiation time, the sample ID, the numbers of detected ^{41}Ca atoms N(^{41}Ca), the mean ^{40}Ca current measured at the offset Faraday cup $\bar{I}(^{40}$Ca$)$ [nA] as well as the resulting mean ratio $\bar{R}_c$. The achieved mean currents are comparable to the currents measured during the first test measurements, see tab. 15. The increase, from the first batch run
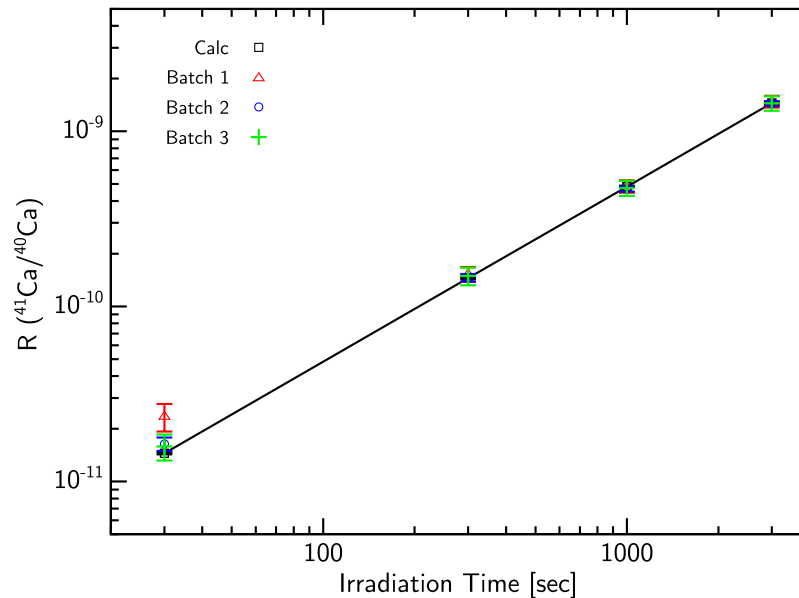
Figure 49: The figure shows the linearity of the irradiation time and the measured values as well as the calculated values of ^{41}Ca/^{40}Ca ratios in heavy concrete irradiated by thermal neutrons with a flux of $\Phi = 1.7 \times 10^{12}$ cm^{-2} s^{-1}. The corresponding values are given in tab. 16.
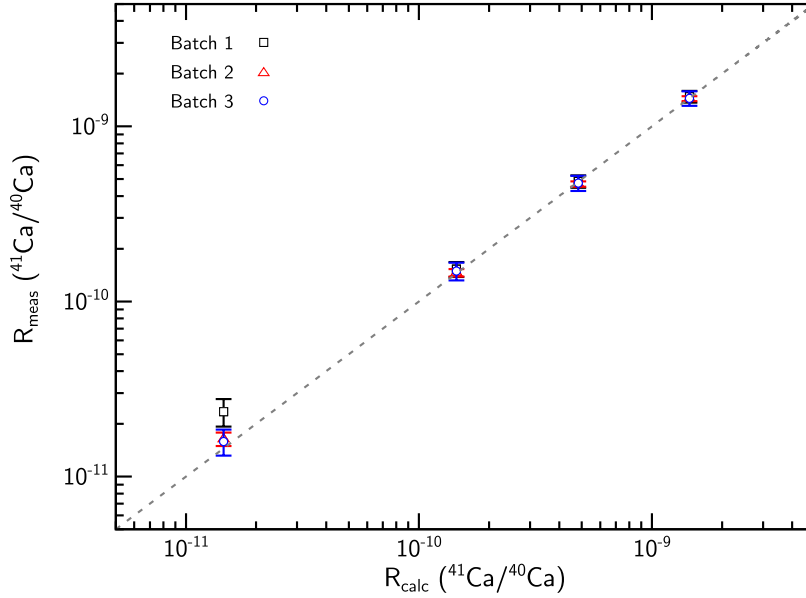
Figure 50: The figure shows a comparison between the estimated and the measured values of ^{41}Ca/^{40}Ca ratios in heavy concrete irradiated by thermal neutrons with a flux of $\Phi = 1.7 \times 10^{12}\,\mathrm{cm}^{-2}\,\mathrm{s}^{-1}$. The measurement is consistent within a range of three orders of magnitude. The corresponding values are given in tab. 16.

to the second and third, was achieved by increasing the Cs-oven temperature by $2\,^\circ$C.

During the second batch measurement, also three untreated samples were investigated. These samples were made from the same concrete as the other irradiated samples, but were not irradiated with neutrons. In this way possible contaminations inside the material and during the sample preparation can be detected. The determined ratio is $\overline{R}_c = 1.45 \times 10^{-12}$ and therefore one order of magnitude lower than the samples irradiated for 30 s, but comparable to the ratios of the C20 standard samples. Nevertheless, the same amount of potassium contamination was detected, compared to the former used standard and blank samples from the same sample preparation. The investigation should be repeated if the K was minimized, to get more reliable results and a more precise background level. According to the long half-life of ^{41}Ca in comparison to the production time, the last term of eq. 6.2, $\lambda\,N_B$, approaches zero.

$$\mathrm{d}N(^{41}Ca) = \sigma \cdot \Phi \cdot N(^{40}Ca)\,\mathrm{d}t \tag{6.6}$$

The resulting linear expression describes the number of ^{41}Ca ions produced after the time t. It depends on the neutron capture cross section σ, the neuron flux Φ and the number of available ^{40}Ca ions. In fig. 49, this relation is confirmed by plotting the irradiation time t against the calculated and the measured isotopic ratios. The discrepancy between the measured data sets is very little. The neutron capture cross section was reduced as explained in sec. 6.3.1, to a mean cross section of $\overline{\sigma} = 0.28$ barn. The expected ratios, based on this corrected cross section, are also displayed in fig. 49. The corresponding solid black line, fits to the measured values within only a few percent. Comparable to the measurements performed by Nishiizumi [92], the calculated and the measured ratios are plotted against each other, see fig. 50. The resulting linearity over three orders of magnitude demonstrated the precision of the measurement and the precision of the adapted mean neutron capture cross section.

Table 18: Results of the second ^{41}Ca measurement at the 6 MV Tandetron™ accelerator of concrete samples irradiated with neutrons. The measurements are sorted by the sample ID and the corresponding irradiation time. The displayed sum values for the detected counts N, the measured current $\bar{\text{I}}$ and the corresponding corrected ratio $\bar{\text{R}}_c$ are calculated as described in sec. 4.4. The measurement time for each sample was about 26 min.

Irrad. Time [sec]	Sample ID	N(^{41}Ca)	$\bar{\text{I}}$(^{40}Ca) [nA]	$\bar{\text{R}}_c$(^{41}Ca/^{40}Ca)
30	1bth2	1421	29.82	$1.24(10)\times10^{-11}$
30	1cth2	2180	29.29	$1.94(12)\times10^{-11}$
30	1dth2	5463	84.82	$1.68(7)\ \times10^{-11}$
30	1fth2	1367	20.98	$1.69(12)\times10^{-11}$
300	2ath2	10 089	17.15	$1.53(4)\ \times10^{-10}$
300	2bth2	13 982	28.57	$1.41(3)\ \times10^{-10}$
300	2cth2	20 426	41.42	$1.43(2)\ \times10^{-10}$
300	2dth2	14 080	27.98	$1.45(3)\ \times10^{-10}$
300	2eth2	10 545	20.82	$1.46(4)\ \times10^{-10}$
300	2fth2	16 082	31.57	$1.47(3)\ \times10^{-10}$
30	3ath2	1561	27.77	$1.72(12)\times10^{-11}$
30	3bth2	1906	32.61	$1.69(13)\times10^{-11}$
30	3cth2	1987	34.43	$1.67(12)\times10^{-11}$
30	3dth2	1952	37.75	$1.49(10)\times10^{-11}$
30	3eth2	2334	24.43	$2.76(13)\times10^{-11}$
30	3fth2	2214	37.75	$1.70(10)\times10^{-11}$
1000	4ath2	81 311	51.11	$4.60(4)\ \times10^{-10}$
1000	4bth2	68 726	42.54	$4.67(6)\ \times10^{-10}$
1000	4cth2	79 090	48.78	$4.68(4)\ \times10^{-10}$
1000	4dth2	107 367	65.85	$4.71(4)\ \times10^{-10}$
1000	4eth2	62 981	38.27	$4.76(5)\ \times10^{-10}$
1000	4fth2	56 614	34.74	$4.71(5)\ \times10^{-10}$
3000	5ath2	109 622	21.32	$1.49(1)\ \times10^{-9}$
3000	5bth2	323 168	64.54	$1.45(1)\ \times10^{-9}$
3000	5cth2	165 235	33.60	$1.42(1)\ \times10^{-9}$
3000	5dth2	205 736	41.68	$1.43(1)\ \times10^{-9}$
3000	5eth2	243 452	49.52	$1.42(1)\ \times10^{-9}$
3000	5fth2	215 210	43.32	$1.44(1)\ \times10^{-9}$
	Untreated	611	40.29	$1.45(31)\times10^{-12}$
	Blank	813	126.35	$3.75(82)\times10^{-13}$
	Std C16	114 857	129.24	$1.03(1)\ \times10^{-10}$
	Std C20	1091	124.71	$1.02(14)\times10^{-12}$

Table 19: Estimated detection limits for ^{41}Ca at the 6 MV Tandetron™ accelerator. The calculation is based on eq. 6.7.

Batch	$N_{^{41}Ca,ROI}(K)$	R_{Blk}	R_L
1	309(18)	9.69(397)$\times 10^{-13}$	1.28(53) $\times 10^{-14}$
2	203(14)	3.75(92) $\times 10^{-13}$	6.12(152)$\times 10^{-14}$
3	195(14)	6.70(680)$\times 10^{-13}$	1.12(114)$\times 10^{-13}$

Based on the resulting ratios in comparison with the calculated values and with respect to the determined low correction factor, a detection limit R_L can be estimated. The estimation is based on statistical calculations of Currie et al. [118]. The detection limit can be defined by the following equation.

$$R_L = 2.33 \cdot \frac{R_{Blk}}{\sqrt{N_{^{41}Ca,ROI}(K)}} \tag{6.7}$$

Where R_{Blk} is the measured ratio for a blank sample and $N_{^{41}Ca,ROI}(K)$ the number of counts inside the ^{41}Ca ROI during this measurement. The resulting detection limits for all three batch measurements with irradiated samples is given in tab. 19.

6.3.5 Results of Concrete Samples Irradiated with Epithermal Neutrons

Beside the samples irradiated with thermal neutrons, also nine samples from each set were equipped with a 1 mm cadmium shield before irradiated with neutrons. In this way the sample activation induced by epithermal neutrons should be investigated, since all thermal neutrons are absorbed within this additional shielding. The results of the measurements are given in tab. 21.

Table 20: Estimations for ^{41}Ca production in heavy concrete irradiated with epithermal neutrons. The irradiation was done at the research reactor TRIGA Mark II in Mainz, with a neutron flux of $\Phi = 1.7 \times 10^{12}$ cm^{-2} s^{-1}. The underlining neutron capture cross section was modified from $\sigma = 0.40$ barn to $\overline{\sigma} = 0.15$ barn, according to the neutron energy distribution, in the epithermal range, emitted from the core of the TRIGA reactor, see Ziegner et al. [116], and the corresponding neutron capture cross section taken from the JANIS database of the Nuclear Energy Agency (NEA).[14]

Irradiation Time [sec]	A(^{41}Ca) [Bq]	calculated N(^{41}Ca)	$\overline{R}$ (^{41}Ca/^{40}Ca)
30	1.57(4) $\times 10^{-3}$	7.12(18)$\times 10^{+9}$	7.94(20)$\times 10^{-12}$
300	1.57(4) $\times 10^{-2}$	7.12(18)$\times 10^{+10}$	7.94(20)$\times 10^{-11}$
1000	5.24(14)$\times 10^{-2}$	2.37(6) $\times 10^{+11}$	2.65(7) $\times 10^{-10}$
3000	1.57(4) $\times 10^{-1}$	7.12(18)$\times 10^{+11}$	7.94(20)$\times 10^{-10}$
30 000	1.57(4)	7.12(18)$\times 10^{+12}$	7.94(20)$\times 10^{-9}$

[14] Retrieved February 8, 2019 https://www.oecd-nea.org

Table 21: ^{41}Ca ratios determined from all three batch measurements of concrete samples irradiated with epithermal neutrons. The measured ratios are averaged over all samples of the same batch and with the same irradiation time the samples were produced with. The measured C16 and C20 standard sample are given in the lower part. The calculated values correspond to sec. 6.3.1. The given correction factors c_f are determined by the C16 measurement and applied to each measured concrete sample.

Prod. Time [sec]	$\overline{R}_c$ (Batch 1)	$\overline{R}_c$ (Batch 2)	$\overline{R}_c$ (Batch 3)	R Calculated
30 (ID 1)	$9.37(220)\times10^{-12}$	$5.84(76)\times10^{-12}$	$5.92(137)\times10^{-12}$	$7.94(20)\times10^{-12}$
300	$1.11(22)\ \times10^{-11}$	$6.54(76)\times10^{-12}$	$1.11(20)\ \times10^{-11}$	$7.94(20)\times10^{-11}$
C16	$1.52(26)\ \times10^{-11}$	$1.06(11)\times10^{-11}$	$1.04(9)\ \ \times10^{-10}$	
C20	$8.16(291)\times10^{-13}$	$1.02(16)\times10^{-12}$	$1.08(10)\ \times10^{-12}$	
c_f	1.18	1.12	1.11	

Compared to the results obtained from the concrete samples irradiated with the whole spectrum of neutrons available, this results are less meaningful in a number of ways with regard to the intended material from a biological shield. On the one hand, the shielding concrete is not surrounded by any moderating material, on this account the thermal neutrons have a much stronger influence to te overall production of ^{41}Ca ions. On the other hand, the used shielding seems to be less homogeneous than expected. This assumption arose from the much higher deviation of the measured ratios between runs of the same sample, in comparison to the samples irradiated with thermal neutrons.

6.3.6 First Results from Concrete Samples of a Biological Shield

In this last section of the investigation concerning ^{41}Ca in concrete samples, samples from a real biological shield were measured. First of all, a XRF analysis of the material was conducted by PD Dr. Erik Strub. In this way the amount of CaO was determined to 6.97%, see tab. 24 column Sample. Based on this number and the assumption of a similar neutron flux achieved at the TRIGA reactor, of $\Phi = 1.7 \times 10^{12}\,\text{cm}^{-2}\,\text{s}^{-1}$, the activity after 10 years of operation was calculated to A = 44.4 kBq/g and a corresponding isotopic ratio of R(^{41}Ca/^{40}Ca) = 2.79×10^{-4}. The legal limit for solid materials to be released free of radioactive material containing only ^{41}Ca is 20 Bq/g.[15]

Since samples with isotopic ratios that high would contaminate the whole system, it was decided to dilute the material with untreated concrete material by the factor of 1:1000. During the sample preparation, conducted by Raphael Margreiter, a dilution of 0.00293 g of sample material to 2.93151 g of untreated concrete could be achieved, which results in a factor of 1:1000.52. In total three sample were produced from the same concrete material. A single run of a biological shield sample measurement is given in fig. 51b and the C16 standard measured during the same batch is displayed in fig. 51a. The mean correction factor over all four measured C16 standard samples was calculated to $c_f = 1.09$ and applied to the measurements. In tab. 22 the results for this batch measurement are summarized. According to the dilution of the sample material, the measured ratios and the corrected ratios are given. The mean ratio over all three concrete

[15] Verordnung über den Schutz vor Schäden durch ionisierende Strahlen (Strahlenschutzverordnung - StrlSchV), Annex III, Table 1, column 5

Table 22: First results of biological shield concrete samples measured at the 6 MV Tandetron™ accelerator. The three samples are made from the same material, which was diluted by three orders of magnitude to prevent possible system contaminations and memory effects. Given are the number of ^{41}Ca counts, the mean ^{40}Ca beam current and the determined ratio. In the last column, $\overline{R}_c$(dil. corr.), the ratios are including the dilution factor.

Sample	N(^{41}Ca)	$\overline{I}$(^{40}Ca) [nA]	$\overline{R}_c$(meas.)	$\overline{R}_c$(dil. corr.)
1	602	48.52	3.92(48) $\times 10^{-12}$	3.92(48)$\times 10^{-9}$
2	514	51.20	3.17(41) $\times 10^{-12}$	3.17(41)$\times 10^{-9}$
3	1312	34.39	1.21(13) $\times 10^{-11}$	1.21(13)$\times 10^{-8}$
Blank	255	101.69	1.44(70) $\times 10^{-13}$	
Std C16	130 092	104.07	1.06(2) $\times 10^{-10}$	
Std C20	743	111.29	6.44(132)$\times 10^{-13}$	

samples is $\overline{R}_c = 6.39(74) \times 10^{-9}$, which corresponds to a radioactive activity of 1.02 Bq/g.

Due to a lack of available informations concerning the origin of the sample and the circumstance of the irradiation, possible explanations of the discrepancy are discussed hereinafter. Based on eq. 6.6 and the proven linearity shown in fig. 49 differences of five orders of magnitude between the calculated and the measured isotopic ratios may be caused in two ways. If the concrete was extracted at the outer surface of the biological shield, the neutron flux would be reduced by several orders of magnitude, see Sahadath et al. [119], which would reduce the resulting ratio by the same order. The other possible explanation is based on the neutron energy. If the investigated biological shield is part of a fast neutron reactor, so called fast breeder, the neutron energy would be in the order of 5 MeV and the corresponding capture cross section at only $\sigma = 1$ mbarn. In combination with a neutron flux of $\Phi = 2 \times 10^{10}$ cm^{-2} s^{-1}, the measured ratio can be explained.

(a) C16 Standard

(b) Biological Shield Conrete
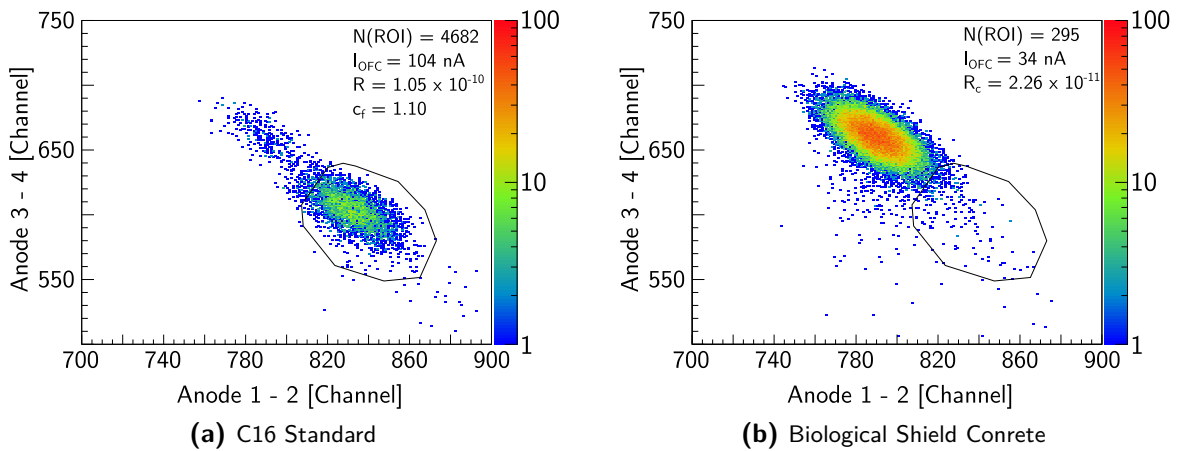
Figure 51: Result of the first concrete sample from a biological shield. The measured ratio is $R_c = 2.26 \times 10^{-11}$.

Chapter 7

Conclusion and Outlook

Conclusion

In the course of this thesis four main topics concerning the improvement of the measurement capabilities at the Cologne 10 MV FN-Tandem accelerator as well as the Cologne 6 MV Tandetron™ accelerator, the data acquisition and data processing, measurements of ^{58}Fe and ^{58}Ni and investigations concerning ^{41}Ca as a possible new reference nuclide for the topic of nuclear waste management were examined.

In the context of improvements concerning the experimental setup, the new 135° gas-filled magnet was put into operation. This includes the installation of three new power supplies and their integration to the existing LabVIEW™ based control software via a full 16-bit Ethernet connection. An identical power supply was installed at the 90° magnet of the low energy mass spectrometer, which also enables a 16-bit control and replaced the existing 11-bit system. This improvement enables one order of magnitude higher precision of controlling the current applied to the magnets. In addition a gas handling system for the required N_2 gas at the new 135° gas-filled magnet as well as the isobutane gas for the ionization chamber was designed, built and tested. It is now possible to evacuate, ventilate and control the injected gas pressure to the vacuum chamber as well as the ionization chamber mounted downstream, individually and with a high reproducibility. Furthermore, two NMR probes were mounted to radial ports of the 135° magnet, at the top of two movable rods. In this way, the homogeneity of the magnetic field was measured to $B_{hom} < 1.64 \times 10^{-4}$ in a range of ± 50 mm from the optical axis, which confirms the specifications of the manufacturer of $B_{hom} = 4 \times 10^{-4}$.

To expand the possibilities for ion beam detection, the existing 10 anode ionization chamber was put back into operation. This includes the recommissioning of the anodes and the wiring as well as the detector window mount. The total energy resolution was determined to $E_{res} = 1.72\%$ with a ^{12}C beam. During multiple measurements with ^{40}Ca, ^{39}K and ^{48}Ti as well as ^{58}Fe and ^{58}Ni the energy loss in different isobutane gas pressure along the flight path was investigated. The corresponding SRIM simulations were compared and analyzed with respect to deviations and similarities.

In parallel with this tests, a new compact 5 anode ionization chamber was developed and com- missioned. The detector is highly adaptable due to the layered structure. Since the corresponding housing can be mounted on both sides to the beam tube, the detector can be used at almost any location along the beam line. The energy resolution was determined to $E_{res} = 2.74\%$ with ^{13}C. First ^{10}Be AMS measurements at the 6 MV Tandetron™ accelerator revealed reliable isotopic ratios, down to $R(^{10}Be/Be) = 2 \times 10^{-13}$, with a mean correction factor of $c_f = 2.43$. These results are all within the 2σ error limits compared to the well known 4 anode ionization chamber from HVE used for these measurements ordinarily. Since the investigations and results concerning the new gas-filled magnet and the measurements performed with the 10 anode and 5 anode ionization chamber were taken into account for the later performed measurements with ^{58}Fe and ^{58}Ni as well as ^{41}Ca, a more detailed description of the results is given at the end of chapter 3.

The used MPA3 data acquisition systems at both accelerators are described in chapter 4. The important differences between `mpa` and `lst` list mode files, and the use of both in the context of data analysis, were investigated in detail. For a fast and effective data procession and analysis different software tools were developed and applied for the conducted measurements. An important step was the usage of the ROOT framework in the context of offline data analysis as well as graphic evaluation. Recorded binary list mode files can now be converted into dedicated ROOT files, including all timing informations for all detected signals. In addition a python tool was developed to extract and sort the data from `fsires` files recorded during AMS batch mode measurements at the 6 MV Tandetron™ accelerator. With this set of tools it was possible to process about 2500 recorded data files in a fast, reliable and dynamic way.

For upcoming measurements of ^{60}Fe, the dedicated AMS beamline at the 10 MV Tandem accelerator in combination with the new 135° gas-filled magnet is well suited, since the isobar ^{60}Ni should be separated well by the use of the new magnet. Within the scope of this thesis, the required investigations with stable ^{58}Fe and ^{58}Ni, the tuning procedure and the test measurements with the gas-filled magnet were conducted and are described in chapter 5. Investigations at the low energy mass spectrometer revealed that FeO^-, in comparison to elemental Fe^- or FeO_2^-, provide the largest beam output. The transmission between the low energy mass spectrometer and the Tandem accelerator is about 90% and the transmission between the 90° high energy magnet and the 135° gas-filled magnet is almost 100%. Without N_2 gas, it was possible to detect and analyze the charge state distribution produced by the entrance foil of the 135° magnet. The most abundant charge states at 100 MeV are 18^+ and 19^+ for ^{58}Fe and ^{58}Ni, respectively. The measured distribution fits well to the expected charge states calculated from eq. 2.7. By summing up the intensity of all charge states, a transmission of 53% through the magnet without N_2 gas was determined. Furthermore, the optimal N_2 gas pressure inside the vacuum chamber of the 135° magnet was investigated. The best separation factor of $S_f = 3.48$ was achieved at 7 mbar N_2 gas pressure. The corresponding beam width of a ^{58}Fe beam, with an initial energy of 100 MeV, at the end of the magnet is 12 mm for 1σ on the focal plane. The corresponding peak to peak separation from the ^{58}Ni component was measured to 84 mm. Both measurements were conducted with a silicon detector in combination with a 1 mm slit aperture mounted right after the 135° gas-filled magnet. It was further found that even a pure (not chemically cleaned) Fe_2O_3 sample contains a considerable high amount of ^{58}Ni and based on the high abundance of natural and stable ^{60}Ni of 26.223%[16] a large isobaric background for ^{60}Fe measurements can be expected. The new 5 anode ionization chamber was mounted after the 135° magnet and the measurements revealed that, at comparable beam energies of about 54 MeV for a ^{58}Fe beam, the separation between ^{58}Fe and ^{58}Ni is 36% larger after the gas-filled magnet than without the gas-filled magnet. This can be traced back to the different energy loss of Fe and Ni inside the N_2 gas. The problem determining separation factors of components with unequal energies was solved by performing a two dimensional Gaussian analysis on both peaks. In this way a separation factor of $S_f = 4.76$ for a ^{58}Fe beam at 7 mbar N_2 gas pressure and 28 mbar isobutane detector gas pressure could be determined. The achieved system settings for ^{58}Fe fully suppress the ^{58}Ni isobar inside the gas-filled magnet, whereby it becomes feasible to measure ^{60}Fe with very low ratios.

In chapter 6 two main questions were investigated. On the one hand, the actual limits for measurements of ^{41}Ca isotopic ratios with CaF_2 sample material at the Cologne 6 MV Tandetron™ accelerator were examined and on the other hand, if ^{41}Ca is suitable as a reference nuclide for nuclear waste management, with respect to the disassembling and dismantling of nuclear power plants. In a first phase, system settings were determined to measure ^{41}Ca standard and blank

[16] National Nuclear Data Center, Retrieved February 18,2019 from www.nndc.bnl.gov

samples. The lowest available standard with a nominal ratio of $R(^{41}Ca/Ca) = 5.885 \times 10^{-13}$ could be measured to $R = 4.70(79) \times 10^{-13}$ which corresponds to a correction factor of $c_f = 1.25$. The achieved blank level is 6×10^{-14} during the first batch measurements.

The traceability of ^{41}Ca in concrete material was investigated by irradiating heavy concrete samples with neutrons at the research reactor TRIGA Mark II at Mainz. The irradiation time was chosen between 30 s and 3000 s to achieve samples with an isotopic ratio across different orders of magnitude, between 10^{-9} and 10^{-11}. The expected radioactive activities as well as the expected isotopic ratios were calculated by taking the full neutron energy spectrum emitted from the research reactor and the corresponding energy depending neutron capture cross sections into account. In this way, the cross section is lowered from $\sigma = 0.40$ barn for thermal neutrons to a mean value of $\overline{\sigma} = 0.28$ barn, for this particular neutron spectrum. The comparison of calculated and measured isotopic ratios showed an excellent linearity over three orders of magnitude and revealed the high precision of the performed AMS measurements. This result confirms the possibility of investigating heavy concrete samples, irradiated with neutrons, with AMS methods and obtain informations concerning their radioactive activity. Therefore, ^{41}Ca seems to be a good candidate for a new reference nuclide in terms of nuclear waste management.

In a last step samples from a biological shield of a research reactor were investigated. The determined mean isotopic ratio is $\overline{R}_c = 6.39(74) \times 10^{-9}$ corresponding to a radioactive activity of 1.02 Bq/g. Since no detailed information about the sample extraction side, the neutron energy distribution or the total neutron flux are available, calculations were performed to assume these conditions. Two sets of parameters were found which would confirm the measured results. The determined radioactive activity produced by ^{41}Ca is therefore below the legal limit.

Outlook

According to the stability and the usable beam output, the MC-SNICS ion source used at the 10 MV Tandem accelerator should be improved as it is described by Southon et al. [120], which includes changes to the beam extraction to a more open structure for better vacuum. This could lead to higher usable currents on the high energy side, and therefore pave the way to measure smaller isotopic ratios. According to the accelerator setup, the installation of steerer pairs, after the offset Faraday cup chamber, for both axis could help to improve the tuning procedure. To further investigate the stability and reliability of the system, tests with $^{14}C/^{13}C$ should be performed. Since the offset Faraday cup chamber is limited in width, no ^{12}C can be measured at the same time. With regard to the new $135°$ gas-filled magnet, several measurements and further test can be performed, to better understand the beam path through the gas or to investigate other radionuclides. The investigation of the beam path could be done with five silicon detectors mounted to the radial ports of the magnet, similar to the installed NMR probes. The analysis of the beam shape should also be continued in the y-axis at the exit of the magnet. Since this beam broadening in y-axis is not affected by the magnetic field, but only by the gas pressure, the beam will leave the magnet with an elliptical shape, see Feuerstein [10]. To determine the transmission through the gas-filled magnet, a radionuclide should be used. The resulting correction factor c_f determined during an AMS measurement, is directly proportional to the transmission. The 5 anode ionization chamber should be moved further to the magnet exit, to reduce the beam broadening inside the field free region. Another step according to a higher beam acceptance, is to enlarge the detector entrance window, which could be done with a Mylar foil.

Apart from the intended ^{60}Fe, the radionuclide ^{63}Ni could be investigated with the new $135°$ gas-filled magnet. The corresponding isobaric component is ^{63}Cu. In this case the difference in nuclear charge Z is one, which will reduce the beam separation by the gas-filled magnet also by

half, compared to ^{60}Fe. Nevertheless, the resulting energy difference in the ionization chamber, between isotope and isobar, should allow a measurement. This radionuclide is of interest in the field of nuclear waste management.

After the first successful ^{41}Ca measurements at the 6 MV Tandetron™ accelerator, further samples from reactor buildings should be investigated. Measuring samples from a drill core for example could help to detect the effective shielding of the concrete and compare the results to the simulation. To be able to measure samples with lower ratios, two main aspects become crucial. On the one hand, the sample preparation must be accurate and reproducible. On the other hand, a new blank material has to be tested, to determine a more reliable blank level for the measurements. Another possibility could be to measure ^{41}Ca from CaH samples. In this case the source output can be increased and the transmission through the accelerator onto the desired charge state is enlarged.

Appendix A

Experimental and Accelerator Setup

5 Anode Gas Ionization Chamber

Detector Design

(a) Layer to smooth field boundary

(b) Layer to smooth field boundary, infront of the entrance window
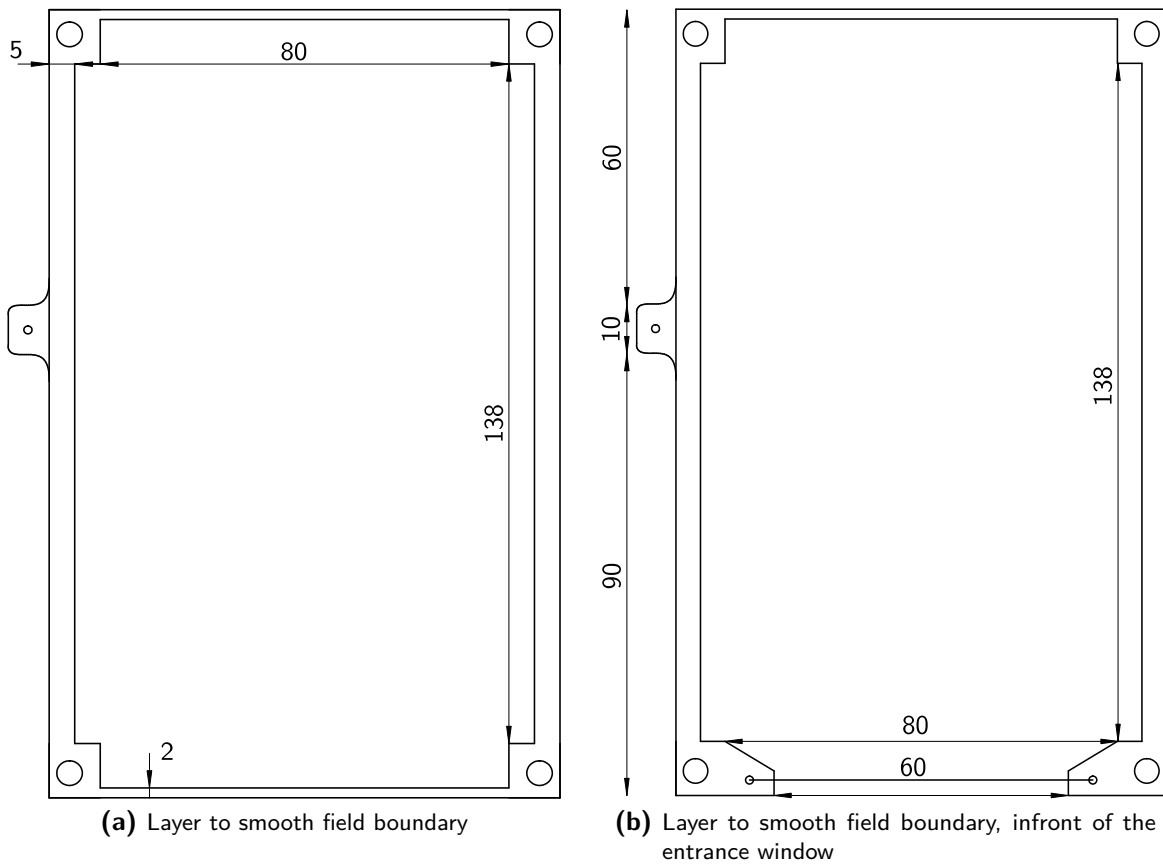
Figure 52: 5 anode ionization chamber layers to smooth the field boundary. Figure a) shows the standard layer. Figure b) shows a special layer used in the height of the entrance window. At this point, the front part of the layer is replaced by a 15 μm gold coated tungsten wire, to reduce beam scattering and losses.
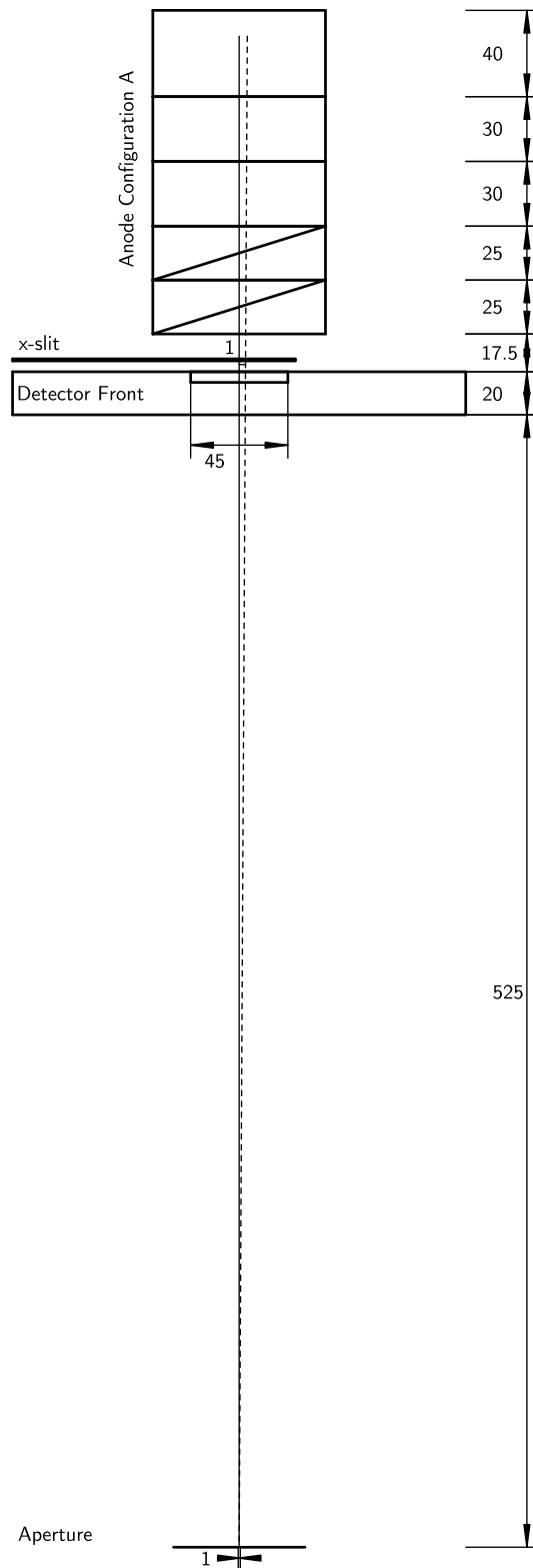
Figure 53: Principle of the measurement concerning the angular resolution of the new 5 anode ionization chamber, drawn to scale. All dimensions are given in mm. The center line describes a beam on the optical axis. The second line is rotated by 0.3°, around the aperture, which corresponds to a maximum beam deviation of 3 mm at the x-slit.

AMS Measurement with ^{10}Be

System Settings for ^{10}Be^{2+} at 13.53 MeV

Table 23: Settings for the AMS Tandetron™ accelerator for the measurement of ^{10}Be^{2+} at 4.51 MV terminal voltage and a beam energy of 13.53 MeV. These settings were determined and optimized by Dr. Stefan Heinze over several years of operation. The settings have been used to compare the results of the new designed 5 anode ionization chamber with the established 4 anode ionization chamber from HVE.

Section	Component	Value		Section	Component	Value	
SO-110	Cathode Volt.	6.999	kV	HES	Q-Pole Focus	44.13	%
	Sputter Curr.	0.4	mA		Q-Pole Astig.	0.31	%
	Extraction	28.00	kV		X-Steerer 1	1663	V
	Einzel Lens	14.74	kV		X-Steerer 2	−842	V
	Y-Steerer	118.5	V		Y-Steerer 1	−1013	V
	Ionizer	18.1	A		Y-Steerer 2	1653	V
	Cs-Oven	108.42	°C				
BI	ESA	3.940	kV	HEM	Magnet	65.888	A
	Magnet	67.752	A		ESA 1	64.825	kV
	Blanking St.	−55	V		ESA 2	64.825	kV
	X-Steerer 1	−97.8	V	HEE	Y-Steerer	1394	V
	X-Steerer 2	−78.3	V		Q-Pole Focus	36.92	%
	Y-Steerer 2	−93.2	V		Q-Pole Astig.	−8	%
	Einzel Lens	23.502	kV	DSW	Magnet	64.900	A
	X-Slits	10	mm		Q-Pole Focus	46.50	%
ACC	Terminal	4.510	MV		Q-Pole Astig.	−0.6	%
	Stripper-Gas	0.014	mbar				
	Q-snout	38.87	kV	AFD	Magnet	117.781	A
	Q-Pole Focus	49.26	%	5 Anode IC	Pressure	43.5	mbar
	Q-Pole Astig.	−2.77	%	4 Anode IC	Pressure	35	mbar

Appendix B

Data Analysis Code Blocks

List Mode file analysis with Root

To convert a < >.lst file to a < >.root file containing the corresponding root tree the following steps have to be performed:

1. For first usage got to folder with all required converter files and type in once: `make`
   This will compile the required C-functions and get all required libraries, the files are stored on the IKP server.

2. Change the number of ADC's in `mpa_to_root.cc` and if necessary the number of channels.

3. Enter `./mpa_to_root ␣ < >.lst -o ␣ < >_Tree.root`. This will convert a certain list mode file into a ROOT tree and save it to the < >_Tree.root output file.

4. For multiple files: `for i in 'find *.lst -printf "%f\\n"'; do ./mpa_to_root $i -o $i.root ; done`

5. The data, events and time information of a single file is stored to a branch named `ams` with individual ROOT leaves, named with `Anodes.A1 - Anodes.A8`.

6. Use ROOT C-code macro, to display and analyze the data, by typing to the ROOT terminal, `.x <Macro Name>.C`.
   It is also possible to simply view the single anode spectra with the ROOT TBrowser, by typing `new TBrowser()` to the ROOT terminal.

The given Python code code block B.1 renames all < >.lst files in the current directory. The standard filenames during a Batch mode measurement at the 6 MV Tandetron™ accelerator are increasing integer numbers corresponding to each performed run. Since the new < >.mpa and < >.fsires files are generated at the end of each run, the < >.lst filename is shifted by 1, for that reason 1.lst contains the list mode data corresponding to 2.mpa and 2.fsires. The given code corrects this, by renaming all < >.lst. In a second step the name of the parent directory is added to all files. In this way data files from different measurements can be distinguished.

Listing B.1: Python code to rename the recorded list mode files from Batch mode measurements at the standard data aquisition at the 6 MV Tandetron™ accelerator

```python
import string, sys, os, glob

dirpath = os.getcwd()
foldername = os.path.basename(dirpath)
pre = foldername + "_"
print("Directory name is : " + foldername)

if not os.path.isfile(foldername + "_1.mpa"):
  os.rename("1.lst", "1_.lst")
  i = 2
  max = 1000
  while i < max:
    a = str(i-1) + "_.lst"
    b = str(i) + ".lst"
    b_ = str(i) + "_.lst"
    if os.path.isfile(b):
      os.rename(b,b_)
      os.rename(a,b)
      i += 1
    else:
      os.rename(a,b)
      break
  types = ('*.lst', '*.mpa', '*.fsires')
  files_grabbed = []
  for files in types:
    files_grabbed.extend(glob.glob(files))
    for f in glob.glob(files):
      if not foldername in f:
        print("True")
        os.rename(f, "{}{}".format(pre, f))
        print("{}{}".format(pre, f))
else:
  print("Already renamed")
```

The following code extracts the most important information from all < >.`fsires` files within a folder and send it to a new, structured text file. In the given case, the generated file contains the run number, the sample ID, the samples description, the counts of the radionuclide, the corresponding statistical error the total counts, the measured current of the stable isotope, a pre-calculated ratio, the standard deviation and the detector live time. The resulting file can easily be imported to a spreadsheet program for further analysis.

Listing B.2: Python readout code for AMS `fsires` data files from Batch-Mode measurements.

```python
import string
import os
import re


i = 1
fname = "{0}{1}".format(i,".fsires")
matrix = []

header = ["#RunNr", "Sample ID", "Desc", "Ca41 counts", "Ca41 stat error", "Total
     ↪ counts","Ca40 current", "Ca41/Ca40", "R rel std dev", "Det Live Time"]
matrix.append(header)


while os.path.isfile(fname):
  fread = open(fname, "r")
  allLine = fread.readlines()
  fread.close()

  line = [i]


  lnumber = 0
  while lnumber < len(allLine):
    if re.match( r'(\bSample Id\b\s+:\s+)(\w+)', allLine[lnumber]):
      m = re.match( r'(\bSample Id\b\s+:\s+)(\w+)', allLine[lnumber])
      line.insert(1,m.group(2))
    elif re.match( r'(\bSample description\b\s+:\s+)(\w+)', allLine[lnumber]):
      m = re.match( r'(\bSample description\b\s+:\s+)(.+)', allLine[lnumber])
      line.insert(2,m.group(2))
    elif re.match( r'(\bCa41 counts\b\s+:\s+)(\w+)', allLine[lnumber]):
      m = re.match( r'(\bCa41 counts\b\s+:\s+)(\w+)', allLine[lnumber])
      line.insert(3,m.group(2))
    elif re.match( r'(Ca41 statistical error \(\%\)\s+:\s+)(.+)', allLine[lnumber]):
      m = re.match( r'(Ca41 statistical error \(\%\)\s+:\s+)(.+)', allLine[lnumber])
      line.insert(4,m.group(2))
    elif re.match( r'(\bTotal counts\b\s+:\s+)([0-9]+)', allLine[lnumber]):
      m = re.match( r'(\bTotal counts\b\s+:\s+)([0-9]+)', allLine[lnumber])
      line.insert(5,m.group(2))
    elif re.match( r'(Ca40 current \[A\]\s+:\s+)(.+)', allLine[lnumber]):
      m = re.match( r'(\bCa40 current\b \[A\]\s+:\s+)(.+)', allLine[lnumber])
      line.insert(6,m.group(2))
    elif re.match( r'(Ca41\/Ca40 ratio\s+:\s+)(.+)', allLine[lnumber]):
      m = re.match( r'(\bCa41\/Ca40 ratio\b\s+:\s+)(.+)', allLine[lnumber])
      line.insert(7,m.group(2))
    elif re.match( r'(Ca41\/Ca40 rel std dev \(\%\)\s+:\s+)(.+)', allLine[lnumber]):
      m = re.match( r'(Ca41\/Ca40 rel std dev \(\%\)\s+:\s+)(.+)', allLine[lnumber])
      line.insert(8,m.group(2))
    elif re.match( r'(\bDetector live time\b\s\[s\]\s+:\s+)(.+)', allLine[lnumber]):
      m = re.match( r'(\bDetector live time\b\s\[s\]\s+:\s+)(.+)', allLine[lnumber])
      line.insert(8,m.group(2))
```

MPA file handling with Python

In contrast to the list mode files, which a stored in a binary file format, the `< >.mpa` files are stored to ASCII files by default. These files contain all informations of a single measurement and the recorded pre-configured spectra. To extract and plot such a recorded spectrum, a Python code was written to convert the data into a files readable with Gnuplot, which is the standard plot program at the Institute for Nuclear Physics in Cologne.

Listing B.3: Python script for `< >.mpa` files including zero events.

```python
import string, sys, os
if (len(sys.argv)!=2):
    print(("Usage : %s Input File" % (sys.argv[0])))
    sys.exit()

file_name = str(sys.argv[1])

with open(file_name, "r") as fread:
    while True:
        theline = fread.readline()
        if not theline: break
        theline = theline.strip("\n")
        if "[CDAT3,1048576 ]" in theline:
            theline = fread.readline()
            theline = theline.strip("\n")
            list = []
            for y in range(1, 1024):
                for x in range(1, 1024):
                    line = (str(x) + "\t" + str(y) + "\t" + theline)
                    list.append(line)
                    theline = fread.readline()
                    theline = theline.strip("\n")
                list.append("")
            theline = fread.readline()
            theline = theline.strip("\n")

file_save = file_name.strip(".mpa")
file = open(file_save + "gnuplot.txt","w")

i = 0
while i < len(list):
    #print list[i]
    file.write("%s\n" % list[i])
    i += 1

file.close()
fread.close()
```

Python code for the conversion of < >.mpa files, recorded without zero events.

Listing B.4: Python script for mpa files without zero events.

```python
import string, sys, os
if (len(sys.argv)!=2):
    print(("Usage : %s Input File" % (sys.argv[0])))
    sys.exit()

file_name = str(sys.argv[1])

with open(file_name, "r") as fread:
    while True:
        theline = fread.readline()
        if not theline: break
        if "[CDAT3,1048576 ]" in theline: break

    while True:
        theline = fread.readline()
        if not theline: break
        if "[DATA]" in theline: break

    theline = fread.readline()
    theline = theline.strip("\n")
    theline = theline.split("\t")
    list = []
    for x in range(1, 1024):
        if "[" in theline: break
        for y in range(1, 1024):
            if str(x) == theline[1] and str(y) == theline[0]:
                line = (str(y) + "\t" + str(x) + "\t" + theline[2])
                print line
                list.append(line)
                theline = fread.readline()
                if "[" in theline: break
                if theline:
                    theline = theline.strip("\n")
                    theline = theline.split("\t")
                else:
                    theline = ["1","1","0"]
            else:
                line = (str(y) + "\t" + str(x) + "\t0")
                list.append(line)
        list.append("")

file_save = file_name.strip(".mpa")
file = open(file_save + "gnuplot.txt","w")

i = 0
while i < len(list):
    #print list[i]
    file.write("%s\n" % list[i])
    i += 1

file.close()
fread.close()
```

105

Appendix C

Measurements with ^{58}Fe at the 10 MV Tandem accelerator

In fig. 54 the charge state distribution without gas, explained in sec. 5.3, for ^{58}Fe at 100 MeV is plotted in combination with the measured distribution after 6 mbar N_2 gas pressure (red curve). The measured currents were normalized to the areas under the Gaussian fits done to each charge state. The mean charge state for ^{58}Fe at 6 mbar gas pressure was calculated to $q_m = 12^+$ from eq. 2.6. The particles lose about $E_{loss} = 54.44$ MeV inside this 2121 mm long gas-filled region. Therefore, lower magnetic fields are required to bend the beam to the correct trajectory and the resulting q_m is shifted in the spectrum.
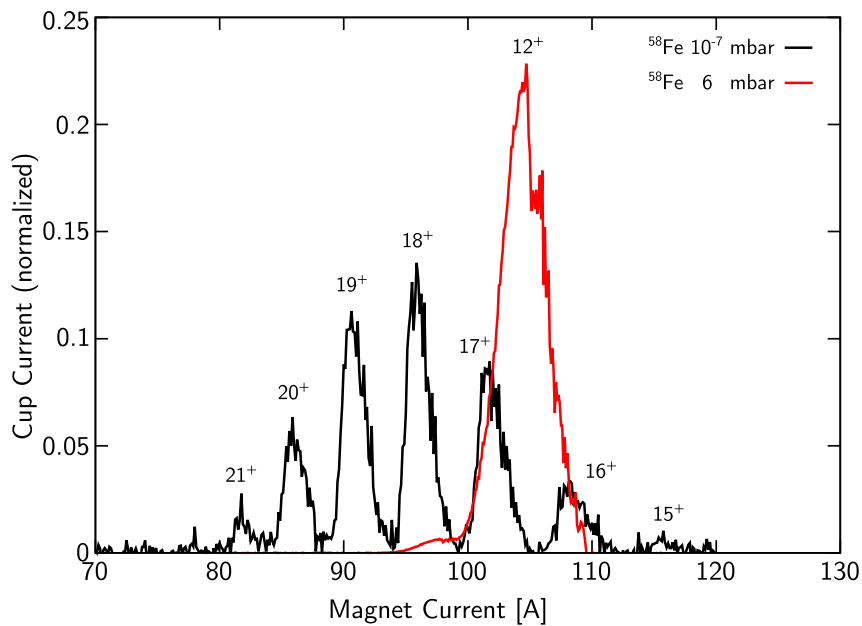
Figure 54: The figure shows a trace of the 135° gas-filled magnet for ^{58}Fe with (red curve) and without (black curve) 6 mbar of N_2 gas pressure. The measured currents were normalized to the areas under the Gaussian fits done to each charge state. The calculated mean charge state q_m is 12^+.

Appendix D

^{41}Ca Measurements

(a) ^{41}Ca blank

(b) ^{41}Ca C16 standard sample

(c) ^{41}Ca C18 standard sample

(d) ^{41}Ca C20 standard sample
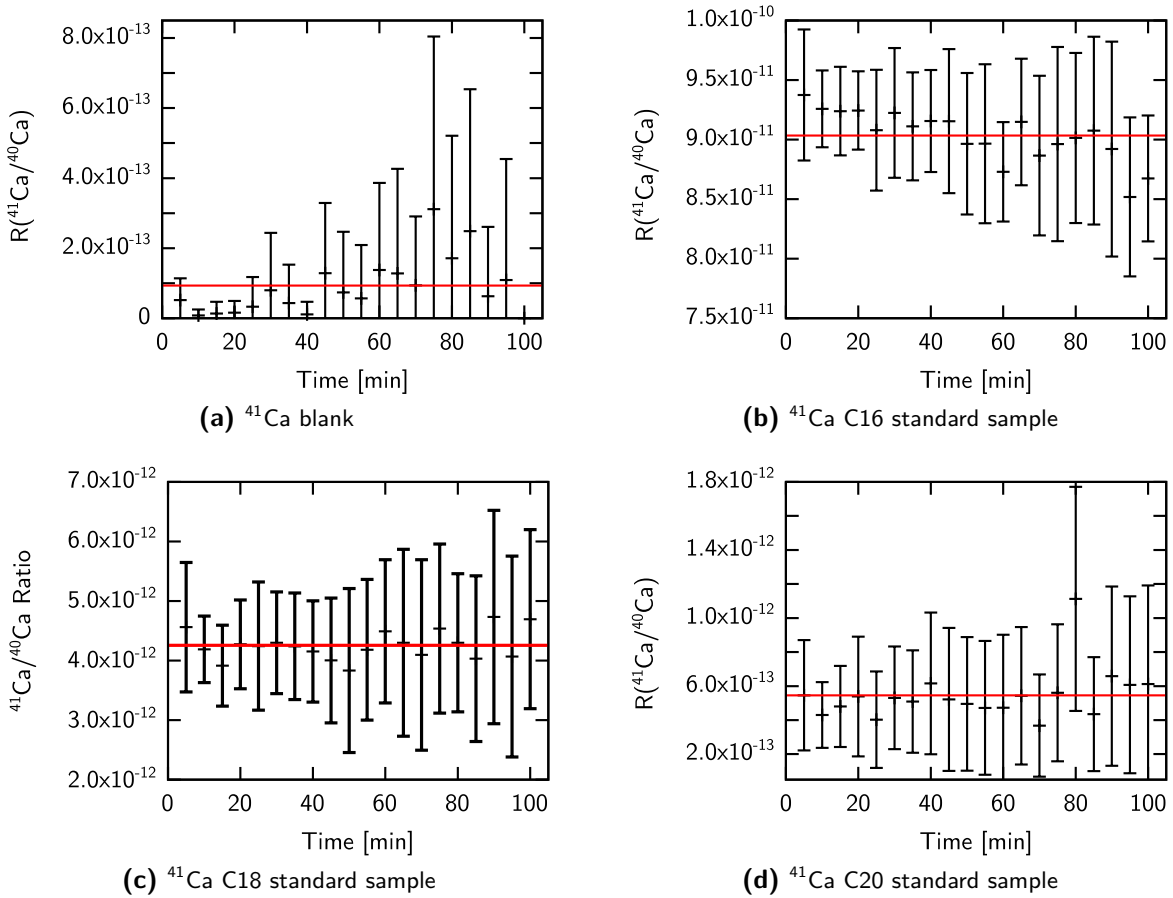
Figure 55: Similar to fig. 42 the figure shows the second measurement of standard samples. The given values are averaged for every run over all measured samples of the same kind. The red line indicated the calculated mean value. The corresponding values for every sample and the calculated correction factors are given in tab. 15

Table 24: Results of the XRF analysis of different concrete samples, provided by PD Dr. Erik Strub

Compound	Sample [%]	Baryt [%]	DIN [%][17]
SiO$_2$	6.50	5.21	2 - 15
TiO$_2$	0.11	0.23	
Al$_2$O$_3$	2.57	1.28	2 - 15
Fe$_2$O$_3$	76.90	0.96	1 - 2
MnO	0.24	—	
MgO	0.49	0.12	
CaO	6.97	8.68	2 - 15
K$_2$O	0.17	0.23	
Na$_2$O	—	2.24	
P$_2$O$_5$	0.51	0.04	
SO$_3$	—	21.40	10 - 14
Ba	0.06	52.05	45 - 54

Compound	Sample [ppm]	Baryt [ppm]
V	130	110
Cr	413	—
Co	—	7
Ni	151	60
Zn	53	469
Ga	9	—
Rb	25	33
Sr	217	2903
Nb	15	22
Zr	55	55
Y	27	17
Cu	178	125
Sn	235	188
Pb	5	113
Sc	—	—
Mo	27	3
La	158	—
Ce	49	161
Nd	17	—

[17] Compare to DIN 25413-1 [115]

Table 25: Results of the first ^{41}Ca measurement at the 6 MV Tandetron™ accelerator of concrete samples irradiated with neutrons. The measurements are sorted by the sample ID and the corresponding irradiation time. The displayed sum values for the detected counts N, the measured current $\bar{I}$ and the corresponding corrected ratio $\bar{R}_c$ are calculated as described in sec. 4.4. The measurement time for each sample was about 26 min.

Irrad. Time [sec]	Sample ID	N(^{41}Ca)	$\bar{I}$(^{40}Ca) [nA]	$\bar{R}_c$(^{41}Ca/^{40}Ca)
30	1bth1	1649	31.70	2.38(29) $\times 10^{-11}$
30	1cth1	5561	108.49	2.35(20) $\times 10^{-11}$
30	1dth1	8760	161.91	2.49(31) $\times 10^{-11}$
30	1fth1	1950	40.99	2.18(22) $\times 10^{-11}$
300	2ath1	16 645	50.62	1.51(3) $\times 10^{-10}$
300	2bth1	26 080	83.31	1.43(3) $\times 10^{-10}$
300	2cth1	26 412	82.02	1.47(3) $\times 10^{-10}$
300	2dth1	21 232	63.16	1.54(3) $\times 10^{-10}$
300	2eth1	13 736	37.04	1.70(5) $\times 10^{-10}$
300	2fth1	14 065	42.19	1.53(3) $\times 10^{-10}$
30	3ath1	2611	57.70	2.07(10) $\times 10^{-11}$
30	3bth1	1490	36.96	1.85(17) $\times 10^{-11}$
30	3cth1	1493	34.09	2.00(15) $\times 10^{-11}$
30	3dth1	1922	50.66	1.74(11) $\times 10^{-11}$
30	3eth1	3444	32.79	4.82(54) $\times 10^{-11}$
30	3fth1	2164	53.43	1.85(12) $\times 10^{-11}$
1000	4ath1	80 028	76.48	4.79(4) $\times 10^{-10}$
1000	4bth1	77 393	73.26	4.84(4) $\times 10^{-10}$
1000	4cth1	73 506	69.20	4.86(5) $\times 10^{-10}$
1000	4dth1	104 186	98.58	4.85(5) $\times 10^{-10}$
1000	4eth1	59 465	55.68	4.89(5) $\times 10^{-10}$
1000	4fth1	49 282	46.17	4.89(6) $\times 10^{-10}$
3000	5ath1	126 220	38.45	1.51(1) $\times 10^{-9}$
3000	5bth1	242 731	110.47	1.49(1) $\times 10^{-9}$
3000	5cth1	134 753	41.93	1.47(1) $\times 10^{-9}$
3000	5dth1	181 274	57.65	1.48(1) $\times 10^{-9}$
3000	5eth1	226 749	82.67	1.46(1) $\times 10^{-9}$
3000	5fth1	178 801	55.91	1.46(1) $\times 10^{-9}$
	Blank	1236	123.36	9.69(397) $\times 10^{-13}$
	Std C16	189 682	188.10	9.80(15) $\times 10^{-11}$
	Std C20	1345	164.38	8.16(225) $\times 10^{-13}$

Table 26: Results of the third ^{41}Ca measurement at the 6 MV Tandetron™ accelerator of concrete samples irradiated with neutrons. The measurements are sorted by the sample ID and the corresponding irradiation time. The displayed sum values for the detected counts N, the measured current $\bar{I}$ and the corresponding corrected ratio $\bar{R}_c$ are calculated as described in sec. 4.4.

Irrad. Time [sec]	Sample ID	$N(^{41}Ca)$	$\bar{I}(^{40}Ca)$ [nA]	$\bar{R}_c(^{41}Ca/^{40}Ca)$
30	1bth3	821	29.43	1.20(15) $\times 10^{-11}$
30	1cth3	3595	96.94	1.60(8) $\times 10^{-11}$
30	1dth3	3249	75.44	1.86(9) $\times 10^{-11}$
30	1fth3	891	22.91	1.68(20) $\times 10^{-11}$
300	2ath3	4830	12.56	1.66(6) $\times 10^{-10}$
300	2bth3	8639	26.43	1.41(4) $\times 10^{-10}$
300	2cth3	14 006	41.90	1.44(3) $\times 10^{-10}$
300	2dth3	9864	28.52	1.49(4) $\times 10^{-10}$
300	2eth3	5004	14.71	1.47(5) $\times 10^{-10}$
300	2fth3	10 484	30.40	1.49(3) $\times 10^{-10}$
30	3ath3	1164	26.09	1.92(14) $\times 10^{-11}$
30	3bth3	1197	29.55	1.75(16) $\times 10^{-11}$
30	3cth3	1195	29.82	1.73(13) $\times 10^{-11}$
30	3dth3	1218	34.16	1.54(14) $\times 10^{-11}$
30	3eth3	1646	31.52	2.25(18) $\times 10^{-11}$
30	3fth3	1549	37.36	1.79(15) $\times 10^{-11}$
1000	4ath3	52 485	48.71	4.65(5) $\times 10^{-10}$
1000	4bth3	43 244	39.61	4.71(7) $\times 10^{-10}$
1000	4cth3	48 258	44.15	4.71(6) $\times 10^{-10}$
1000	4dth3	69 991	64.12	4.71(4) $\times 10^{-10}$
1000	4eth3	36 405	32.40	4.85(7) $\times 10^{-10}$
1000	4fth3	36 827	32.72	4.85(7) $\times 10^{-10}$
3000	5ath3	59 756	17.34	1.49(1) $\times 10^{-9}$
3000	5bth3	214 656	63.94	1.45(1) $\times 10^{-9}$
3000	5cth3	112 718	34.03	1.43(1) $\times 10^{-9}$
3000	5dth3	139 830	41.67	1.45(1) $\times 10^{-9}$
3000	5eth3	157 472	47.51	1.43(1) $\times 10^{-9}$
3000	5fth3	137 431	41.29	1.44(1) $\times 10^{-9}$
	Blank	389	113.36	6.70(681) $\times 10^{-13}$
	Std C16	58 974	110.08	1.04(2) $\times 10^{-10}$
	Std C20	642	114.82	1.08(21) $\times 10^{-12}$

Bibliography

[1] **L. K. Fifield**. "Accelerator mass spectrometry and its applications". *Reports on Progress in Physics* 62.8 (Aug. 1999), pp. 1223–1274.

[2] **J. Chen, Z. Guo, K. Liu, and L. Zhou**. "Development of Accelerator Mass Spectrometry and Its Applications". *Reviews of Accelerator Science and Technology* 04.01 (Jan. 2011), pp. 117–145.

[3] **M. Schiffer**. "Ein dediziertes Beschleuniger-Massenspektrometer für mittelschwere Radionuklide am Kölner FN-Tandembeschleuniger". *PhD Thesis, University of Cologne* (Mar. 2018).

[4] **H. Bethe**. "Zur Theorie des Durchgangs schneller Korpuskularstrahlen durch Materie". *Annalen der Physik* 397.3 (1930), pp. 325–400.

[5] **F. Bloch**. "Zur Bremsung rasch bewegter Teilchen beim Durchgang durch Materie". *Annalen der Physik* 408.3 (1933), pp. 285–320.

[6] **J. Lindhard and A. H. Soerensen**. "Relativistic theory of stopping for heavy ions". *Physical Review A* 53.4 (Apr. 1996), pp. 2443–2456.

[7] **J. F. Ziegler, M. Ziegler, and J. Biersack**. "SRIM – The stopping and range of ions in matter (2010)". *Nuclear Instruments and Methods in Physics Research Section B: Beam Interactions with Materials and Atoms* 268.11-12 (June 2010), pp. 1818–1823.

[8] **O. Tarasov and D. Bazin**. "LISE++: Radioactive beam production with in-flight separators". *Nuclear Instruments and Methods in Physics Research Section B: Beam Interactions with Materials and Atoms* 266.19-20 (Oct. 2008), pp. 4657–4664.

[9] **W. H. Bragg and R. Kleeman**. "XXXIX. On the α particles of radium, and their loss of range in passing through various atoms and molecules". *The London, Edinburgh, and Dublin Philosophical Magazine and Journal of Science* 10.57 (Sept. 1905), pp. 318–340.

[10] **C. Feuerstein**. "Improvement of measurement capabilities at the Cologne Accelerator Mass Spectrometer". *PhD Thesis, University of Cologne* (Mar. 2018).

[11] **N. Bohr**. "Scattering and Stopping of Fission Fragments". *Physical Review* 58.7 (Oct. 1940), pp. 654–655.

[12] **E. Bonderup and P. Hvelplund**. "Stopping Power and Energy Straggling for Swift Protons". *Physical Review A* 4.2 (Aug. 1971), pp. 562–569.

[13] **W. K. Chu**. "Calculation of energy straggling for protons and helium ions". *Physical Review A* 13.6 (June 1976), pp. 2057–2060.

[14] **W. Lenz**. "Über die Anwendbarkeit der statistischen Methode auf Ionengitter". *Zeitschrift für Physik* 77.11-12 (Nov. 1932), pp. 713–721.

[15] **J. Jansen, C. Alderliesten, A. van Bennekom, K. van der Borg, and A. de Jong**. "Terrigenous supply of 10Be and dating with 14C and 10Be in sediments of the Angola basin (SE Antlantic)". *Nuclear Instruments and Methods in Physics Research Section B: Beam Interactions with Materials and Atoms* 29.1-2 (Nov. 1987), pp. 311–316.

[16] **Q. Yang, D. O'Connor, and Z. Wang**. "Empirical formulae for energy loss straggling of ions in matter". *Nuclear Instruments and Methods in Physics Research Section B: Beam Interactions with Materials and Atoms* 61.2 (Aug. 1991), pp. 149–155.

[17] **J. P. Biersack and J. F. Ziegler**. "The Stopping and Range of Ions in Solids". *Ion Implantation Techniques* 22.3 (Mar. 1982), pp. 122–156.

[18] **E. J. Williams**. "Concerning the scattering of fast electrons and of cosmic-ray particles". *Proceedings of the Royal Society of London. Series A. Mathematical and Physical Sciences* 169.939 (Mar. 1939), pp. 531–572.

[19] **P. Sigmund and K. Winterbon**. "Small-angle multiple scattering of ions in the screened Coulomb region". *Nuclear Instruments and Methods* 119.8 (July 1974), pp. 541–557.

[20] **G. Molière**. "Theorie der Streuung schneller geladenen Teilchen II Mehrfach- und Vielfachstreuung". *Zeitschrift für Naturforschung* 3a (Feb. 1948), pp. 78–97.

[21] **L. Meyer**. "Plural and multiple scattering of low-energy heavy particles in solids". *Physica Status Solidi (b)* 44.1 (Mar. 1971), pp. 253–268.

[22] **R. Anne, J. Herault, R. Bimbot, H. Gauvin, G. Bastin, and F. Hubert**. "Multiple angular scattering of heavy ions (16,17O, 40Ar, 86Kr and 100Mo) at intermediate energies (20–90 MeV/u)". *Nuclear Instruments and Methods in Physics Research Section B: Beam Interactions with Materials and Atoms* 34.3 (Sept. 1988), pp. 295–308.

[23] **L. Flamm and R. Schumann**. "Die Geschwindigkeitsabnahme der α-Strahlen in Materie". *Annalen der Physik* 355.14 (May 1916), pp. 655–699.

[24] **G. H. Henderson**. "Changes in the Charge of an α -Particle Passing through Matter". *Proceedings of the Royal Society of London. Series A, Containing Papers of a Mathematical and Physical Character* 102.717 (Jan. 1923), pp. 496–506.

[25] **N. Bohr**. "Velocity-Range Relation for Fission Fragments". *Physical Review* 59.3 (Feb. 1941), pp. 270–275.

[26] **N. Bohr**. "The Penetration of Atomic Particles Through Matter". *Mathematisk-fysiske meddelelser* 18 (1948).

[27] **W. E. Lamb**. "Passage of Uranium Fission Fragments Through Matter". *Physical Review* 58.8 (Oct. 1940), pp. 696–702.

[28] **H.-D. Betz, G. Hortig, E. Leischner, C. Schmelzer, B. Stadler, and J. Weihrauch**. "The average charge of stripped heavy ions". *Physics Letters* 22.5 (Sept. 1966), pp. 643–644.

[29] **H. D. Betz**. "Charge States and Charge-Changing Cross Sections of Fast Heavy Ions Penetrating Through Gaseous and Solid Media". *Reviews of Modern Physics* 44.3 (July 1972), pp. 465–539.

[30] **R. Sayer**. "Semi-empirical formulas for heavy-ion stripping data". *Revue de Physique Appliquée* 12.10 (Oct. 1977), pp. 1543–1546.

[31] **A. S. Schlachter, J. W. Stearns, W. G. Graham, K. H. Berkner, R. V. Pyle, and J. A. Tanis**. "Electron capture for fast highly charged ions in gas targets: An empirical scaling rule". *Physical Review A* 27.6 (June 1983), pp. 3372–3374.

[32] **J. Sarén, J. Uusitalo, M. Leino, and J. Sorri**. "Absolute transmission and separation properties of the gas-filled recoil separator RITU". *Nuclear Instruments and Methods in Physics Research Section A: Accelerators, Spectrometers, Detectors and Associated Equipment* 654.1 (Oct. 2011), pp. 508–521.

[33] **J. Sarén**. "The ion-optical design of the MARA recoil separator and absolute transmission measurements of the RITU gas-filled recoil by". *PhD Thesis, University of Jyväskyla* (Dec. 2011).

[34] **U. Zoppi**. "Isobar Suppression in Accelerator Mass Spectrometry". *PhD Thesis, University of Zurich* (1993).

[35] **M. Poutivtsev**. "Extraterrestrisches 53Mn in hydrogenetischen Mangankrusten". *PhD Thesis, University of Munich* (Apr. 2007).

[36] **K. Knie**. "Beschleunigermassenspektrometrie mit Isobarenseparation in einem dedizierten gasgefüllten Magneten". *PhD Thesis, University of Munich* (1997).

[37] **M. Martschini, J. Buchriegler, P. Collon, W. Kutschera, J. Lachner, W. Lu, A. Priller, P. Steier, and R. Golser**. "Isobar separation of 93Zr and 93Nb at 24MeV with a new multi-anode ionization chamber". *Nuclear Instruments and Methods in Physics Research Section B: Beam Interactions with Materials and Atoms* 361 (Oct. 2015), pp. 201–206.

[38] **R. Middleton**. "A Negative Ion Cookbook". *University of Pennsylvania* (Feb. 1990).

[39] **I. Langmuir and K. H. Kingdon**. "THERMIONIC EFFECTS CAUSED BY ALKALI VAPORS IN VACUUM TUBES". *Science* 57.1463 (Jan. 1923), pp. 58–60.

[40] **J. F. Wendt and A. B. Cambel**. "Surface Ionization of Potassium on Tungsten". *Journal of Applied Physics* 34.1 (Jan. 1963), pp. 176–178.

[41] **W. Kutschera, I. Ahmad, B. Glagola, R. Pardo, K. Rehm, D. Berkovits, M. Paul, J. Arnold, and K. Nishiizumi**. "Accelerator mass spectrometry of 59Ni in extraterrestrial matter". *Nuclear Instruments and Methods in Physics Research Section B: Beam Interactions with Materials and Atoms* 73.3 (Mar. 1993), pp. 403–412.

[42] **W. Shockley**. "Currents to Conductors Induced by a Moving Point Charge". *Journal of Applied Physics* 9.10 (Oct. 1938), pp. 635–636.

[43] **S. Ramo**. "Currents Induced by Electron Motion". *Proceedings of the IRE* 27.9 (Sept. 1939), pp. 584–585.

[44] **O. Frisch**. "Isotope Analysis Of Uranium Samples By Means Of Their Alpha Ray Groups". *British Atomic Energy Report* BR-49 (1944), p. 7.

[45] **M. Paul, B. G. Glagola, W. Henning, J. G. Keller, W. Kutschera, Z. Liu, K. E. Rehm, B. Schneck, and R. H. Siemssen**. "Heavy ion separation with a gas-filled magnetic spectrograph". *Nuclear Instruments and Methods in Physics Research Section A: Accelerators, Spectrometers, Detectors and Associated Equipment* 277.2-3 (May 1989), pp. 418–430.

[46] **C. B. Fulmer and B. L. Cohen**. "Equilibrium Charges of Fission Fragments in Gases". *Physical Review* 109.1 (Jan. 1958), pp. 94–99.

[47] **P. W. Kubik, D. Elmore, T. K. Hemmick, and W. Kutschera**. "The gas-filled magnet: An isobar separator for accelerator mass spectrometry". *Nuclear Inst. and Methods in Physics Research, B* 40-41.PART 2 (Apr. 1989), pp. 741–744.

[48] **K. Knie, T. Faestermann, G. Korschinek, G. Rugel, W. Rühm, and C. Wallner**. "High-sensitivity AMS for heavy nuclides at the Munich Tandem accelerator". *Nuclear Instruments and Methods in Physics Research Section B: Beam Interactions with Materials and Atoms* 172.1-4 (Oct. 2000), pp. 717–720.

[49] **R. Hellborg**. *Electrostatic Accelerators*. Particle Acceleration and Detection. Berlin/Heidelberg: Springer-Verlag, 2005.

[50] **K. van der Borg, A. P. de Haas, A. M. Hoogenboom, B. A. Strasters, A. Vermeer, and N. A. van Zwol**. "The injector of the Utrecht en tandem". *Nuclear Instruments and Methods In Physics Research* 220.1 (Feb. 1984), pp. 115–117.

[51] **A. Dewald, S. Heinze, J. Jolie, A. Zilges, T. Dunai, J. Rethemeyer, M. Melles, M. Staubwasser, B. Kuczewski, J. Richter, U. Radtke, F. von Blanckenburg, and M. Klein**. "CologneAMS, a dedicated center for accelerator mass spectrometry in Germany". *Nuclear Instruments and Methods in Physics Research Section B: Beam Interactions with Materials and Atoms* 294 (Jan. 2011), pp. 18–23.

[52] **A. Gottdang, D. J. W. Mous, and R. G. Haitsma**. "The novel HVEE 5 MV Tandetron™". *Nuclear Instruments and Methods in Physics Research, Section B: Beam Interactions with Materials and Atoms* 190.1-4 (May 2002), pp. 177–182.

[53] **M. Schenkel**. "Eine neue Schaltung für die Erzeugung hoher Gleichspannungen". *Elektrotechnische Zeitschrift* 40.28 (July 1919), pp. 333–334.

[54] **A. Stolz, A. Dewald, R. Altenkirch, S. Herb, S. Heinze, M. Schiffer, C. Feuerstein, C. Müller-Gatermann, A. Wotte, J. Rethemeyer, and T. Dunai**. "Radiocarbon measurements of small gaseous samples at CologneAMS". *Nuclear Instruments and Methods in Physics Research Section B: Beam Interactions with Materials and Atoms* 406 (Sept. 2017), pp. 283–286.

[55] **K. Purser**. "INJECTION SYSTEM FOR TANDEM ACCELERATORS". *United States Patent 5,247,263* (Sept. 1993), p. 7.

[56] **C. Müller-Gatermann**. "Aufbau eines Datenaufnahmesystems für das Flugzeitspektrometer am CologneAMS-Beschleuniger und Optimierung der Betriebsparameter". *Magisterarbeit, University of Cologne* (Jan. 2014).

[57] **A. Stolz**. "Einrichtung und Weiterentwicklung eines 14CO2-Systems am 6 MV TANDETRON Beschleuniger des CologneAMS". *PhD Thesis, University of Cologne* (Feb. 2019).

[58] **K. Knie, T. Faestermann, and G. Korschinek**. "AMS at the Munich gas-filled analyzing magnet system GAMS". *Nuclear Instruments and Methods in Physics Research Section B: Beam Interactions with Materials and Atoms* 123.1-4 (Mar. 1997), pp. 128–131.

[59] **Danfysik**. "Technical Drawing 135° GFM" (2016).

[60] **Scanditronix**. *NMR 851PC Operation Manual*. Tech. rep. 1990.

[61] **R. Salzer, S. Thiele, and S. Paasch**. "Grundlagen der NMR-Spektroskopie". *Wiley-VCH Verlag GmbH* (1999), pp. 1–31.

[62] **M. H. Levitt**. *Spin dynamics: Basics of nuclear magnetic resonance, 2nd edition.* 2nd ed. Vol. 2. 1. John Wiley & Sons, Jan. 2008, p. 752.

[63] **S. Herb**. "Automation of AMS measurements at the Cologne 10 MV FN Tandem Accelerator". *Master Thesis, University of Cologne* (Mar. 2018).

[64] **K. van der Borg, C. Alderliesten, H. Haitjema, G. Hut, and N. A. van Zwol**. "The Utrecht accelerator facility for precision dating with radionuclides". *Nuclear Inst. and Methods in Physics Research, B* 5.2 (Nov. 1984), pp. 150–154.

[65] **G. F. Knoll**. *Radiation Detection and Measurement*. 4th ed. John Wiley & Sons, Jan. 2010.

[66] **G. Hackenberg**. "Entwicklung eines Gasionisationsdetektors für Schwerionen". *Bachelor Thesis, University of Cologne* (May 2015).

[67] **S. Kurtz**. "Design and development of a new gas-filled detection system for the focal plane of Notre Dame's Browne-Büchner Spectrograph". *Thesis, University of Notre Dame* (Apr. 2007), p. 84.

[68] **J. R. Erskine, T. H. Braid, and J. C. Stoltzfus**. "An ionization-chamber type of focal-plane detector for heavy ions". *Nuclear Instruments and Methods* 135.1 (May 1976), pp. 67–82.

[69] **D. Shapira, R. M. Devries, H. W. Fulbright, J. Toke, and M. R. Clover**. "The Rochester heavy ion detector". *Nuclear Instruments and Methods* 129.1 (Nov. 1975), pp. 123–130.

[70] **H. Sann, H. Damjantschitsch, D. Hebbard, J. Junge, D. Pelte, B. Povh, D. Schwalm, and D. B. Tran Thoai**. "A position-sensitive ionization chamber". *Nuclear Instruments and Methods* 124.2 (Mar. 1975), pp. 509–519.

[71] **K. Kusterer, J. Betz, H. L. Harney, B. Heck, Liu Ken Pao, and F. Porto**. "GAS DETECTOR SYSTEM FOR MASS AND CHARGE IDENTIFICATION OF HEAVY IONS." *Nuclear instruments and methods* 177.2-3 (Nov. 1980), pp. 485–494.

[72] **G. Rosner, B. Heck, J. Pochodzalla, G. Hlawatsch, B. Kolb, and A. Miczaika**. "A new position measurement for ionization chambers". *Nuclear Instruments and Methods* 188.3 (Oct. 1981), pp. 561–569.

[73] **T. J. Dunai**. *Cosmogenic Nuclides.* Cambridge: Cambridge University Press, 2010, p. 199.

[74] **G. Korschinek, A. Bergmaier, T. Faestermann, U. Gerstmann, K. Knie, G. Rugel, A. Wallner, I. Dillmann, G. Dollinger, C. L. von Gostomski, K. Kossert, M. Maiti, M. Poutivtsev, and A. Remmert**. "A new value for the half-life of 10Be by Heavy-Ion Elastic Recoil Detection and liquid scintillation counting". *Nuclear Instruments and Methods in Physics Research Section B: Beam Interactions with Materials and Atoms* 268.2 (Jan. 2010), pp. 187–191.

[75] **D. E. Granger and P. F. Muzikar**. "Dating sediment burial with in situ-produced cosmogenic nuclides: Theory, techniques, and limitations". *Earth and Planetary Science Letters* 188.1-2 (May 2001), pp. 269–281.

[76] **M. Baroni, E. Bard, J. R. Petit, O. Magand, and D. Bourlès**. "Volcanic and solar activity, and atmospheric circulation influences on cosmogenic10Be fallout at Vostok and Concordia (Antarctica) over the last 60years". *Geochimica et Cosmochimica Acta* 75.22 (Nov. 2011), pp. 7132–7145.

[77] **A. Wallner, L. Coquard, I. Dillmann, O. Forstner, R. Golser, M. Heil, F. Käppeler, W. Kutschera, A. Mengoni, L. Michlmayr, A. Priller, P. Steier, and M. Wiescher**. "Measurement of the stellar cross sections for the reactions 9Be(n,γ) 10Be and 13C(n,γ) 14C via AMS". *Journal of Physics G: Nuclear and Particle Physics* 35.1 (Jan. 2008), p. 8.

[78] **K. Nishiizumi, M. Imamura, M. W. Caffee, J. R. Southon, R. C. Finkel, and J. McAninch**. "Absolute calibration of 10Be AMS standards". *Nuclear Instruments and Methods in Physics Research Section B: Beam Interactions with Materials and Atoms* 258.2 (May 2007), pp. 403–413.

[79] **FAST ComTec GmbH**. *MPA-3 Multiparameter Data Acquisition System User Manual.* Tech. rep. 2014.

[80] **R. Brun and F. Rademakers**. "ROOT — An object oriented data analysis framework". *Nuclear Instruments and Methods in Physics Research Section A: Accelerators, Spectrometers, Detectors and Associated Equipment* 389.1-2 (Apr. 1997), pp. 81–86.

[81] **C. Tuniz, J. Bird, D. Fink, and G. Herzog**. *Accelerator Mass Spectrometry: Ultrasensitive Analysis for Global Science.* New York: CRC Press, 1998.

[82] **L. Wacker, M. Christl, and H. A. Synal**. "Bats: A new tool for AMS data reduction". *Nuclear Instruments and Methods in Physics Research, Section B: Beam Interactions with Materials and Atoms* 268.7-8 (2010), pp. 976–979.

[83] **P. Ludwig**. "Search for 60Fe of Supernova Origin in Eath's Microfossil Record". *PhD Thesis, University of Munich* (Sept. 2015).

[84] **M. Limongi and A. Chieffi**. "The nucleosynthesis of Al26 and Fe60 in solar metallicity stars extending in mass from 11 to 120 Msun: the hydrostatic and explosive contributions" (Apr. 2006), pp. 483–500.

[85] **J. Feige**. "The Connection between the Local Bubble and the 60Fe Anomaly in the Deep Sea Hydrogenetic Ferromanganese Crust". *Magisterarbeit, University of Vienna* (Mar. 2010).

[86] **G. Rugel, T. Faestermann, K. Knie, G. Korschinek, M. Poutivtsev, D. Schumann, N. Kivel, I. Günther-Leopold, R. Weinreich, and M. Wohlmuther**. "New Measurement of the 60Fe Half-Life." *Physical review letters* 103 (Aug. 2009), p. 4.

[87] **K. Ostdiek, T. Anderson, W. Bauder, M. Bowers, P. Collon, R. Dressler, J. Greene, W. Kutschera, W. Lu, M. Paul, D. Robertson, D. Schumann, M. Skulski, and A. Wallner**. "Towards a measurement of the half-life of 60 Fe for stellar and early Solar System models". *Nuclear Instruments and Methods in Physics Research Section B: Beam Interactions with Materials and Atoms* 361 (Oct. 2015), pp. 638–642.

[88] **C. Fitoussi, G. M. Raisbeck, K. Knie, G. Korschinek, T. Faestermann, S. Goriely, D. Lunney, M. Poutivtsev, G. Rugel, C. Waelbroeck, and A. Wallner**. "Search for supernova-produced 60Fe in a marine sediment". *Physical Review Letters* 101 (Sept. 2008), p. 15.

[89] **R. Altenkirch**. "Setting the new AMS-Injector at the FN-Tandem Accelerator into Operation and First Performance Test". *Master Thesis, University of Cologne* (June 2014).

[90] **R. De Maesschalck, D. Jouan-Rimbaud, and D. L. Massart**. "The Mahalanobis distance". *Chemometrics and Intelligent Laboratory Systems* 50.1 (Jan. 2000), pp. 1–18.

[91] **F. P. Cranston and D. H. White**. "Thermal neutron capture cross sections in calcium". *Nuclear Physics, Section A* 169.1 (June 1971), pp. 95–100.

[92] **K. Nishiizumi, M. W. Caffee, and D. J. DePaolo**. "Preparation of 41Ca AMS standards". *Nuclear Instruments and Methods in Physics Research Section B: Beam Interactions with Materials and Atoms* 172.1-4 (Oct. 2000), pp. 399–403.

[93]   **G. Jörg, Y. Amelin, K. Kossert, and C. Lierse v. Gostomski**. "Precise and direct determination of the half-life of41Ca". *Geochimica et Cosmochimica Acta* 88 (July 2012), pp. 51–65.

[94]   **K. C. Welten, D. J. Hillegonds, J. Masarik, and K. Nishiizumi**. "Cosmogenic 41Ca in diogenites: Production rates, pre-atmospheric size and terrestrial ages". *Nuclear Instruments and Methods in Physics Research, Section B: Beam Interactions with Materials and Atoms* 259.1 (June 2007), pp. 653–662.

[95]   **A. Wallner, A. Arazi, T. Faestermann, K. Knie, G. Korschinek, H. Maier, N. Nakamura, W. Rühm, and G. Rugel**. "41Ca – a possible neutron specific biomarker in tooth enamel". *Nuclear Instruments and Methods in Physics Research Section B: Beam Interactions with Materials and Atoms* 223-224.SPEC. ISS. (Aug. 2004), pp. 759–764.

[96]   **S. P. Freeman, B. Beck, J. M. Bierman, M. W. Caffee, R. P. Heaney, L. Holloway, R. Marcus, J. R. Southon, and J. S. Vogel**. "The study of skeletal calcium metabolism with 41Ca and 45Ca". *Nuclear Instruments and Methods in Physics Research, Section B: Beam Interactions with Materials and Atoms* 172.1-4 (Oct. 2000), pp. 930–933.

[97]   **H. Shen, F. Pang, S. Jiang, M. He, K. Dong, L. Dou, Y. Pang, X. Yang, X. Ruan, M. Liu, and C. Xia**. "Study on 41 Ca-AMS for diagnosis and assessment of cancer bone metastasis in rats". *Nuclear Instruments and Methods in Physics Research Section B: Beam Interactions with Materials and Atoms* 361 (Oct. 2015), pp. 643–648.

[98]   **D. Fink, J. Klein, and R. Middleton**. "41Ca: past, present and future". *Nuclear Instruments and Methods in Physics Research Section B: Beam Interactions with Materials and Atoms* 52.3-4 (Dec. 1990), pp. 572–582.

[99]   **IAEA**. "Radiological Characterization of Shut Down Nuclear Reactors for Decommissioning Purposes". *INTERNATIONAL ATOMIC ENERGY AGENCY TECHNICAL REPORTS* 389 (1998).

[100]   **T. Schulze-König, C. Maden, E. Denk, S. Freeman, M. Stocker, M. Suter, H.-A. Synal, and T. Walczyk**. "Comparison of 41Ca analysis on 0.5MV and 5MV-AMS systems". *Nuclear Instruments and Methods in Physics Research Section B: Beam Interactions with Materials and Atoms* 268.7-8 (Apr. 2010), pp. 752–755.

[101]   **C. Vivo-Vilches, J. M. López-Gutiérrez, M. García-León, C. Vockenhuber, and T. Walczyk**. "41Ca measurements on the 1 MV AMS facility at the Centro Nacional de Aceleradores (CNA, Spain)". *Nuclear Instruments and Methods in Physics Research, Section B: Beam Interactions with Materials and Atoms* 413 (Dec. 2017), pp. 13–18.

[102]   **M. He, X. Ruan, S. Wu, W. Wang, C. Li, H. Shen, X. Wang, L. Lu, S. Wu, G. He, and S. Jiang**. "41Ca analysis using CaF- in CIAE–AMS system". *Nuclear Instruments and Methods in Physics Research Section B: Beam Interactions with Materials and Atoms* 268.7-8 (Apr. 2010), pp. 804–806.

[103] **S. Hosoya, K. Sasa, T. Matsunaka, T. Takahashi, M. Matsumura, H. Matsumura, M. Sundquist, M. Stodola, and K. Sueki**. "Optimization of a ΔE-E detector for 41Ca AMS". *Nuclear Instruments and Methods in Physics Research Section B: Beam Interactions with Materials and Atoms* 406 (Sept. 2017), pp. 268–271.

[104] **Y. Oura**. "UTTAC ANNUAL REPORT 2016". *UTTAC ANNUAL REPORT* 86 (Sept. 2017), p. 112.

[105] **C. Vockenhuber, T. Schulze-König, H.-A. Synal, I. Aeberli, and M. Zimmermann**. "Efficient 41Ca measurements for biomedical applications". *Nuclear Instruments and Methods in Physics Research Section B: Beam Interactions with Materials and Atoms* 361 (Oct. 2015), pp. 273–276.

[106] **A. Wallner, M. Bichler, I. Dillmann, R. Golser, F. Käppeler, W. Kutschera, M. Paul, A. Priller, P. Steier, and C. Vockenhuber**. "AMS measurements of 41Ca and 55Fe at VERA – two radionuclides of astrophysical interest". *Nuclear Instruments and Methods in Physics Research Section B: Beam Interactions with Materials and Atoms* 259.1 (June 2007), pp. 677–682.

[107] **A. Wallner, O. Forstner, R. Golser, G. Korschinek, W. Kutschera, A. Priller, P. Steier, and C. Vockenhuber**. "Fluorides or hydrides? 41Ca performance at VERA's 3-MV AMS facility". *Nuclear Instruments and Methods in Physics Research, Section B: Beam Interactions with Materials and Atoms* 268.7-8 (Apr. 2010), pp. 799–803.

[108] **G. Rugel, S. Pavetich, S. Akhmadaliev, S. M. Enamorado Baez, A. Scharf, R. Ziegenrücker, and S. Merchel**. "The first four years of the AMS-facility DREAMS: Status and developments for more accurate radionuclide data". *Nuclear Instruments and Methods in Physics Research Section B: Beam Interactions with Materials and Atoms* 370 (Mar. 2016), pp. 94–100.

[109] **High Voltage Engineering Europa B.V.** "Technical Drawing of the 4 Anode Ionization Chamber from High Voltage Engineering Europa B.V." (2006).

[110] **X. Hou**. "Liquid scintillation counting for determination of radionuclides in environmental and nuclear application". *Journal of Radioanalytical and Nuclear Chemistry* 318.3 (Dec. 2018), pp. 1597–1628.

[111] **D. Hampe, B. Gleisberg, S. Akhmadaliev, G. Rugel, and S. Merchel**. "Determination of 41Ca with LSC and AMS: method development, modifications and applications". *Journal of Radioanalytical and Nuclear Chemistry* 296.2 (May 2013), pp. 617–624.

[112] **DIN 25413-2:2018-04**. "Klassifikation von Abschirmbetonen nach Elementanteilen – Teil 2: Abschirmung von Gammastrahlung". *DEUTSCHE NORM* (Apr. 2013).

[113] **DIN 1045-2:2008-08**. "Tragwerke aus Beton, Stahlbeton und Spannbeton – Teil 2: Beton – Festlegung, Eigenschaften, Herstellung und Konformität – Anwendungsregeln zu DIN EN 206-1". *DEUTSCHE NORM* (Aug. 2008).

[114] **DIN EN-206-1:2001-07**. "Beton Teil 1: Festlegung, Eigenschaften, Herstellung und Konformität Deutsche Fassung EN 206-1:2000". *DEUTSCHE NORM* (July 2001).

[115]   **DIN 25413-1:2018-04**. "Klassifikation von Abschirmbetonen nach Elementanteilen –
        Teil 1: Abschirmung von Neutronenstrahlung". *DEUTSCHE NORM* (Apr. 2013).

[116]   **M. Ziegner, T. Schmitz, R. Khan, M. Blaickner, H. Palmans, P. Sharpe, G. Hampel, and H. Böck**. "Confirmation of a realistic reactor model for BNCT dosimetry at the
        TRIGA Mainz". *Medical Physics* 41.11 (Nov. 2014), p. 8.

[117]   **E. Nottoli, P. Bienvenu, D. Bourlès, A. Labet, M. Arnold, and M. Bertaux**. "Determination of Long-Lived Radionuclide (10 Be, 41 Ca, 129 I) Concentrations in Nuclear
        Waste by Accelerator Mass Spectrometry". *Volume 1: Low/Intermediate-Level Radioactive
        Waste Management; Spent Fuel, Fissile Material, Transuranic and High-Level Radioactive
        Waste Management*. Vol. 1. ASME, Sept. 2013, p. 4.

[118]   **L. A. Currie**. "Limits for qualitative detection and quantitative determination. Application
        to radiochemistry". *Analytical Chemistry* 40.3 (Mar. 1968), pp. 586–593.

[119]   **H. Sahadath, A. S. Mollah, K. A. Kabir, and M. Fazlul Huq**. "Calculation of the
        different shielding properties of locally developed ilmenite-magnetite (I-M) concrete".
        Radioprotection 50.3 (July 2015), pp. 203–207.

[120]   **J. Southon and G. M. Santos**. "Life with MC-SNICS. Part II: Further ion source
        development at the Keck carbon cycle AMS facility". *Nuclear Instruments and Methods
        in Physics Research, Section B: Beam Interactions with Materials and Atoms* 259.1 (June
        2007), pp. 88–93.

List of Figures

List of Tables

Danksagung

Erklärung zur Urheberschaft

„Ich versichere, dass ich die von mir vorgelegte Dissertation selbständig angefertigt, die benutzten Quellen und Hilfsmittel vollständig angegeben und die Stellen der Arbeit - einschließlich Tabellen, Karten und Abbildungen -, die anderen Werken im Wortlaut oder dem Sinn nach entnommen sind, in jedem Einzelfall als Entlehnung kenntlich gemacht habe; dass diese Dissertation noch keiner anderen Fakultät oder Universität zur Prüfung vorgelegen hat; dass sie - abgesehen von unten angegebenen Teilpublikationen - noch nicht veröffentlicht worden ist sowie, dass ich eine solche Veröffentlichung vor Abschluss des Promotionsverfahrens nicht vornehmen werde. Die Bestimmungen der Promotionsordnung sind mir bekannt. Die von mir vorgelegte Dissertation ist von apl. Prof. Dr. Alfred Dewald betreut worden.“

Köln, 02.07.2019   Richard Spanier

Teilpublikationen

R. Altenkirch, C. Feuerstein, M. Schiffer, G. Hackenberg, S. Heinze, C. Müller-Gatermann, A. Dewald „*Operating the 120° Dipol-Magnet at the CologneAMS in a gas-filled mode*“, Nucl. Instr. and Meth. B 438 (2019) 184-188